

**Development of a QA testing and
benchmarking framework and a search for
the $B_c^+ \rightarrow \bar{K}^{*0}(892) (\rightarrow K^- \pi^+) K^+$ decay at
LHCb**



A THESIS SUBMITTED IN FULFILMENT OF THE REQUIREMENTS FOR THE DEGREE OF DOCTOR OF
PHILOSOPHY AT THE UNIVERSITY OF BIRMINGHAM

BY

NATHANAEL ASHTON SPENCER FARLEY

University of Birmingham, UK

2018

UNIVERSITY OF
BIRMINGHAM

University of Birmingham Research Archive

e-theses repository

This unpublished thesis/dissertation is copyright of the author and/or third parties. The intellectual property rights of the author or third parties in respect of this work are as defined by The Copyright Designs and Patents Act 1988 or as modified by any successor legislation.

Any use made of information contained in this thesis/dissertation must be in accordance with that legislation and must be properly acknowledged. Further distribution or reproduction in any format is prohibited without the permission of the copyright holder.

Abstract

This thesis describes the implementation of LHCbPR, a QA testing and benchmarking framework for the LHCb experiment at CERN, and a search for the rare decay $B_c^+ \rightarrow \bar{K}^{*0}(892)(\rightarrow K^- \pi^+)K^+$.

LHCbPR is a novel framework that meets the needs of simulation and other software work of the LHCb collaboration. It is built to test software using modern techniques while adapting for the particular challenges of tests with durations varying between a second and many hours. LHCbPR uses a microservice architecture, loosely coupling the different components essential to run, aggregate and display tests and their results.

Hints of the rare decay $B_c^+ \rightarrow \bar{K}^{*0}(892)(\rightarrow K^- \pi^+)K^+$ have been reported previously by the LHCb Collaboration. The analysis in this thesis seeks to improve on previous measurements by performing a dedicated search for this particular decay channel using 3 fb^{-1} of proton proton collision data recorded at centre-of-mass energies of 7 TeV and 8 TeV at the LHC.

Contents

Abstract	<i>iii</i>
Contents	<i>v</i>
List of Figures	<i>x</i>
List of Tables	<i>xiii</i>
Author's contribution	<i>xv</i>
1 Introduction	1
1.1 Standard Model	4
1.1.1 Strong force	5
1.1.2 Electroweak	6
1.1.2.1 Quark flavour	7
1.2 B_c meson	8
2 The LHCb experiment	11
2.1 VELO	13

2.2	RICH	15
2.2.1	RICH 1	16
2.2.2	RICH 2	18
2.2.3	PMT	19
2.3	Bending magnet	19
2.4	Tracking systems	20
2.5	Calorimetry	20
2.5.1	ECAL	21
2.5.2	HCAL	23
2.6	Muon systems	24
2.7	Trigger and stripping	26
2.7.1	L0	26
2.7.2	HLT	27
2.7.3	Stripping	27
2.8	ProbNN	28
2.9	Simulation	28
2.9.1	PYTHIA	30
2.9.2	BcVegPy	31
2.9.3	EvtGen	31
2.9.4	Geant4	31
2.9.5	Boole	32
2.9.6	Moore	33
2.9.7	Brunel	33

2.9.8	DaVinci	33
3	PMT ageing validation	35
3.1	Prior work	35
3.2	Motivation	36
3.2.1	Ageing	37
3.3	Experimental setup	39
3.3.1	R12699 PMT	41
3.4	Method	43
3.5	Analysis	44
3.6	Results	45
4	LHCbPR	47
4.1	Prior work	48
4.2	Microservices	49
4.3	Individual microservices	49
4.3.1	LbNightlyTools	49
4.3.1.1	Configuration	50
4.3.1.2	Checkout	50
4.3.1.3	Building and testing	50
4.3.1.4	Jenkins configuration	52
4.3.1.5	Dashboard	52
4.3.2	LHCbPR2HD	53
4.3.3	LHCbPR2BE	55

4.3.4	LHCbPR2ROOT	55
4.3.5	LHCbPR2FE	56
4.3.5.1	Motivation for rewriting front end	61
4.3.6	LHCbPR2FE2	63
5	Analysis	65
5.1	Simulation	67
5.1.1	Recalculating ProbNN variables	67
5.1.1.1	PIDCorr	68
5.2	Selection	69
5.2.1	Preselection	69
5.2.1.1	Trigger cuts	71
5.2.1.2	Stripping	72
5.2.1.3	Resonant mass cuts	74
5.2.2	BDT	75
5.2.2.1	Results	80
5.2.2.2	Punzi figure of merit	83
5.3	Yield extraction	83
5.3.1	Fit description	86
5.3.2	Expected results	91
5.3.3	Fit results	94
5.4	Efficiencies	94
5.4.1	Selection efficiency	96

<i>CONTENTS</i>	<i>ix</i>
5.5 Systematic errors	97
5.5.1 Fit model choices	98
5.5.2 Toy studies	104
6 Conclusion	107
References	109

List of Figures

1.1	Observed beta decay energy spectrum	3
2.1	b acceptance for LHCb at 7 TeV to 8 TeV [31]	12
2.2	A schematic view of the LHCb detector [30].	12
2.3	VELO resolution performance [32].	14
2.4	Schematic of the VELO.	14
2.5	Schematic of the VERtEx LOcator (VELO) position.	15
2.6	Schematic image of Cherenkov radiation [33].	17
2.7	RICH ability to identify μ , π , K and p	17
2.8	Schematic design of the RICHs.	18
2.9	Dynode chain example from [36]	19
2.10	Schematic diagram of the ECAL [39]	21
2.11	Schematic of HCAL.	23
2.12	Schematic design of the muon stations [30].	25
2.13	LHCb data flow [47]	29
3.1	Gain variation vs. illumination period as found in [57] for the PMT.	36

3.2	Secondary emissive layer damage (down-drift model).	38
3.3	Secondary emissive layer damage (up-drift model).	39
3.4	Long-term Photomultiplier Tube (PMT) ageing experiment.	42
3.5	Pixel positions on the PMT.	43
3.6	An example of pulse height measurement	44
3.7	Gain vs. lab time for PMT ageing.	45
3.8	Gain vs. LHCb time for PMT ageing.	46
4.1	LHCb Continuous build and integration system [66].	51
4.2	the Nightly Build System (LbNightlyTools) screenshot	54
4.3	Example of LHCbPR test view (from HLT team).	58
4.4	A screenshot of LHCbPR2FE's ROOT file browser's widget.	60
5.1	Feynman diagrams for control and signal channels.	66
5.2	Results of the calculation of the KDE for ProbNNp [78].	70
5.3	Schematic diagram of the TISTOS method [79].	71
5.4	Schematic view of decay as seen in lab frame.	73
5.5	Input variable distributions for the BDT for control channel 2011	76
5.6	Input variable distributions for the BDT for control channel 2012	77
5.7	Input variable distributions for the BDT for signal channel 2011	78
5.8	Input variable distributions for the BDT for signal channel 2012	79
5.9	Overtraining plots for $B^+ \rightarrow K^{*0}(892)(\rightarrow K^+ \pi^-) \pi^+$	81
5.10	Overtraining plots for $B_c^+ \rightarrow \bar{K}^{*0}(892)(\rightarrow K^- \pi^+) K^+$	82
5.11	Punzi figure of merit for various Boosted Decision Tree (BDT) cuts for control channel.	84

5.12	Punzi figure of merit for various BDT cuts for signal channel.	85
5.13	Fit to simulated data for the control channel using Ipatia distribution.	88
5.14	Fit to simulated data for the signal channel using Ipatia distribution.	89
5.15	Fit of 2011 control channel data.	91
5.16	Fit of 2012 control channel data.	92
5.17	Background sidebands for $B_c^+ \rightarrow \bar{K}^{*0}(892)(\rightarrow K^- \pi^+)K^+$	93
5.18	Unblinded data fits for $B_c^+ \rightarrow \bar{K}^{*0}(892)(\rightarrow K^- \pi^+)K^+$	95
5.19	Double Crystal Ball (DCB) fit to control channel simulated data 2011	100
5.20	DCB fit to control channel data 2011	101
5.21	Background fit of 2011 signal channel for $B_c^+ \rightarrow \bar{K}^{*0}(892)(\rightarrow K^- \pi^+)K^+$ data	102
5.22	Background fit of 2012 signal channel for $B_c^+ \rightarrow \bar{K}^{*0}(892)(\rightarrow K^- \pi^+)K^+$ data	103
5.23	Toy studies for the $B^+ \rightarrow K^{*0}(892)(\rightarrow K^+ \pi^-)\pi^+$ case	105

List of Tables

1.1	Properties of quarks [12].	2
1.2	Features of the fundamental forces included in the SM.	4
1.3	Properties of leptons.	5
5.1	Trigger cuts. All events must pass at least one trigger on each level to be included. . . .	72
5.2	List of variables used in BDT.	75
5.3	Values of parameters held constant in final Ipatia function.	90
5.4	Efficiencies for simulated data for the control channel.	97
5.5	Efficiencies for simulated data for the signal channel.	97
5.6	Comparisons of variables between Ipatia and DCB fit.	99

Author's Contribution

The work in this thesis is a combination of the author's own contributions and the contributions of others. The work in Chapter 3 and Chapter 5 (excluding Sections 5.2.1.1 and 5.2.1.2) are entirely the author's work except where referenced. Significant contributions were made by the author to LHCbPR2FE, as detailed in Section 4.3.5, with the invention of the Turboview being entirely the author's contribution.

Chapter 1

Introduction

In Ancient Greece, Democritus is credited with proposing the theory of atoms, which are defined as indivisible units of matter; the universe being composed only of atoms and void. After the idea had been overlooked for millennia, modern experiments have found that the truth is much closer to the model proposed by Democritus, but what is now called the atom is not fundamental. After the discovery of the constituents of the atom, a small number of particles were discovered up to the early 1950s, at which point, advances in particle accelerator technology allowed significant increases in centre-of-mass energy of particle collisions. Beginning with the Bevatron accelerator [1], the 1950s–1960s saw a figurative explosion of new particles being discovered. The known universe was no longer restricted to protons, neutrons, electrons, K , π mesons and the Λ hyperon, some of their anti-particles and photons.

With the discovery of numerous states (e.g. ρ [2], Λ [3], η [4] and more) with significantly differing masses, a unifying theory was proposed [5], analogous with the periodic table and based on a set of fundamental particles called *quarks* [6]. These are massive, point-like spin-half particles

Table 1.1: Properties of quarks [12].

Quark	Symbol	Charge	Mass
down	d	$-1/3$	$4.7^{+0.5}_{-0.3} \text{ MeV}/c^2$
up	u	$+2/3$	$2.2^{+0.5}_{-0.4} \text{ MeV}/c^2$
strange	s	$-1/3$	$95^{+9}_{-3} \text{ MeV}/c^2$
charm	c	$+2/3$	$1.28^{+0.025}_{-0.035} \text{ GeV}/c^2$
bottom	b	$-1/3$	$4.18^{+0.04}_{-0.03} \text{ GeV}/c^2$
top	t	$+2/3$	$(173.0 \pm 0.4) \text{ GeV}/c^2$

that carry colour charge, electromagnetic (EM) charge, flavour, weak isospin/hypercharge and baryon number. At first, just the up, down and strange quarks (often called ‘light’ quarks) were discovered [7], followed by the discovery of charm [8, 9], bottom [10] and finally top [11] in 1995 (often called ‘heavy’ quarks).

The quark model defines several properties of quarks, summarised in Table 1.1, which are:

flavours Quarks have *flavour* characterising their weak interactions

mass Each of the quarks has a distinct finite mass varying between a few MeV up to $\sim 10^2$ GeV

charges Quarks have fractions of electron charge which contribute to the overall EM charge of the particle that they form, e.g. protons and neutrons

Quarks are bound by the strong force which acts on objects with colour charge.

In addition to quarks, there are other fundamental fermions (spin- $\frac{1}{2}$ particles) that do not have colour charge (called leptons): electrons, muons, tau leptons and their neutrino counterparts.

Neutrinos were discovered in trying to explain the energy spectra of beta decays (Figure 1.1). When beta decay was discovered, it was expected that the energy spectra would be a sharp peak around the mass difference between the initial and final state constituents in order to conserve en-

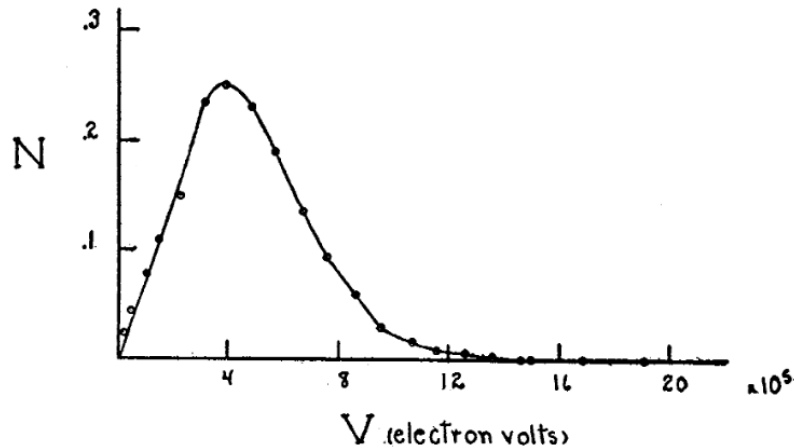


Figure 1.1: Observed beta decay spectrum in 1935. It was expected that there would be a narrow energy spectrum. This puzzle prompted the discovery of the neutrino. Reprinted figure with permission from F. A. Scott. “Energy Spectrum of the Beta-Rays of Radium E”. in: *Phys. Rev.* 48.5 (Sept. 1935), pp. 391–395. DOI: 10.1103/PhysRev.48.391

ergy. When the spectrum was found shown on Figure 1.1, many theories were proposed (including the non-conservation of energy!). Pauli [14] postulated the existence of small neutral particles which we now call neutrinos and their existence was confirmed in 1956 [15].

These quarks and leptons can be grouped into three *generations*. Formally, quarks are formed into SU(2) doublets within each generation and charged leptons are paired into doublets with their equivalent neutrino.

Properties of particles define the *interactions* between them. There are four fundamental forces responsible for the interactions between particles each with associated gauge bosons. Only three are sufficiently strong to be considered at the scale of particle physics i.e. $\sim 10^{-15}$ m:

- EM force (mediated by photons, γ)

Table 1.2: Features of the fundamental forces included in the SM[12]. *Strength relative to the EM force, for two u quarks separated 10^{-18}

m[16].				
Interaction	Mediator	Coupling strength*	Range (m)	Med. mass GeV/c^2
Strong	g	25	∞	0
EM	γ	1	∞	0
Weak	Z^0, W^\pm	0.8	10^{-18}	$W^\pm (80.379 \pm 0.012) \text{ GeV}/c^2$ $Z^0 (91.1876 \pm 0.0021) \text{ GeV}/c^2$

- Weak force (mediated by W^\pm and Z bosons)
- Strong force (mediated by gluons, g)

Properties of the gauge bosons are shown in Table 1.2.

1.1 Standard Model

The Standard Model (SM) is a Quantum Field Theory (QFT), one can write

$$SU(3)_C \times SU(2)_W \times U(1)_Y, \quad (1.1)$$

where $U(1)_Y$ is the unitary group responsible for weak hypercharge (a combination of the EM charge and isospin of fermions), $SU(2)_W$ is the special unitary group responsible for the electroweak interactions (a combination of the EM and weak forces) and $SU(3)_C$ the special unitary group responsible for colour interactions that describe the strong force.

The SM assumes that all particles have anti-particle equivalents with all quantum numbers reversed or identical (in the case that a particle is its own anti-particle). This is represented by the adjoint representation of a given particle.

Table 1.3: Properties of leptons [12]. Neutrino masses have upper limits set and the mass difference between them has been measured (although the mass hierarchy is not known)

Lepton	Symbol	Charge	Mass
electron	e	-1	$(0.510\,998\,946\,1 \pm 0.000\,000\,003\,1) \text{ MeV}/c^2$
electron neutrino	ν_e	0	$< 2 \text{ eV}/c^2$
muon	μ	-1	$(105.658\,374\,5 \pm 0.000\,002\,4) \text{ MeV}/c^2$
muon neutrino	ν_μ	0	$< 0.19 \text{ MeV}/c^2$
tau	τ	-1	$(1776.86 \pm 0.12) \text{ MeV}/c^2$
tau neutrino	ν_τ	0	$< 18.2 \text{ MeV}/c^2$

The SM defines fundamental particles which can be put into two categories: fermions with half integer spin and bosons with integer spin. Fermions are classified further into quarks (Table 1.1) and leptons (Table 1.3) as mentioned previously.

1.1.1 Strong force

The strong force, described by Quantum ChromoDynamics (QCD), contains three colour charges and three anti-colour charges: red/anti-red (R), blue/anti-blue (B) and green/anti-green (G). It is mediated by gluons, of which there are eight, each with a single colour and anti-colour charge e.g. $R\bar{G}$.

Only quarks and gluons are subject to the strong force. It is postulated that observable particles are always colourless and therefore hadrons can only exist in combinations of quarks and anti-quarks that ensure this, e.g. quark anti-quark pairs or triplets of quarks. In addition to these 2- or 3-quark states, there is growing evidence for the existence of bound states consisting of 5-quark states, so-called pentaquarks, as recently reported by the Large Hadron Collider beauty (LHCb)

experiment[17]. Note that the pentaquarks reported by LHCb are distinct from those originally reported at HERA in [18] which were not confirmed by subsequent data or any other experiments.

In practice, calculations involving the strong force are challenging because of the complexity of diagrams (gluon self-interactions) and the magnitude of the characteristic coupling parameter α_s . The potential describing the force can be described by a short range component acting as $1/r$ and a long range component that is proportional to r . In the large separation limit i.e. low energy limit, the potential between quarks becomes arbitrarily large while the strong coupling α_s becomes large making perturbative methods inappropriate. Various phenomenological models describe this regime, including string fragmentation [19] in which quark anti-quark pairs are produced from the vacuum as it becomes more energetically favourable to create new particles from the vacuum instead of ‘maintaining’ the high potential between the original quark anti-quark pair.

1.1.2 Electroweak

At low energies (under ~ 100 GeV), the EM and weak force are distinct but at higher energies they combine to form the $SU(2)_W \times U(1)_Y$ group found in Equation 1.1. Therefore, the SM puts both of these interactions in the same group.

Quantum ElectroDynamics (QED) [20] calculations can be solved to a high precision since the boson responsible for it (the photon, γ) does not carry EM charge and therefore has no self-interactions. The strength of the EM coupling parameter, α_{EM} , is $\ll 1$ meaning perturbative calculations converge rapidly. Two notable examples of the very high experimental precision that can be achieved, that necessitate such calculations, are (see references for definition):

- the electron magnetic moment, $g/2$, is measured to be $1.001\,159\,652\,180\,85 \pm 0.000\,000\,000\,000\,76$ [21]

- α_{EM}^{-1} is measured to be $137.035\,999\,070 \pm 0.000\,000\,098$ [22]

The weak force is mediated by the W and Z bosons. Since both of these bosons have very high mass their range is limited by the Heisenburg uncertainty principle to an effective range of $\sim 10^{-18}$ m. The weak force interacts with all known fermions. It is also the only force in the SM to change the flavour of particles via the W boson.

1.1.2.1 Quark flavour

Quark flavour was assigned based on non-observations of kinematically allowed decays. Quarks have flavour up, down, strange, charmed, top and bottom, each assigned an integer quantum number (e.g. strangeness, charmedness, etc.) whose sign matches its EM charge and must be conserved in strong, EM and neutral current weak interactions.¹ These can be seen in Table 1.1.

Each quark is represented by weak eigenstates which map onto mass eigenstates via the \mathbf{V}_{CKM} rotation matrix[12]:

$$\begin{pmatrix} d_W \\ s_W \\ b_W \end{pmatrix} = \mathbf{V}_{\text{CKM}} \begin{pmatrix} d \\ s \\ b \end{pmatrix} \quad (1.2)$$

$$\mathbf{V}_{\text{CKM}} = \begin{pmatrix} c_{12}c_{13} & s_{12}c_{13} & s_{13}e^{-i\delta_{13}} \\ -s_{12}c_{23} - c_{12}s_{23}s_{13}e^{i\delta_{13}} & c_{12}c_{23} - s_{12}s_{23}s_{13}e^{i\delta_{13}} & s_{23}c_{13} \\ s_{12}s_{23} - c_{12}c_{23}s_{13}e^{i\delta_{13}} & -c_{12}s_{23} - s_{12}c_{23}s_{13}e^{i\delta_{13}} & c_{23}c_{13} \end{pmatrix}, \quad (1.3)$$

¹For historical reasons the up and down quarks do not have ‘up-ness’ and ‘down-ness’ and instead use strange isospin of 1/2 and -1/2 respectively.

where $c_{ij} = \cos(\theta_{ij})$ and $s_{ij} = \sin(\theta_{ij})$, which corresponds to

$$\mathbf{V}_{\text{CKM}} = \begin{pmatrix} V_{ud} & V_{us} & V_{ub} \\ V_{cd} & V_{cs} & V_{cb} \\ V_{td} & V_{ts} & V_{tb} \end{pmatrix}, \quad (1.4)$$

where V_{ij}^2 corresponds to the probability a quark can undergo the transition $i \rightarrow j$. The currently measured values for \mathbf{V}_{CKM} are [23]

$$\left(|V_{ij}| \right) = \begin{pmatrix} 0.97417 \pm 0.00021 & 0.2248 \pm 0.0006 & (4.09 \pm 0.39) \times 10^{-3} \\ 0.220 \pm 0.005 & 0.995 \pm 0.016 & (40.5 \pm 1.5) \times 10^{-3} \\ (8.2 \pm 0.6) \times 10^{-3} & (40.0 \pm 2.7) \times 10^{-3} & 1.009 \pm 0.031 \end{pmatrix}. \quad (1.5)$$

\mathbf{V}_{CKM} is unitary, assuming three generations of quarks, which implies:

$$\sum_{i=u,c,t} |V_{ij}|^2 = 1; \quad \sum_{k=d,s,b} V_{ij} V_{kj}^* = 0. \quad (1.6)$$

The \mathbf{V}_{CKM} can also be expressed in terms of Wolfenstein parameters[12]:

$$\begin{pmatrix} 1 - \lambda^2/2 & \lambda & A\lambda^3(\rho - i\eta) \\ -\lambda & 1 - \lambda^2/2 & A\lambda^2 \\ A\lambda^3(1 - \rho - i\eta) & -A\lambda^2 & 1 \end{pmatrix}. \quad (1.7)$$

where $\lambda = s_{12}$, $A\lambda^2 = s_{23}$ and $A\lambda^3(\rho - i\eta) = s_{13}e^{-i\delta}$.

1.2 B_c meson

The B_c meson, composed of b and c valence quarks, is the heaviest meson possible in the SM with two unlike flavour quarks. Due of its high mass, its occurrence is suppressed relative to lighter b

mesons. The c quark accounts for $\sim 70\%$ of the B_c width [24], the b contributes $\sim 20\%$ [25], and 10% is contributed by $B_c \rightarrow W \rightarrow q\bar{q}$.

B_c annihilation decays at tree level with no b or c in the intermediate or final stages can only proceed via the W boson: $\bar{b}c \rightarrow W^+ \rightarrow u\bar{q}$ (where $q = d, s$). The amplitude of this decay process is dominated by the Cabibbo-Kobayashi-Maskawa (CKM) matrix elements $V_{cb}^* V_{uq}$ with any enhancement to the predicted branching fractions potentially indicating beyond SM physics such as a charged Higgs replacing the W .

The $B_c^+ \rightarrow \bar{K}^{*0}(892)K^+$ branching fraction has been predicted to be $(1.00^{+0.18}_{-0.34}) \times 10^{-6}$ [26]. Using $\mathcal{B}(B_c^+ \rightarrow J/\psi \pi^+) \sim [0.34, 2.9] \times 10^{-3}$ from [27] and $\frac{\sigma(B_c^+)}{\sigma(B^+)} \mathcal{B}(B_c^+ \rightarrow J/\psi \pi^+) = (7.0 \pm 0.3) \times 10^{-6}$ (from [28]), an estimate of $\frac{\sigma(B_c^+)}{\sigma(B^+)} \sim [0.23, 2.1]\%$ is found. Combined with [26], this gives a value of $\frac{\sigma(B_c^+)}{\sigma(B^+)} \mathcal{B}(B_c^+ \rightarrow \bar{K}^{*0}(892)(\rightarrow K^- \pi^+)K^+) \sim [0.1, 1.7] \times 10^{-8}$. This theoretical estimate is not inconsistent with the measured value of $(8.0^{+4.4}_{-3.8}(\text{stat}) \pm 0.6(\text{syst})) \times 10^{-8}$ [29], however the statistical uncertainty is sufficiently large that no firm conclusions can be drawn.

The aim of the analysis described in chapter 5 is to develop a more performant selection by focusing on one specific decay namely, $B_c^+ \rightarrow \bar{K}^{*0}(892)(\rightarrow K^- \pi^+)K^+$ with a view to making a first observation in LHCb Run 1 data of this annihilation process.

Chapter 2

The LHCb experiment

The LHCb detector[30] is dedicated to studying heavy flavour decays. For this reason, the LHCb detector was designed with a very forward angular coverage due to the high, forward peaking $b\bar{b}$ production cross section at the Large Hadron Collider (LHC). LHCb's acceptance accounts for $\sim 25\%$ of all b or \bar{b} decays (see Figure 2.1).

The LHCb detector, seen in Figure 2.2, has full detector coverage over 10 mrad to 300 mrad polar angle, or $2 < \eta < 5$ where η is defined as

$$\eta = -\ln(\tan(\theta/2)), \quad (2.1)$$

where θ is defined as the angle between particle momenta and the beam axis. The detector extends approximately 20 m from the interaction point and ~ 50 cm behind the interaction point. The z -axis is defined along the beam axis, with 0 defined at the nominal LHC interaction point, IP8, inside the VELO and positive leading into the main detector. The transverse plane is defined as the x - y plane perpendicular to the z -axis.

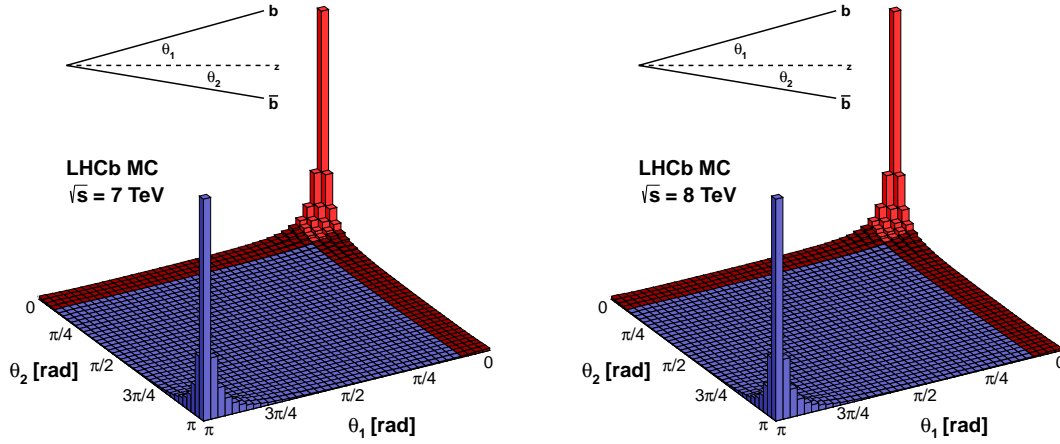


Figure 2.1: b acceptance for LHCb at 7 TeV to 8 TeV [31]

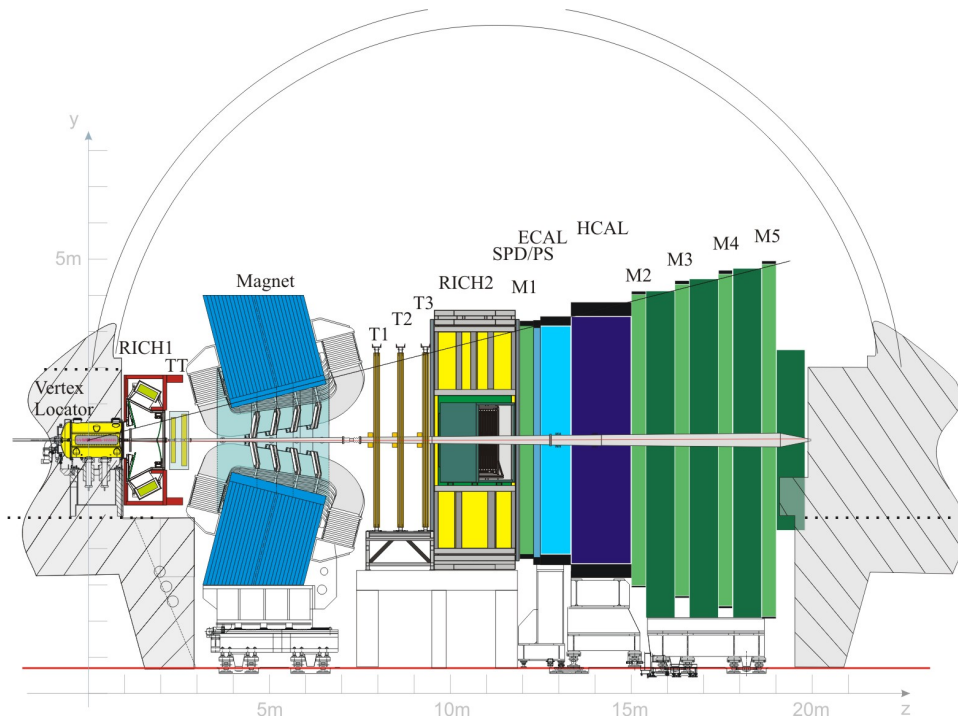


Figure 2.2: A schematic view of the LHCb detector [30].

2.1 VELO

Since b mesons decaying weakly have a relatively long lifetime, it is important to have good vertex resolution to measure the displacement of the hadron from the primary vertex (PV). The VELO plays a vital role in the experiment's ability to identify b -hadrons, known as b -tagging, by providing accurate measurements of the PV position.

The VELO is ~ 1 m in length and is positioned 17.5 cm upstream of the interaction point to ~ 75 cm downstream as seen in Figure 2.5. It is composed of 25 silicon detector stations. The design has been built to include the detection of backward tracks which travel upstream from the interaction point in order to determine the location of the PV. The key performance indicator for the VELO is the Impact Parameter (IP) resolution where the IP of a track is defined as its distance from the PV at the point of closest approach to the PV. This is illustrated in Figure 2.3 using 2012 data.

The VELO is a collection of silicon modules providing information on a track's r and ϕ coordinates, as measured along the beam axis. It contains 42 r sensors, plus four for backward tracks, and 42 ϕ sensors with 2048 readout channels per sensor with an average occupancy of $\sim 1.1\%$ (for Run 1).

The VELO is made up of two boxes which hold the semi-circular halves of the detector, as seen in Figure 2.4 and Figure 2.5, to allow the VELO to retract while the LHC is in its injection phase. During the injection phase, the VELO is withdrawn from the beam to a safe distance (>6 cm) and is then moved in closer when stable beam conditions have been established. When in position for data taking, the inner edges of VELO overlap by 1.5 cm with a minimum distance to the beam of 8 mm which is a compromise between proximity to nominal bunch crossing position for maximum

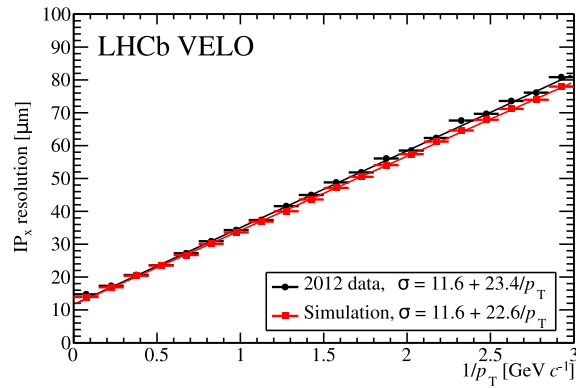


Figure 2.3: VELO resolution performance [32].

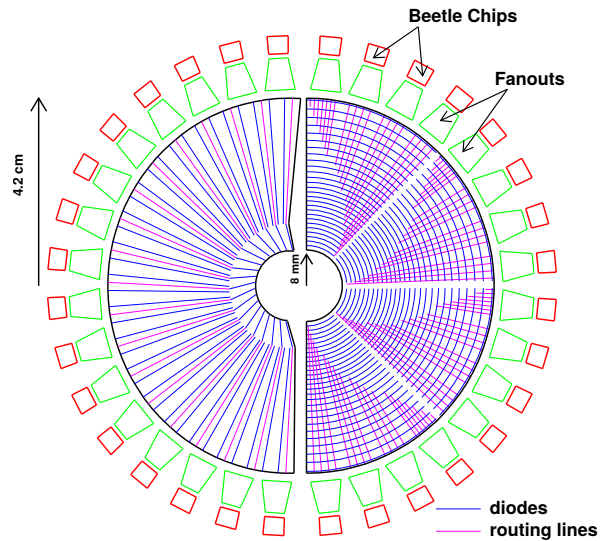


Figure 2.4: Schematic of the VELO design, left: ϕ -measuring sensor, right: R-measuring sensor. Figure and caption taken from [32]

benefit to track parameter determination and reducing risk of damage to the silicon detectors due to off momentum beam particles.

RF interference between the VELO and the beams can affect the accuracy and precision of the experiment. There are two main concerns: the beams can fall out of alignment, which can

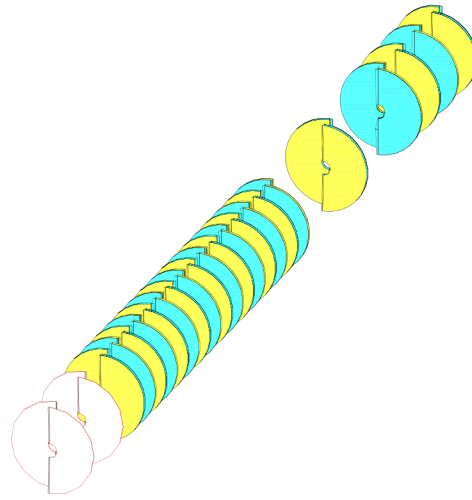


Figure 2.5: Schematic of the VELO position (white stations are upstream). Figure taken from [32].

potentially damage the VELO, disrupting the readout, and out-gassing. Wake field suppressors[32] and RF foil are placed between the VELO and the beam in order to combat these issues.

2.2 RICH

In the LHCb detector there are two Ring Imaging CHerenkov detectors (RICHs) detectors (see Figure 2.8), RICH 1 being situated directly downstream of the VELO and RICH 2 being placed downstream of the magnet and tracking stations T1, T2 and T3 as seen in Figure 2.2. They are designed to assist in Particle IDentification (PID) in the momentum range 1 GeV/c to 60 GeV/c for RICH 1 and 15 GeV/c to 100 GeV/c. The separation of different particle types in the data collected by the RICH can be seen clearly in Figure 2.7.

Particles which travel at speeds approaching the speed of light in vacuum inside the RICH emit Cherenkov radiation. During Run 1 this was done with Hybrid Photon Detectors (HPDs). For

the LHCb upgrade, to be installed between 2019 and 2021, the HPDs will be replaced with PMTs (see subsection 2.2.3 for more information). This is achieved by filling the RICHs with substances such that the phase speed of light is lower than the speed of particles in a given kinematic region. When charged particles travel through the RICH with a greater speed than that of the phase speed of light in the medium, rings of light are emitted as shock waves (as seen in Figure 2.6). This light is then collected through a system of mirrors and HPDs along the edges of the detector. The angle made by the emitted light and the particle is described by the relation

$$\cos \theta = \frac{1}{n\beta}, \quad (2.2)$$

where $\beta = \frac{v}{c}$ of the incident particle.

The RICH's innovative design is essential for PID in LHCb. As can be seen in Figure 2.7, it is straightforward to identify specific particles when presented with an isolated Cherenkov ring. During running it is rare to see such an isolated track, so a log likelihood search of all tracks is performed to identify the most likely candidate for a given Cherenkov ring (and therefore track) [34]. PID for a candidate is defined as the log likelihood that the Cherenkov ring belongs to a particular particle (e.g. PID_k for a candidate is the log likelihood that track belongs to a K).

2.2.1 RICH 1

RICH 1 occupies the region $990 < z < 2165$ mm and covers the full LHCb acceptance (i.e. $\theta_x < 300$ mrad, $\theta_y < 250$ mrad stopping at $\theta_x = \theta_y = 25$ mrad). This can be seen in Figure 2.8. It is composed of two radiators: a 5 cm block of aerogel and an 85 cm region of decafluorobutane (C_4F_{10}) gas. The aerogel provides π - K separation up to 10 GeV/c and K^+ identification for particle momenta above 2 GeV/c. The C_4F_{10} gas provides further π - K separation up to 50 GeV/c.

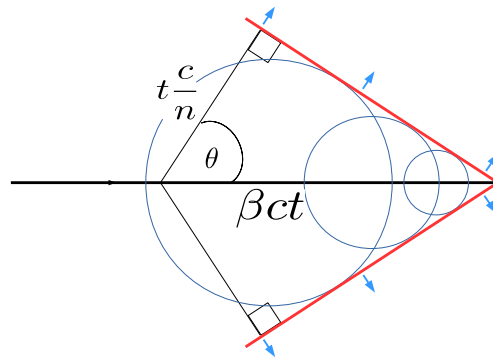


Figure 2.6: Schematic image of Cherenkov radiation [33]. Red line shows the shock front. θ is relative to the particle velocity.

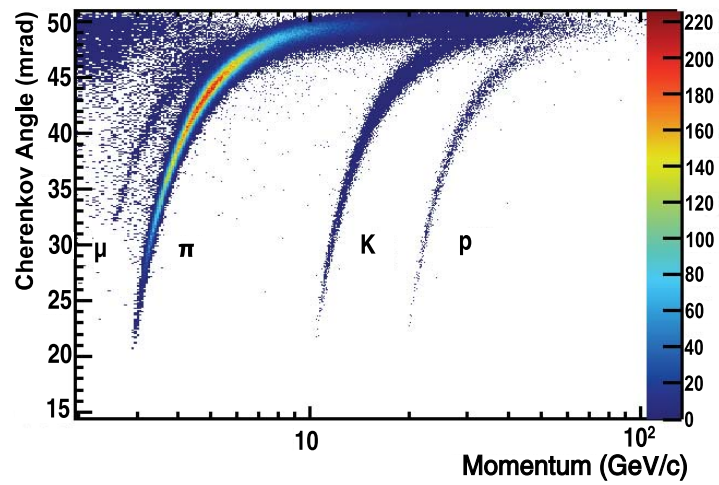


Figure 2.7: RICH ability to identify μ , π , K and p . This plot shows isolated Cherenkov rings only i.e. best case scenario. See text for more information. [34]

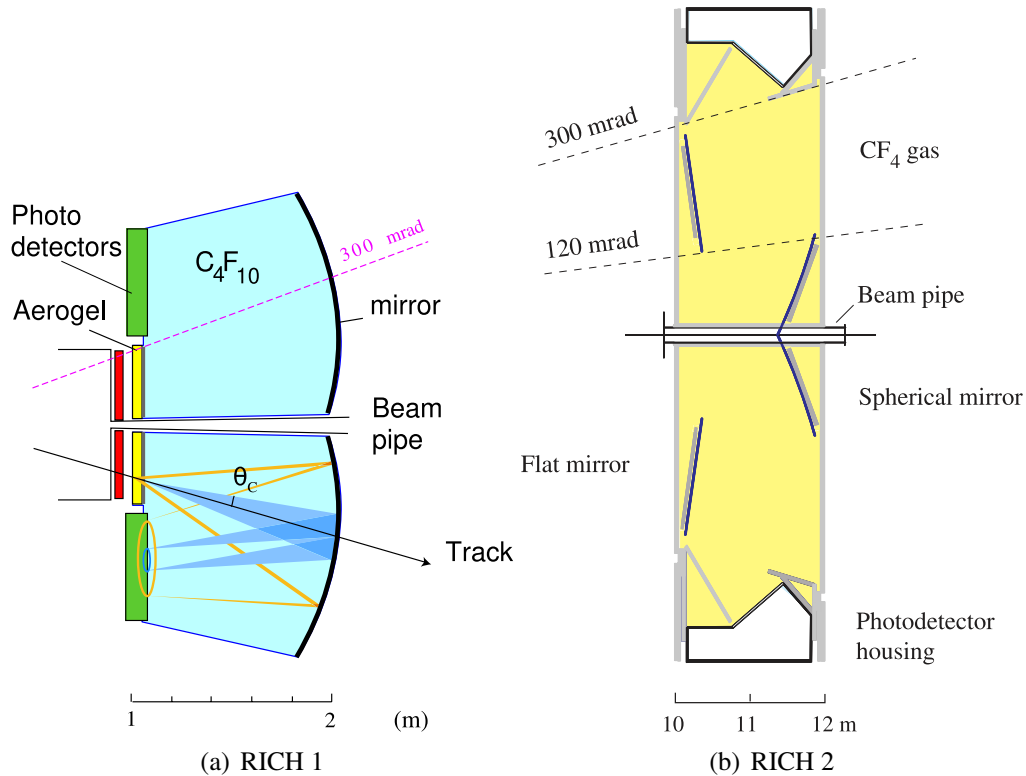


Figure 2.8: Schematic design of the RICHs (as seen from above) [35].

2.2.2 RICH 2

RICH 2 is placed at 9500 mm extending to a length of 2332 mm. It covers the angular range of $\theta_x < 120 \text{ mrad}$, $\theta_y < 100 \text{ mrad}$. RICH 2 is composed of a single 167 cm radiator composed of tetrafluoromethane (CF_4) which gives a π - K separation in a momentum range of around 50 GeV/c to 100 GeV/c.

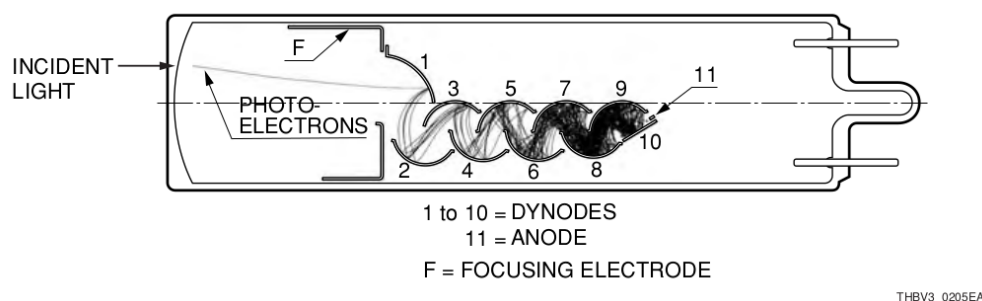


Figure 2.9: Dynode chain example from [36]

2.2.3 PMT

In considering the LHCb upgrade, it was decided that PMTs would be used instead of HPDs in the RICH. Studies to evaluate the longevity of PMTs that will be used in the upgraded LHCb for Run 3 (from 2021) are summarised in chapter 3.

PMTs have been a standard in particle physics photon detection for many years. Currently, the RICH upgrade team intends to use the Hamamatsu H12700 MaPMTs due to their high active-area fraction of 87%, radiation hardness and other features. The H12700 uses a linear-focused type of electrodes as can be seen in Figure 2.9. For more information, see subsection 3.3.1.

2.3 Bending magnet

LHCb uses a single iron yoke dipole magnet to measure momentum of charged particles. It has a bending power of 4 T m with a thickness of 10 m, as measured along the beam axis, allowing it to cover the full acceptance of ± 300 mrad horizontally and ± 250 mrad vertically. The momentum resolution provided by the magnet is 0.3 % to 0.6 % of the deflection of charged particles.

The magnet design allows for rapid ramping-up and inversion of the field polarity which allows the cancelling of systematic errors between bending directions. The non-uniformity of the B field is $\pm 1\%$ in the x - y plane of 1 m^3 from 3 m to 8 m in z .

2.4 Tracking systems

The tracking systems of the LHCb detector are the Tracker Turicensis (TT), T1, T2 and T3. The TT is composed purely of silicon microstrip detectors for high resolution measurement and is placed between RICH 1 and the bending magnet. T1, T2 and T3 are placed between the magnet and RICH 2. They are composed primarily of straw tube detectors, called Outer Tracker (OT), with a small region of silicon microstrip detectors around the beam pipe, called the Inner Tracker (IT), due to the high occupancy in that region. Straw tubes are used since they are much cheaper than silicon microstrip detectors and provide comparable accuracy in their kinematic region.

Since straw tube detectors only measure in one dimension, it is necessary to rotate some layers of the straw tubes in T1, T2 and T3. The first and last layers are parallel to the x -axis of the experiment, while the second and third layers are rotated by 5° and -5° respectively in order to measure the y -axis [37].

2.5 Calorimetry

Calorimetry detectors present in the detector are responsible for providing accurate information about the energy of decaying particles. They consist of the following parts

- PreShower Detector (PS)

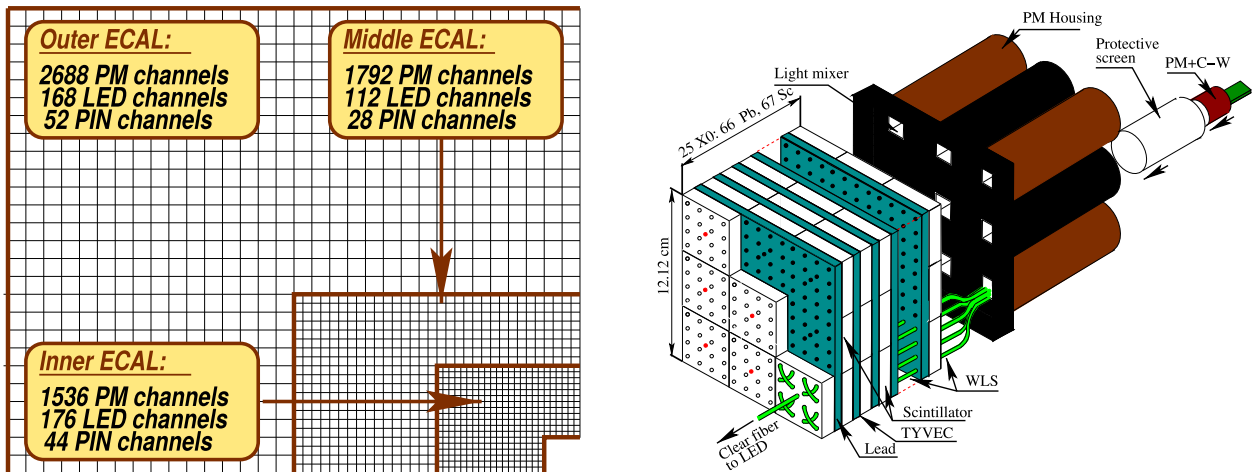


Figure 2.10: Schematic diagram of the ECAL [39]. (left) a schematic diagram of cell size. (right) an example of the inner section of the ECAL

- Scintillating Pad detector (SPD)
- Electromagnetic CALorimeter (ECAL)
- Hadronic CALorimeter (HCAL)

The PS and SPD work together to eliminate pion background from inelastic pp collisions. The SPD works to detect if a particle is neutral or charged and the PS differentiates between electrons and pions. The calorimetry system as a whole removes background events with high transverse energy (i.e. energy measured in the transverse dimension) electrons with a rejection level of around 99 % [38].

2.5.1 ECAL

The ECAL is a shashlik (i.e. with wires going through bored holes in the calorimeter, like a kebab), sampling calorimeter with alternating lead and scintillator layers with plastic WLS fibre readout.

This design [40] was chosen because of its good radiation hardness, fast response times as well as being well tested by other experiments [41]. The energy resolution of the ECAL is also a good feature and has been measured [38] to be

$$\frac{\sigma(E)}{E} \approx \frac{9\%}{\sqrt{E}} \oplus 8\% \oplus \frac{0.003 \text{ GeV}}{E}, \quad (2.3)$$

where E is in GeV. The terms are stochastic, constant and noise respectively.

The ECAL is situated at 12.5 m from the interaction point. Radially, it measures at $\theta_x < 300$ mrad, $\theta_y < 250$ mrad in line with the tracking system (see section 2.4). The inner acceptance is designed to avoid too much radiation from the beam pipe and so is $\theta > 25$ mrad. Since radiation drops sharply with distance (as a function of x and y), the ECAL is structured in 3 radial layers: inner (from $65 \times 65 \text{ cm}^2$ to $194 \times 145 \text{ cm}^2$), middle (from $194 \times 145 \text{ cm}^2$ to $388 \times 242 \text{ cm}^2$) and outer (from $388 \times 242 \text{ cm}^2$ to $776 \times 630 \text{ cm}^2$). In order to maintain more equal occupancy between the three layers the inner layer has more tiles than the middle, and the middle more tiles than the outer.

Along the beam axis, the ECAL is constructed of alternating layers of 2 cm lead, 120 μm white reflecting TYVEC [30] paper and 4 mm scintillator tiles. These measure 42 cm in the z -axis totalling 66 layers of lead and scintillator. This provides $25 X_0$ with a Moliere radius of 3.5 cm

Individual tiles of the scintillator are made from polystyrene admixtures of 2.5 % PTP and 0.01 % POPOP[39]. The tiles are injection moulded to provide the best coverage. The cell sizes for each layer are: 4.04 cm^2 for the inner layer; 6.06 cm^2 for the middle layer; and 12.12 cm^2 for the outer layer. This provides a more equal particle occupancy for each cell during run time.

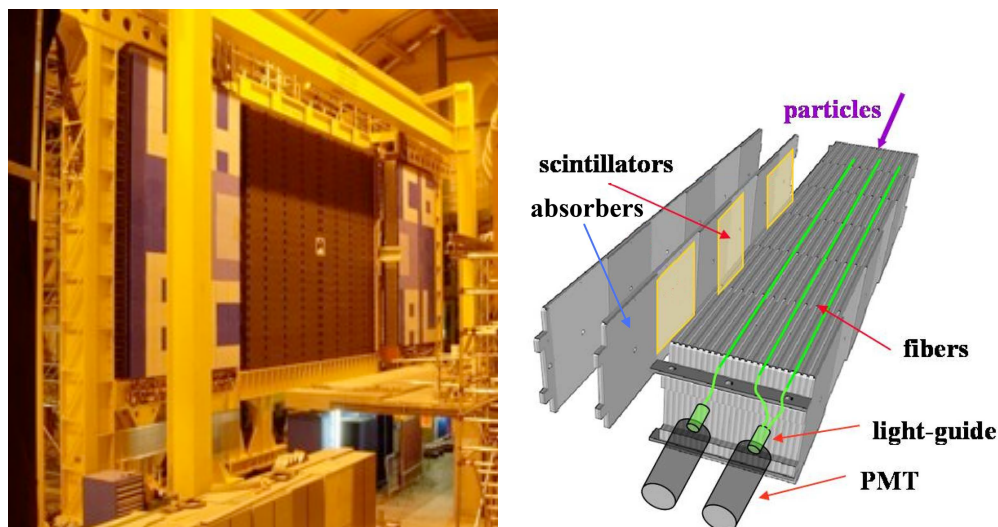


Figure 2.11: Schematic of the HCAL [30]. (left) Photograph of HCAL. (right) Schematic of individual cell(s).

Readout from the tiles is done via 1.2 mm diameter plastic WLS fibres and read into PMTs. These are looped so that light traverses the module twice while inside the module, with the loops outside the module.

2.5.2 HCAL

The HCAL is a sampling device of absorber and active material. The absorber is iron, and the active material is a scintillator. They are positioned parallel to the beam axis in alternating layers. The transverse width of the iron spacers corresponds to the hadron interaction length in steel. Light is collected in a similar way to the ECAL, via plastic WLS fibres and then fed into PMTs.

The HCAL is positioned 13.33 cm from the interaction point along the z -axis with dimensions of 8.4 m, 6.8 m and 1.65 m in x , y and z respectively. It is separated into two layers in the x - y plane: inner (4202 mm \times 3676 mm) and outer (8408 mm \times 6828 mm). In order to maintain more equal

occupancy between the two layers, the cell size in the outer layer is larger than the inner layer. The cell sizes are 131.3 mm^2 and 262.6 mm^2 for inner and outer respectively.

The internal structure of the HCAL is identical over the whole calorimeter, allowing cells to be constructed by connecting various layers to a single PMT. This structure can be seen in Figure 2.11.

The energy resolution of the HCAL is

$$\frac{\sigma(E)}{E} \approx \frac{(69 \pm 5) \%}{\sqrt{E}} \oplus (9 \pm 2) \%, \quad (2.4)$$

where E is in GeV. The terms are stochastic and constant respectively.

An novel feature of the HCAL is its ability to be absolutely calibrated. This allows for online calibration of other detectors by comparing the expected energy deposited in the HCAL compared to other detectors with simulated data.

2.6 Muon systems

The muon system of the LHCb detector provide essential muon detection. There are 5 stations (M1–M5), situated downstream of the interaction point. M1 is placed before the calorimeters, to aid measurement of transverse momentum (p_T), whereas M2–M5 are placed at the downstream end of the detector. M2–M5 are separated by 80 cm thick iron blocks that act as muon filters. Since muons are so penetrating, other particles are stopped by the iron blocks but muons are not. The muon stations use Multi Wire Proportional Chambers (MWPCs) except the inner section of M1 which uses Triple Gas Electron Multiplier (Triple-GEM) detectors (due to the high fluence incident on this region which lies close to the beam pipe).

The MWPCs act much like straw tubes in the tracking stations, being composed of an array of wires held at high voltage between two conductive plates. The gas in between the plates is a mixture

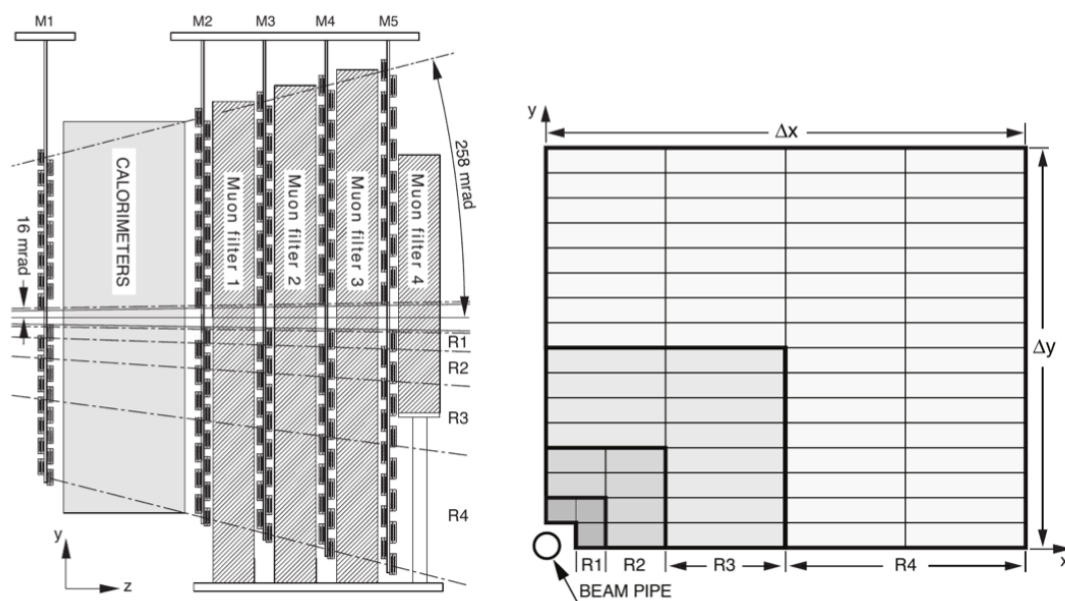


Figure 2.12: Schematic design of the muon stations [30].

of C_4F_{10} , argon and carbon dioxide in a ratio of 5:40:55 [37]. When a muon passes through the mixture, it ionises the gas and the ions flow towards the wire creating a signal.

The Triple-GEM detectors work on a similar principle to the MWPCs except that instead of an array of wires, the Triple-GEM detectors use small i.e. μm scale conductive rings around holes in polymer foils [42]. The holes act like pixels, attracting electrons from ionisation to well known locations in the detector providing precise hit resolution. The gasses inside are the same as the MWPC (C_4F_{10} , argon and carbon dioxide), but with a ratio of 40:45:15.

In order to keep the occupancy across each of the muon stations more equal, the stations are designed in concentric rectangles, R1–R4, as seen in Figure 2.12. The regions go from highest wire density to lowest from R1 to R4 ensuring that each part ages at roughly the same rate.

2.7 Trigger and stripping

The LHC operates with 40 million bunch crossings per second and one to two pp collisions per crossing, which is much too fast for the LHCb detector to read out all the data from. To combat this, triggers are used as a way to filter out uninteresting data.

First, the Level 0 trigger (L0), hardware based, online, is used to filter out the most obviously uninteresting events, down to ~ 1 MHz, then High Level Trigger 1 (HLT1) (software based, online) and High Level Trigger 2 (HLT2) (software based, offline) are used to whittle down the data to a rate of ~ 3 kHz.

2.7.1 L0

The L0 is a hardware trigger built into the LHCb detector. It has three parts: L0-PileUp trigger, L0-Calorimeter trigger and L0-Muon trigger.

The L0-PileUp trigger is only used for luminosity measurement.

The L0-Calorimeter trigger uses calorimetry information to cut on transverse energy. There are 3 trigger lines that use L0-Calorimeter:

L0Photon High transverse energy in PS and ECAL but no hits in SPD or HCAL

L0Electron High transverse energy in PS, ECAL and SPD but no hits in HCAL

L0Hadron High transverse energy in all calorimeters

The L0-Muon trigger utilises the muon stations and p_T to cut on muons. There are two trigger lines that use L0-Muon trigger:

L0Muon The track with the greatest p_T (above a preset threshold) also has hits in all 5 muon stations, forms a straight line towards the interaction point.

L0DiMuon As L0Muon, but the two tracks with the largest transverse momentum when multiplied instead of a single track.

2.7.2 HLT

The High Level Trigger (HLT) is a collection of software based triggers that can be changed much more easily than their L0 counterparts.

HLT1 is an online trigger system that uses additional information from the VELO and trackers to perform a partial reconstruction of the events. This can be used to validate cuts made at L0 and also make new cuts such as tightening constraints on the χ^2 and impact parameter of tracks.

HLT2 is an offline trigger system which runs on the same hardware as HLT1 with a lower priority, meaning that HLT2 triggers run only when HLT1 is complete. Since it has more time, a full reconstruction of the events are performed and cuts are based on the full reconstruction. Often, trigger lines at this level are quite specific, e.g. the analysis described in chapter 5 uses the Topo2BodyBBDT line which is a BDT trained to identify topologically two body decays.

2.7.3 Stripping

After HLT2, a further set of loose preselection cuts are applied called stripping lines. These selections are usually for specific analyses or groups of analyses and are run on the Grid in order to reduce the size of the dataset to a workable amount. The analysis described in chapter 5 uses the

StrippingBc2hhh_Kpypi_exclLine and StrippingBc2hhh_KKpi_exclLine lines[43] which are designed to catch 3-body B_c and B_u decays[44, 45].

2.8 ProbNN

ProbNN variables are a special feature of LHCb. They are not variables ‘straight out’ of the detector; they are Multi-Variate Analysis (MVA) results of several variables. Although they are not part of the detector, they are an intrinsic ingredient of analyses that depend on particle identification, combining information from multiple sources, at LHCb. The ProbNN MVA is trained on information such as: track momentum; distance from clones¹; RICH information; fit quality e.g. log-likelihoods, χ^2 ; and PID variables. The consistency of a given track with a specific hypothesis X is quantified using ProbNN _{X} variables where X represents the species of particle in question.

PID is used to distinguish between particles. For example, hadron identification uses the RICH by doing a log-likelihood fit to the readout with various hypotheses (K^\pm , p). These are then stored as PID_k and PID_p variables to be used later. Identifying kaons with the RICH has been found to have an efficiency of around 95 % (in the momentum range 2 GeV to 100 GeV), with a mis-id rate for mistaking pions for kaons at ~5 % [46].

2.9 Simulation

Simulated data provides many functions throughout this analysis including:

- signal training data for a Boosted Decision Tree (BDT), i.e. a multivariate discriminator
- assessing efficiencies on a given signal

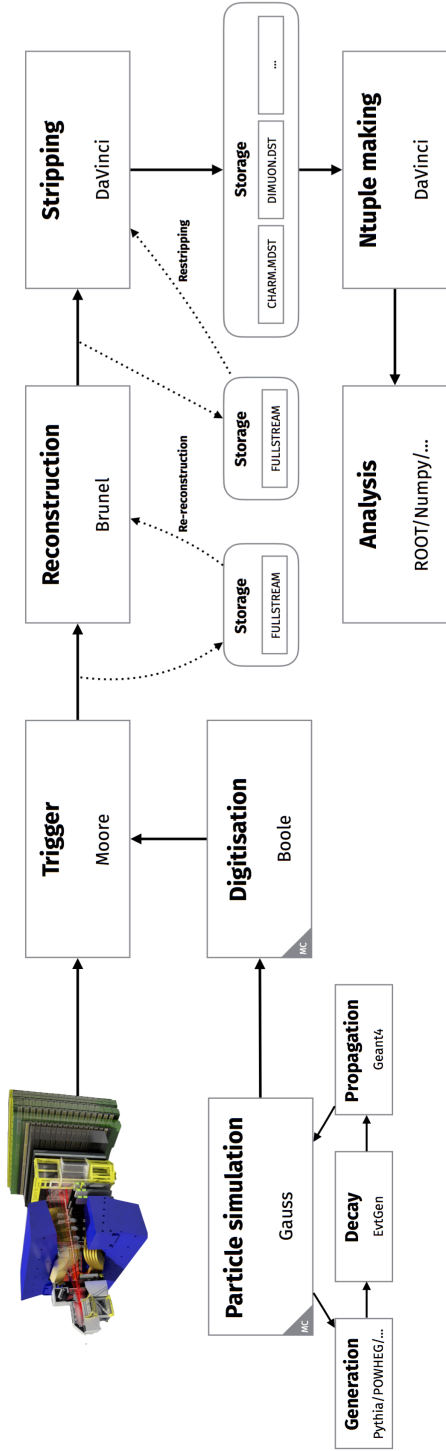


Figure 2.13: LHCb data flow [47]

- testing signal fit models without background
- testing signal fit models using current theories

The simulation framework used in LHCb uses several applications which can be seen in Figure 2.13.

For the simulation, the Gauss [48] framework manages the creation of events. This comes in three stages. First, generation of cross sections, exclusive kinematics and 4-momenta of particles for a given process: this can be with various generators. In the $B^+ \rightarrow K^{*0}(892)(\rightarrow K^+ \pi^-) \pi^+$ case, PYTHIA [49] was used to generate events. In the $B_c^+ \rightarrow \bar{K}^{*0}(892)(\rightarrow K^- \pi^+) K^+$ case, BcVegPy [50] was used. Second, decays are managed with EvtGen [51]. Finally, the events are propagated through the detector with Geant4 [52].

Once the physics of the events are simulated, the event is then digitised by Boole[53] to simulate what the detector would actually record given the physics of the event.

At this point, simulated data enters the data flow that data takes: Trigger (Moore [54]), reconstruction (Brunel [55]) and stripping (DaVinci [56]).

2.9.1 PYTHIA

This package[49] is a general purpose high energy physics generator. With support for both hard and soft processes from centre-of-mass energy of 10 GeV to 100 TeV, PYTHIA is the *de facto* standard for particle physics simulation. However, since it is aimed at a general audience, some more niche processes are provided by separate packages such as EvtGen.

The modelling in PYTHIA ranges from being ‘rigorously derived from theory’ [49] to heuristic phenomenological models that take inputs from data. This allows PYTHIA to provide good approximations of theoretical cross sections for processes including: QCD processes; Electroweak processes; and Fourth generation fermion production.

¹Clones are multiple tracks constructed from a single physical particle.

2.9.2 BcVegPy

This package[50] was developed in response to the need for fast B_c simulation due to increasing cross sections at the LHC [50]. It exploits the fact that the subprocesses of a B_c decay are always ‘hard’ and can be calculated to a good approximation with pQCD. This was achieved using the particle helicity technique [50]. This also has the added benefit that the cross sections of B_c mesons are calculated using full theoretical predictions i.e. without input from experimental data.

2.9.3 EvtGen

This package[51] manages the decays of generated events (in this case generated by PYTHIA or BcVegPy). It contains implementations of decays from theoretical models.

EvtGen’s handling of decays is more complex than PYTHIA in part because it considers amplitudes instead of probabilities. This allows it to calculate interference between various resonances and improves the ability to calculate non-trivial decay time distributions for CP-violating decays.

Using this package, it is possible to override the default behaviour of simulating all possible decays. This functionality is often used to force a single decay chain; signal simulated data is generated by specifying only a single possible decay chain and passing this to EvtGen. In the case of the analysis of this thesis, this is the method used to generate signal-only simulated data.

2.9.4 Geant4

Geant4[52] is a toolkit for simulating particles passage through matter. In use across disciplines it is a mature project with a solid and well tested code base.

Once the particles are generated with PYTHIA, etc., it is necessary to simulate their passage and interaction with the detector. To aid this, the detector is represented as a hierarchical eXtensible Markup Language (XML) structure which can be switched off in sections (e.g. testing only the VELO or removing the HCAL and replacing it with iron).

Geant4 simulates the passage of particles by allowing particles to travel a certain distance (known as *steps*). The ideal distance of a step is a compromise between speed and accuracy since the shorter the steps, the more accurate the results but longer the simulation. The probability that one of the allowed interactions, for the particle traversing the material at a given energy, taking place is the primary consideration when considering an acceptable step size through a material.

LHCb maintains a slightly modified version of Geant4 in order to adapt it fully to the experiment's needs.

2.9.5 Boole

Once the particles have fully undergone simulation (including fragmentation and hadronisation) the events are digitised to match the detector response.

Digitisation is the process whereby events are taken from their 'analogue' state (as simulated events where their properties are known to an arbitrary precision) and the detector responses to the events are simulated. This records the events as hits in the detectors and therefore become digital (in the sense that they are recorded as signals)

As it is possible to completely know simulated events, so-called 'MC Truth' is recorded so that analysts can compare the reconstructed (see Brunel, subsection 2.9.7) particle id with the true particle id.[53]

2.9.6 Moore

Since the L0 LHCb trigger is hardware based, it is necessary to simulate the trigger for simulated data. HLT1 and HLT2 are part of the Moore project[54].

2.9.7 Brunel

Brunel[55] is responsible for reconstructing events recorded in the detector into tracks which can take on physical meaning, e.g. particle id. It is also responsible for resolving clusters, e.g. when two particles hit a single cell of a detector at the same time. The data generated by Brunel is then passed to other analysis software and made available to the user.

By comparing simulated tracks and reconstructed tracks, it is possible to calculate a reconstruction efficiency so that the true rate from the detector can be estimated.

2.9.8 DaVinci

DaVinci[56] is an analysis framework specific to LHCb with many LHCb specific tools. It is primarily used in reducing data from Brunel into a manageable size for individual analysts to manipulate. It does this by using pluggable algorithms to perform complex calculations on the grid and returning the results to the user. Examples of algorithms used are:

- Mass substitution for wrongly identified particles (e.g. swapping the mass of a K with a mass of a π)
- Recording the results of the triggers as boolean data types

- Reconstructing particles not explicitly present in the original simulation e.g. particle resonances

Although it is theoretically possible to do all analysis using only DaVinci, it is more practical to use DaVinci only for heavy workloads which can be distributed over several computing nodes. Since DaVinci is a framework—i.e. it works by calling the code of the user, not by being called by the user—it is difficult to use interactively.

Chapter 3

PMT ageing validation

As part of the upgrade to the RICH, the HPDs are due to be replaced with PMTs. Investigation of the Hamamatsu R12699 (HA0023) is described in this section. These devices have already been proven to be sufficiently radiation hard for the expected particle fluences but their characteristics are not yet sufficiently understood. The series of tests described below measure how the anode efficiency changes with particle fluence.

3.1 Prior work

Previously in [57], the R12699 PMT was tested and found to have some counter-intuitive behaviour after long illumination periods (see Figure 3.1); the gain variation described by [57] has been found to improve with age, whereas typically PMT performance deteriorates with age. In the paper, it is

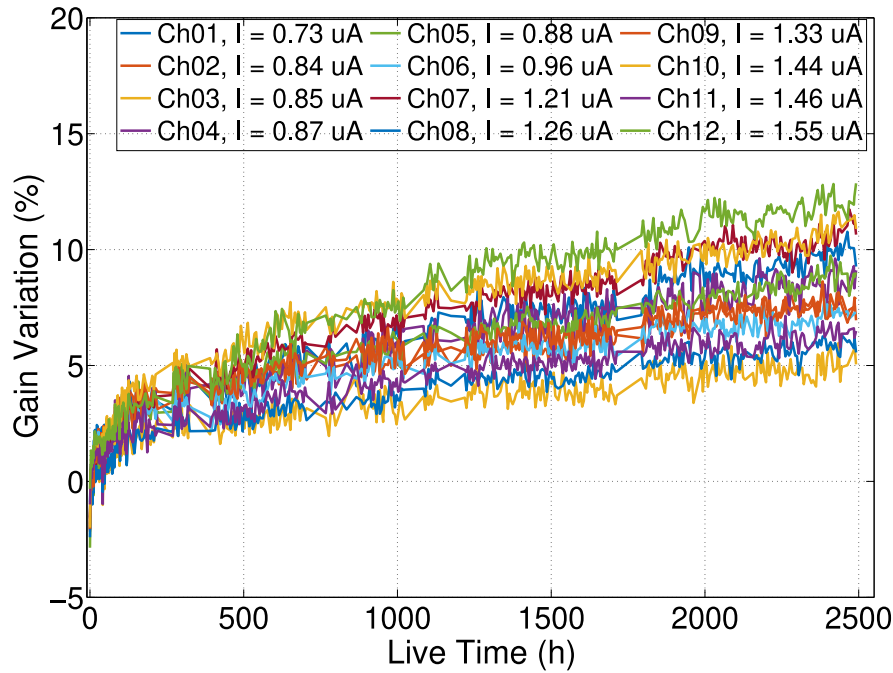


Figure 3.1: Gain variation vs. illumination period as found in [57] for the PMT. This improvement in anode sensitivity was an unexpected effect of ageing.

posited that PMTs from different batches may have different behaviour due to a difference in the thickness of the caesium layer grown on the dynode surfaces. The aim of the new investigation into the Hamamatsu R12699 (HA0023) described in this thesis is to improve understanding of this behaviour.

3.2 Motivation

The active elements of the LHCb RICH detectors are PMTs. Since the proposed operational period of the PMTs are significantly shorter than the proposed operational period of the experiment, some of the PMTs will need to be replaced. It is difficult to test individual PMTs during running,

therefore it is necessary to have an estimate of when they will fail and have an understanding of their behaviour under the fluences experienced at the LHC. Testing the PMTs in this way allows us to provide a reasonable timeline for replacement of PMTs and allows for their operational parameters to be adjusted as time goes on, e.g. for a change in voltage to maintain the same gain and hence efficiency.

3.2.1 Ageing

The ageing model introduced in [58] provides a good basis for understanding the ageing or loss of anode sensitivity (sometimes called ‘reduction of secondary emission ratio’ [36]) within a PMT, proposing that the ageing of a PMT is a function of the current output level, working history and dynode materials, especially the secondary emissive surface of the dynode.

As PMTs are produced in a wide variety of designs and can withstand relatively different working conditions it is only possible to state relatively general rules for ageing. It is likely that the secondary emissive surface of the dynode, the purpose of which is to increase the secondary emission of electrons, is responsible for variations in ageing behaviour as this layer is subjected to a high level of initial bombardment and subsequent emissions.

During the working life of a PMT, there is generally a period of stability followed by a period of deterioration. Once the period of stability is over, the gain on the PMT, or more specifically the dynodes, begins to change due to damage to the secondary emissive surface of the dynode. This can be for a number of reasons, such as helium diffusion through the glass or changes in charge distribution. The most commonly attributed cause of damage to the secondary emissive surface is the continuous sputtering action of the layer behind which it is located; in the case of the R12699,

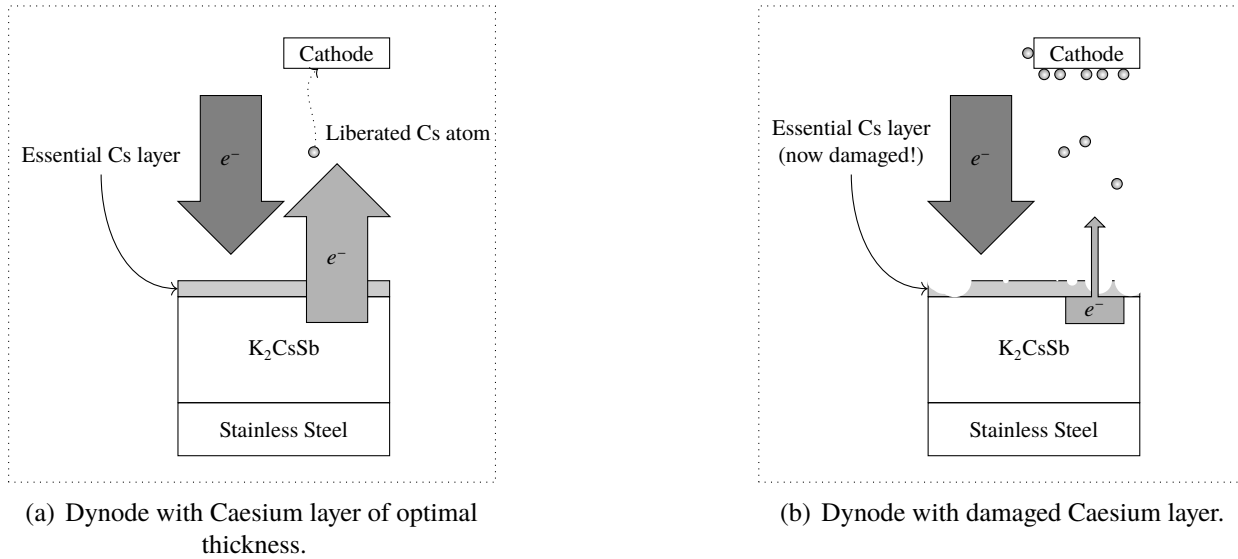


Figure 3.2: How the caesium layer becoming damaged over time causes the gain to go down in the PMT with ageing (see down-drift mode in subsection 3.2.1).

this is a layer of K₂CsSb. This sputtering increases with current, which provides more electrons making integrated current over time, is one of the greatest predictors of damage.

Taking into consideration the recent literature on the ageing of PMTs (including [57, 59]), two modes can be put forward for this deterioration: the down-drift mode (see Figure 3.2) and up-drift mode (see Figure 3.3).

In the case of the down-drift mode, the secondary emissive surface starts at the optimal thickness for the efficiency of secondary emissions, but is slowly damaged by the sputtering of the previous layer meaning that the efficiency of secondary emissions drops. In most cases, this can be accommodated by increasing the gain on the PMT to compensate for the loss of efficiency.

In the case of the up-drift mode, the secondary emissive surface of the dynode is deeper than the optimal thickness meaning that it serves to block electrons from leaving the surface (as well as

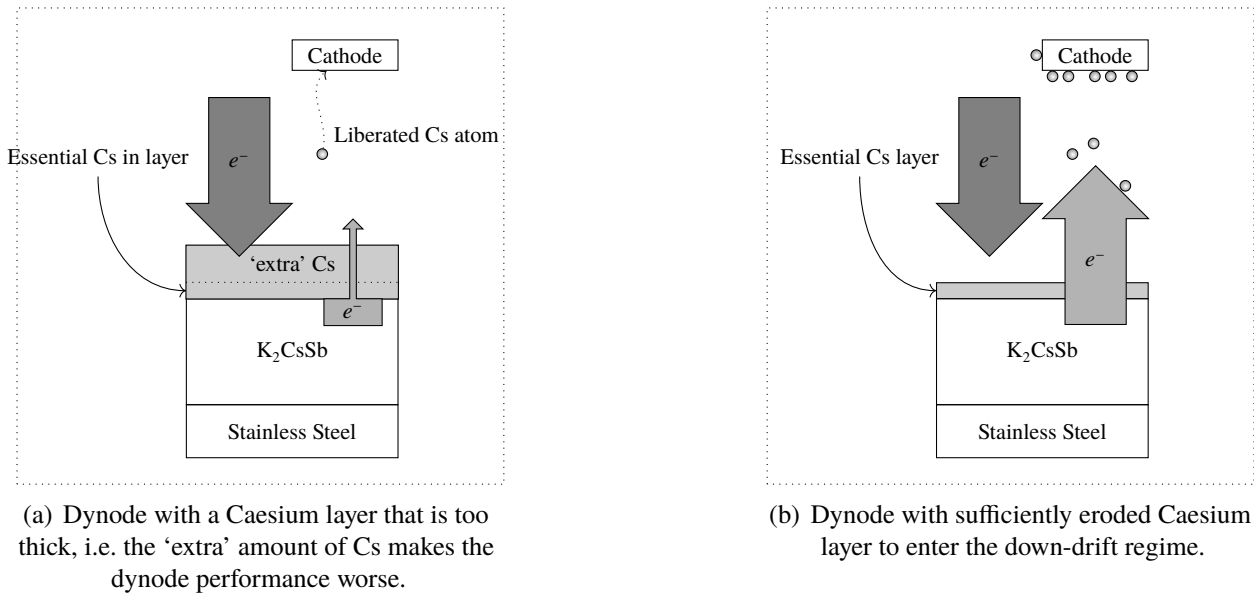


Figure 3.3: How an excessively thick caesium layer causes the gain to go up in the PMT with ageing (see up-drift mode in subsection 3.2.1)

providing a limited boost to secondary emissions). The damage suffered by the secondary emissive surface leads to an erosion of this extra thickness leaving (roughly) the optimal thickness for the most efficient secondary emissions. The dynode then behaves as the down-drift case.

While it is difficult to state whether the ageing process described in this section is correct i.e. up-drift and down-drift models, it is a plausible model, accounting well for the variation between batches of PMTs.

3.3 Experimental setup

The tests described in [57, 59] were carried out for an equivalent operational period comparable with the operation of Run 3 of LHCb, where an equivalent operational period aims to keep the total

luminosity the same (i.e. double the rate, halve the time, etc.). The aim of this test is to establish the extent to which the R12699 studied supports the up-drift/down-drift behaviour described in [58]. The experiment was designed to at least match the equivalent operational period of [57, 59].

The experimental setup can be seen in Figure 3.4. The internal setup is comprised of a laser, plastic (to diffuse the laser beam), PMT and ageing LED.

The laser is a model PiL040X from Advanced Laser Diode Systems [60] operating at a wavelength of (406 ± 5) nm, attached to a power source (EIG2000DX, came with PiL040X) which triggered by an Agilent Technologies 81150A Pulse Function Arbitrary Generator [61] set at

$$(1.000\ 000\ 000\ 0 \pm 0.000\ 000\ 000\ 5) \text{ kHz.}$$

The laser is only switched on during data taking.

A white ageing LED is used for the ageing as the lifetime of the laser is significantly less than the expected operational period of the experiment. Since every change to the experimental setup, e.g. replacing the laser, requires recalibration and introduces systematic errors, an LED was used as it is expected to last much longer than the operational period. In addition, the cost of a new laser is ~£100 which would raise the cost of the experiment for every time it would need replacing.

A plastic block is used to diffuse the laser so that the PMT pixels have more equal exposure during data taking. Without the plastic, the laser beam would have been too focused and only a few pixels would have usable measurements.

The PMT described in subsection 3.3.1 is connected to a local PC with an embedded Data Acquisition Unit (DAQ) (a prototype of the V1729 by CAEN [62]). The data are received as binary input, which is then recorded in a custom binary format using software written for this experimental setup by Tonino Sergi.

Since the signals from the PMT are analogue and the DAQ requires digital input, a AN308/NL Analogue to Digital Converter (ADC) [63] is used.

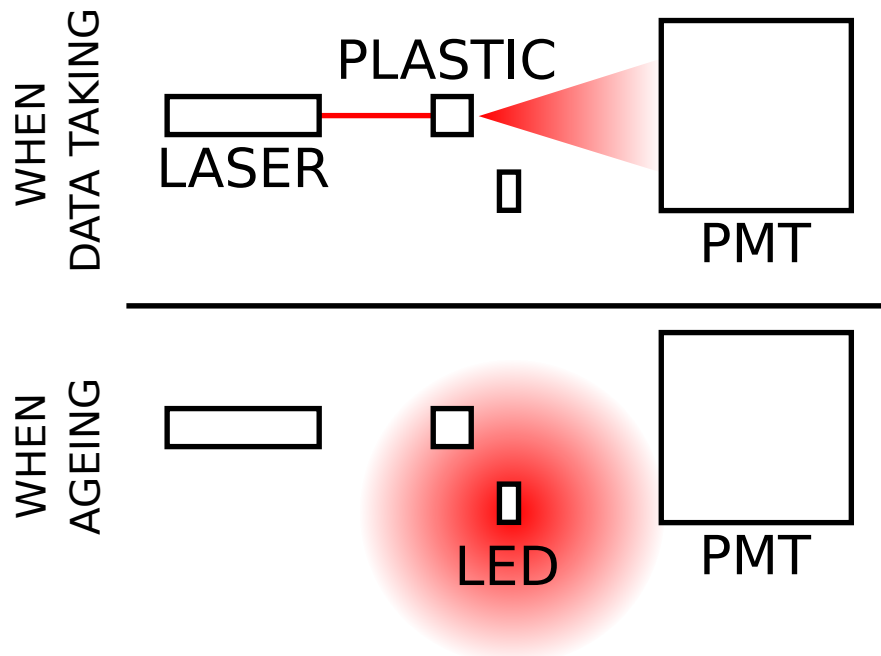
The V1729 prototype DAQ only has three available channels available (Channels 1, 2 and 3) and 8 channels of the PMT were being read out (see Figure 3.5), so signal was time multiplexed with cables of various lengths to delay the signal. These timed cables came in three types: 3 ms, 16 ms and 32 ms. These channels were then named as '*(physical channel).(time-multiplexed channel)*', i.e. for the channel 1.1, there is a delay of 3 ms; for the 2.2 and 3.2 channels there is a delay of 16 ms; and for the 2.3 and 3.3 channels there is a delay of 32 ms. These signals are then passed to the PC, where the output is recorded locally during individual runs of the test for later analysis.

3.3.1 R12699 PMT

The PMT used for this experiment is the R12699 from Hamamatsu [64]. It is a 64-channel, square Multi-Anode PhotoMultiplier Tube (MaPMT) measuring $52 \text{ mm}^2 \times 52 \text{ mm}^2$. It has an $8 \text{ pixel} \times 8 \text{ pixel}$ matrix: each cell being $6 \text{ mm}^2 \times 6 \text{ mm}^2$ attached to a 10-stage dynode chain (as seen in Figure 2.9). These are attached to a borosilicate or UV glass entrance window which is used in conjunction with a bialkali (antimony-potassium-caesium, K_2CsSb) photocathode.

It is particularly suitable for high energy physics experiments due to its: low dark count rate; only moderate amount of cross talk; and small borders allowing for close packing (approximately 87% effective area).

The R12699 is different from its counterpart the H12700 in that the output pins are directly connected to the anodes of the photocathodes. This means that a custom voltage divider must be constructed (in this case, it was designed and built in-house).



(a) Experimental setup for the PMT testing. (Not to scale).



(b) Experimental setup for the PMT testing.

Figure 3.4: Long-term PMT ageing experiment.

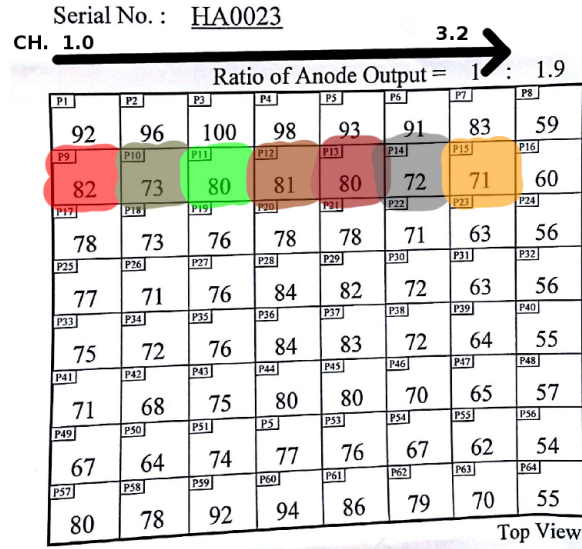


Figure 3.5: Pixel positions on the PMT. The channels are coloured red and yellow and green and brown and scarlet and black and ochre for channels 1.1, 2.1, 2.2, 2.3, 3.1, 3.2 and 3.3 respectively. The PMT was positioned with channel 1 at the top and channel 3.2 at the base.

3.4 Method

The PMT was aged using an LED as detailed in section 3.3. The LED was run continuously using a signal generator to allow regulation of the incoming current to the PMT. Measurements of the PMT response, i.e. a ‘run’, were taken approximately on a daily basis. During each run, the LED output was stopped using the signal generator, then the laser switched on for a 30 minute period while data were recorded to the local PC (see section 3.3).

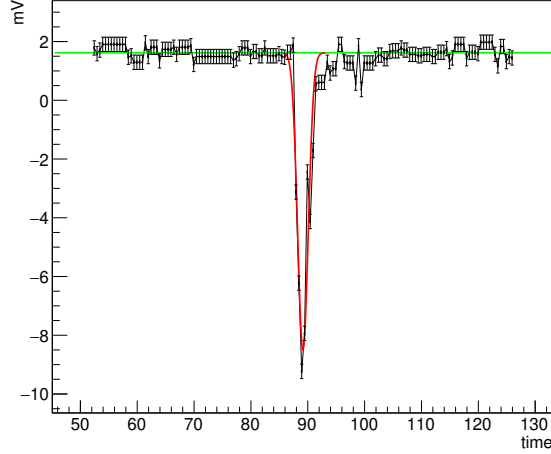


Figure 3.6: An example of pulse height measurement

3.5 Analysis

The purpose of the analysis is to measure the gain over time, which is expected to vary due to the deterioration of the dynodes. To do this, the peak gain was measured approximately every day (with a few exceptions for power outages, etc.).

The data were analysed offline in several stages. First, the pulse height of the charges collected by the PMT (see Figure 3.6) is measured by fitting a Gaussian trough to a histogram of collected charge vs time. The height of these peaks are then used to fill a histogram (one per channel per run, see section 3.4) and plotted. As discussed in [65], the histogram should naturally be in the shape of a Polya function,

$$P(Q) = C_0 \frac{(1 + \theta)^{1+\theta}}{\Gamma(1 + \theta)} \left(\frac{Q}{\bar{Q}} \right)^\theta \exp \left(-(1 + \theta) \frac{Q}{\bar{Q}} \right), \quad (3.1)$$

where the peak gain, b is defined as $\frac{1}{1+\theta}$. The peak voltage (b) was then plotted against lab time (Figure 3.7) and LHCb time (i.e. the time a PMT would be inside LHCb continuously operating at Run 3 luminosities to experience the same fluence, see Figure 3.8).

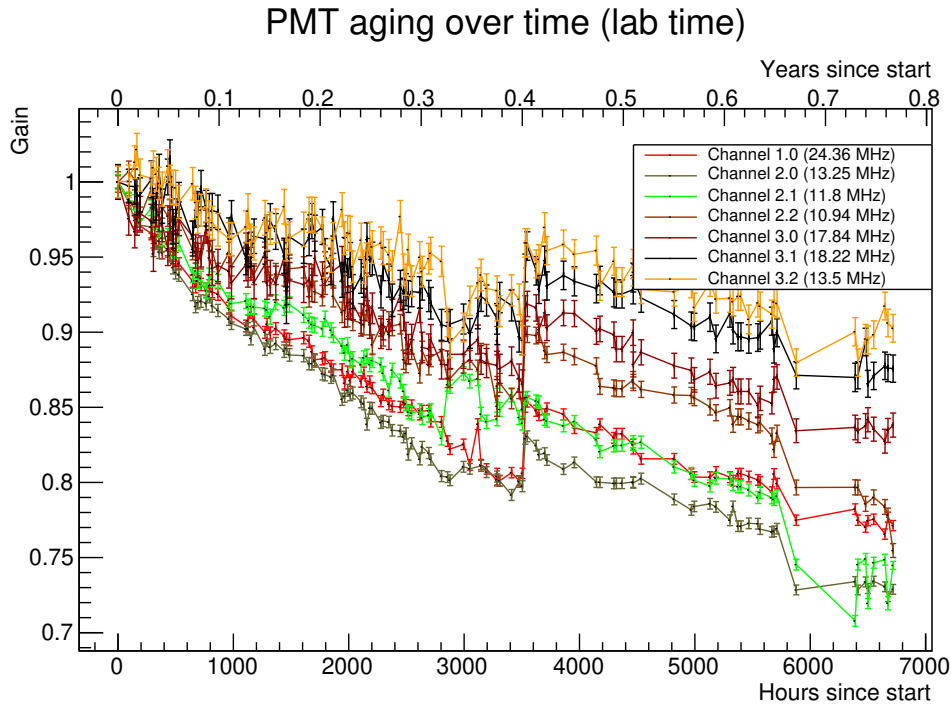


Figure 3.7: Gain vs. lab time for PMT testing. The jump at ~ 3500 lab hours is due to grounding the pins of the PMT.

3.6 Results

As can be seen from Figure 3.7 and Figure 3.8, the loss of anode sensitivity (i.e. the effects of ageing) of this PMT was found to follow a downward trend, possibly indicating that different batches of R12699 PMTs may have different behaviours. At the very least it demonstrates that the upward trend found in [57] is not true for every R12699 PMT.

In addition to this, the integrated luminosity measured compared to [57] is approximately 4 times as much¹, meaning the loss of gain is well within the $\sim 20\%$ per 3000 hours of intense illumination found previously.

¹Calvi et al. quote their rate per pixel as ‘a few MHz’, where our experiment had 10 MHz and ran for twice as long.

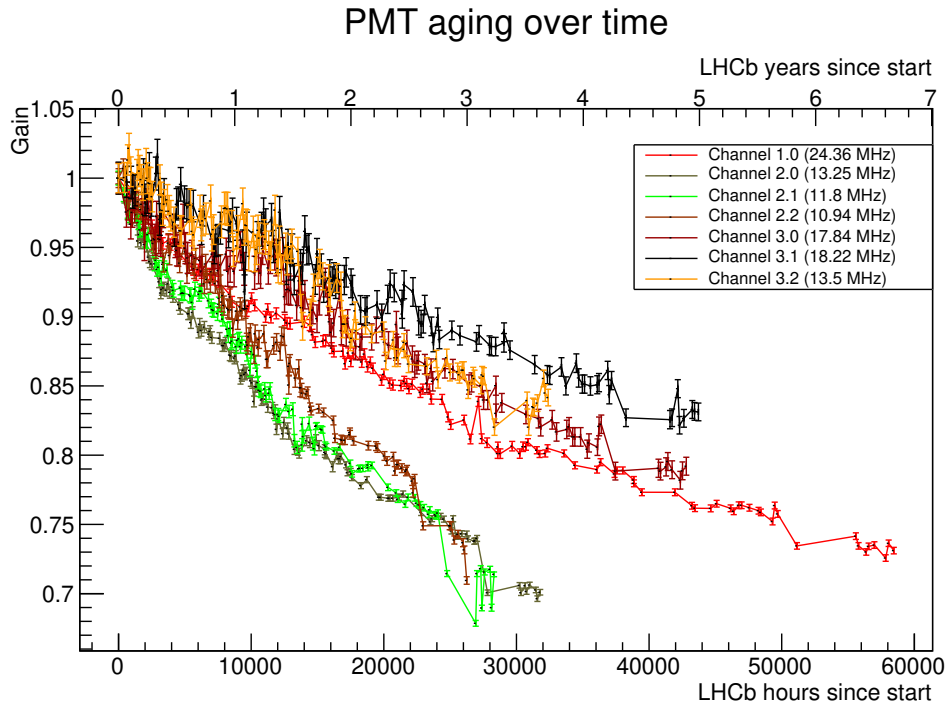


Figure 3.8: Gain vs. effective LHCb time for PMT testing. In this plot, the jump at 3500 lab hours due to grounding has been corrected. (see Figure 3.7)

Figure 3.8 shows that, at least naively, the PMTs should not suffer a loss of gain more than 30% over 3 years, with many pixels surviving much better than that over time. However, since the incompatibility between the results found here and the results in [57] casts doubt on the predictability of behaviour between batches, individual tests on batches used in the LHCb upgrade will provide a better predictor of the loss of gain over time.

Chapter 4

LHCbPR

The simulation work at the LHCb experiment is complex with large amounts of code being edited every day. With large software projects it is possible for code to become too large/interconnected to fix in a reasonable amount of time. One way to tackle these kinds of problems is writing tests. Modern projects, such as Geant4 [52], favour a Continuous Integration (CI) based approach using Test Driven Development (TDD) which leads to more modular and more robust code. Greater test coverage means if a bug is introduced it is spotted earlier and easier to debug. With older code bases, converting to using TDD involves considerable work as code can easily become ‘spaghetti code’ which is affected by a weak copy of the hierarchy problem: small changes in seemingly innocuous places can have vast and unpredictable effects, with changes to the oldest code often having the worst effect.

In addition to the age and complexity of the code, meaningful tests of simulation software are often on the scale of hours and days instead of a few seconds. This means that running the tests after every commit, as with traditional CI workflows, is impractical.

To solve this problem, LHCb Progression and Regression suite (LHCbPR) was created as an automated test framework with a web interface for test authors to see easily the effects their changes would have. Version 1 of LHCbPR was a single monolithic application which started to become difficult to develop due to its size (falling victim to the very problem it sought to solve). For version 2 of LHCbPR, containers were used to separate each part of the software, each responsible for individual functions. This kind of architecture is usually referred to as a microservice architecture.

This section details each of these microservices: LbNightlyTools (subsection 4.3.1), LHCbPR2BE (subsection 4.3.3), LHCbPR2ROOT (subsection 4.3.4), LHCbPR2HD (subsection 4.3.2) and LHCbPR2FE (subsection 4.3.5).

4.1 Prior work

The previous version of LHCbPR was a single, monolithic application. This had several drawbacks: rapid redeployment of individual components, such as the web interface, required the entire application be restarted; adoption of new technology required changing the entire stack; boundaries between components were very easy to break; and the large code base was intimidating for new developers and required current developers to check their changes would not break across a much larger target.

This monolithic approach was initially used because it makes prototyping easier.

4.2 Microservices

Microservices avoid the common problems of monolithic applications by using many applications (called microservices) in tandem, all of which can use a different stack and be run on different systems, often through containerisation of some kind. The benefits include: different stacks mean that developers of individual microservices can pick technologies best suited to the task; developers only need to understand a single microservice's code to start editing it, making it much easier to pick up and continue to develop; and individual microservices can be restarted in production without disrupting other microservices (e.g. the front end can be redeployed several times a day without ever restarting the test database). However, the strengths of microservices can quickly turn into weaknesses. If a developer from a single microservice wishes to contribute to another they likely have to learn a new stack. Testing the whole is also more difficult since microservices, by design, are independent from one another i.e. separate repositories, separate machines, etc. which makes it difficult to write a single test that covers the whole application.

4.3 Individual microservices

This section lists the individual microservices that make up LHCbPR.

4.3.1 LbNightlyTools

The LbNightlyTools [66–68] package was designed as a test scheduling system which uses Jenkins CI. It calls the LHCbPR2BE Application Programming Interface (API) in order to store results in LHCbPR for later use.

When talking about LbNightlyTools, it is useful to define several terms: a *slot* is a ‘consistent stack’ of software [67] and a *platform* is the base including the OS, flags and compilers. By using configurations of slots and platforms, it is possible to test specific stacks of software against a wide variety of targets.

A flow diagram of the LbNightlyTools system can be found in Figure 4.1.

4.3.1.1 Configuration

Config files that drive the tests are written in an XML format [68], and these files configure the slot(s), platform(s) and build options. The specific XML format also supports wildcard expressions for platforms such as `x86_64-s16-gcc*-*` for matching `gcc46` and `gcc48` builds

4.3.1.2 Checkout

Checking out the code is done on a per project basis via a customisable Python function [67, Section 4.1.2]. Usually this involves checking out the most recent code from git or downloading a source tar file. All the files created by the checking out process (known as *artifacts*) are stored in a directory for later use.

4.3.1.3 Building and testing

For the nightly system, building and testing are interdependent. Often, LbNightlyTools is the first test indicating whether a project will function (usually by testing the build process). Generally speaking, building and unit tests are carried out entirely within LbNightlyTools while the results of larger integration tests are done in LbNightlyTools and the results are passed on and displayed in to LHCbPR.

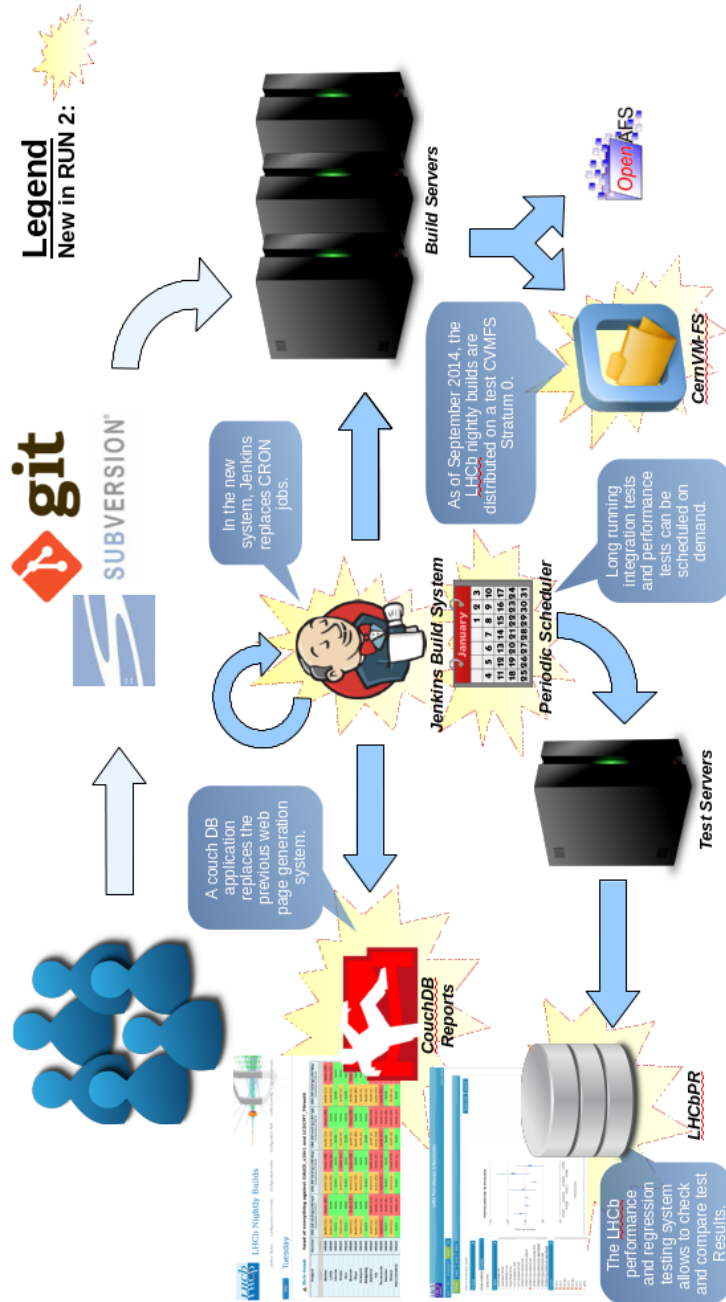


Figure 4.1: LHCb Continuous build and integration system [66].

Currently the build status of projects is not integrated into LHCbPR, but a dedicated dashboard, see subsection 4.3.1.5, is available to see the build status of various jobs, as well as logs for failed build/tests.

4.3.1.4 Jenkins configuration

Jenkins is an off-the-shelf open source CI system which is used as the basis for LbNightlyTools. Although out of the box Jenkins did not have all the features needed for LbNightlyTools, it was possible to extend it with several plugins which allowed for a feature complete system [67, Section 4.2].

Jenkins uses a system of *jobs* (referred to as Jenkins jobs for this section) to drive similar tasks with configurable inputs. Some examples of this are: starting and running individual tests, configuring individual slots, scheduling tests for running and running the customised python function for checkout (see subsection 4.3.1.2). Since Jenkins jobs are machine independent, they can be used to distribute the workload across multiple *workers*, where workers are the host machines of the tests. This is useful as one explicit goal of LbNightlyTools is to be able to run tests across multiple platforms which can include different processors and other hardware.

In addition, the use of a Jenkins job for configuring slots means that if there is a change to a slot (e.g. a version change in part of the software stack for a slot), a rebuild of all the tests using that slot can be triggered via the dashboard or the job scheduler [67].

4.3.1.5 Dashboard

In order for LbNightlyTools to be useful, users need to have easy access to logs and reports on the success or failure of builds and tests. For this, a web based dashboard has been created that presents the status of builds and tests.

The dashboard has been carefully designed with two main functions in mind:

- provide a filtered summary of individual/multiple slots with graphs
- provide easy access to build logs to get specific information on build/test failures

The filtered summary allows users to see quickly if there are any general problems or if there are any tests taking significantly longer than usual (see Figure 4.2). This online analysis of the current build situation is important because if resources are being held up by errant code e.g. infinite loops, etc. then immediate action needs to be taken to make sure that the nightly build systems do not fall behind.

The specific information provided includes: access to the build machine (if it still exists) and build logs.

In order to have this information available when needed, the dashboard maintains a CouchDB database that holds all the information on the tests which LbNightlyTools is responsible for. CouchDB is a schema-less database which allows for flexibility in storing different data types for each test. The downside of schema-less databases is that access speed can be slower than schemed databases. To mitigate this, the dashboard database is regularly indexed with the appropriate keys [67].

4.3.2 LHCbPR2HD

In order to maintain flexibility, the output of jobs in LbNightlyTools may take any form (ROOT files, csv output, etc.). Since the front end requires a consistent data format, a database of results

CERN Accelerating science Directory Sign in

LHCb LHCb Nightly Builds

Search All slots

Nightly builds Release builds Periodic tests Nightly dashboard CVMFS installation status Testing builds External links ▾

Thursday 2018-03-08 Wednesday 2018-03-07 Tuesday 2018-03-06 Monday 2018-03-05 Sunday 2018-03-04 Saturday 2018-03-03 Friday 2018-03-02 Select a date Show filters

lhcb-2016-patches - build: 687 Compare with previous build Compare with other slot Browse files

Test slot with patches for 2016 production stack available on: cvmfs

Project	Version	x86_64-slc6-gcc49-opt		x86_64-slc6-gcc49-dbg	
		build	tests	build	tests
LHCb	2016-patches	build	tests	build	tests
Lbcom	2016-patches	build	tests	build	tests
Rec	2016-patches	build	tests	build	tests
Brunel	2016-patches	build	tests	build	tests (14)
Phys	2016-patches	build	tests	build	tests
Hlt	2016-patches	build (2)	tests	build (2)	tests
Moore	2016-patches	build (13)	tests (12)	build	tests (6)
Online	v5r31	build (2)	tests (16)	build (2)	tests (17)
MooreOnline	2016-patches	build	tests (2)	build	tests (1)
Analysis	2016-patches	build	tests	build (1)	tests
DaVinci	2016-patches	build (405)	tests (17)	build (405)	tests (22)

Figure 4.2: LbNightlyTools screenshot

is created with an entry for each test run, along with its associated test conditions (compiler, architecture, etc.). Since the data can take any form, simple translation classes are written in Python called *handlers*. Handlers inherit from a base Python class that provides various methods for storing results as integers, floats, strings, JavaScript Object Notation (JSON) and ROOT files. The database entries are then emitted from the handler as Python dictionaries and stored in the database using the API provided by LHCbPR2BE.

Test authors are usually very familiar with Python classes, which makes using python classes as handlers a low barrier to entry into the LHCbPR system.

4.3.3 LHCbPR2BE

This microservice contains the production database mentioned in subsection 4.3.2. Its strengths include exposing data via a custom API designed for LHCbPR which means developers do not need to spend time learning raw SQL commands.

The disadvantages of this approach lie in its strengths: raw database access is not possible outside of the container e.g. from the web front end, so fine grained control of the data returned is not possible. This leads to inefficient response times because data are not tailored for each application using the database. However, this is not usually a problem since LHCbPR2BE code is generally simple to extend for specific applications if needed.

Another of the advantages of the microservice architecture is that the internal structure of LHCbPR2BE can be completely changed (i.e. the database technology can be swapped out) while maintaining the API e.g. a change from schema based to schema-less based database would be transparent to services outside of the container.

4.3.4 LHCbPR2ROOT

One of the explicit aims of LHCbPR is to present test results in a web browser in a meaningful, human-readable way. Often this includes an online comparison of data when the data being compared are not known, to the developer, before the user chooses the test runs to view e.g. plotting trend lines of values from multiple test runs or plotting many graphs on one set of axes. While it is technically possible to do full analyses using JavaScript, the development time needed to implement this is prohibitive and can be CPU intensive for the client. Tasks like analysis are much easier in

Python so this microservice provides a way for developers to compare data using Python and serve it via an API (usually in JSON form).

This project is a simple Python Flask server which has custom endpoints for specific analyses, usually using ROOT.

The functions of the API provided by LHCbPR2ROOT include: converting ROOT internal file structure to JSON; comparing histograms by dividing, multiplying, adding and subtracting; plotting multiple graphs on a single pair of axes; perform Anderson-Darling, χ^2 or Kolmogorov tests on the histograms; and create text based 2D histogram in place of a table[69].

4.3.5 LHCbPR2FE

This project is the front end of LHCbPR2 and is written in AngularJS (with a mixture of TypeScript and JavaScript). AngularJS was chosen as a flexible framework supported by Google that can be used well into the future. LHCbPR2FE contains functionality that allows users to quickly view results of tests run in LbNightlyTools, see 4.3.1, in order to draw holistic conclusions, e.g. whether a bug has been introduced or whether a new change performs better or worse than expected. (Since bugs by their nature are unpredictable, it is better to provide a system where users can see directly the results of their test rather than rely solely on an automated alert system.)

For test authors wishing to make their tests seen in LHCbPR2, they must first create an analysis module which defines a group of test views e.g. tests involving Gauss, GEANT4, etc..

After this, test views need to be created for each discrete view to be shown in LHCbPR2FE. They are designed explicitly for users and so may or may not hide technical details as needed. This is achieved by querying the LHCbPR2BE API which contains all the associated information about the test and displaying information relevant to the user. Generally, test views initially show overview

information and can be queried (via dropdown boxes, buttons, etc.) to find further information on the selected test runs.

An excellent example of this is the test view created by the HLT team which can be seen in Figure 4.3.

For test authors who only need to compare plots in ROOT files (a common use case for LHCb simulation work), a TurboView¹ can be created. A TurboView is created using a factory function which takes a single JavaScript object which can specify a number of options and the AngularJS controller will be automatically created. An example of this factory function and its configuration object can be seen in Listing 1.

The advantages of TurboViews are: common framework for viewing the results of tests; single code base for comparing plots; upgrades to TurboView code are automatically applied to all test views; and individual test authors do not need to learn JavaScript to have their test viewed in LHCbPR2FE.

Inside a TurboView, there are several ways to compare plots from different test runs: side by side comparison, overlaid comparison, ratio plot (histograms only), ratio plot with interactive axes (histograms only) and difference plot with interactive axes (histogram only). The plot views with interactive axes are made with d3 [70], all other plots are based on jsroot [71].

The TurboView framework also implements a widget for browsing the contents of ROOT files in the test (see Figure 4.4). This allows users of LHCbPR2 to explore ROOT files associated with tests and view additional plots. This also allows the test author to create many plots which are usually not useful, but may become useful if something has gone wrong (e.g. plots used for debugging problems or plots created to test for a single bug).

¹An original contribution by the author. See text for description.

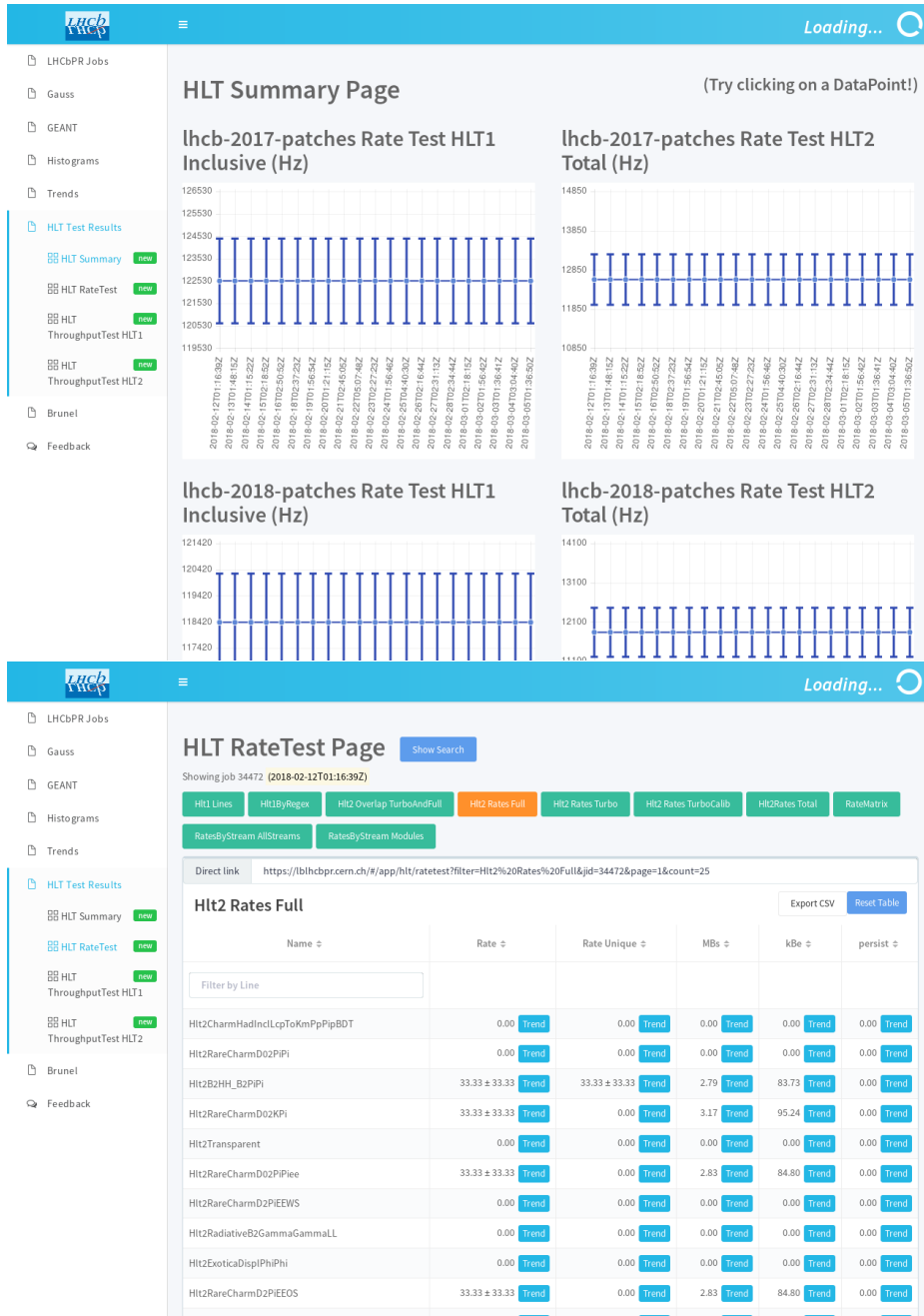


Figure 4.3: An example of the test view created by the HLT team. Clicking on a datapoint on the graphs on the top screen provides a detailed view of that run as in the bottom screenshot.

```
Module.create('gauss', 'Gauss', 2)
  .registerTurboView({
    title: "Hadronic Multiplicity & Cross Sections",
    defaultPlotView: "plotSplit",
    plotViews: ["plotSplit", "plotSame"],
    defaultPlots: [
      {
        locationInFile: "/InElastic_XSec_Kaon_10mm_Al",
        resourceName: "TargetTestCompPlots.root"
      },
      {
        locationInFile: "/Multiplicity_Proton_10mm_Be",
        resourceName: "TargetTestCompPlots.root"
      },
      {
        locationInFile: "/Elastic_XSec_Pion_10mm_Si",
        resourceName: "TargetTestCompPlots.root"
      }
    ]
  },
  restrict: {
    selectedApp: "GAUSS",
    selectedOptions: "GAUSS-TARGETHCM"
  }
});
```

Listing 1: An example of registering a TurboView.

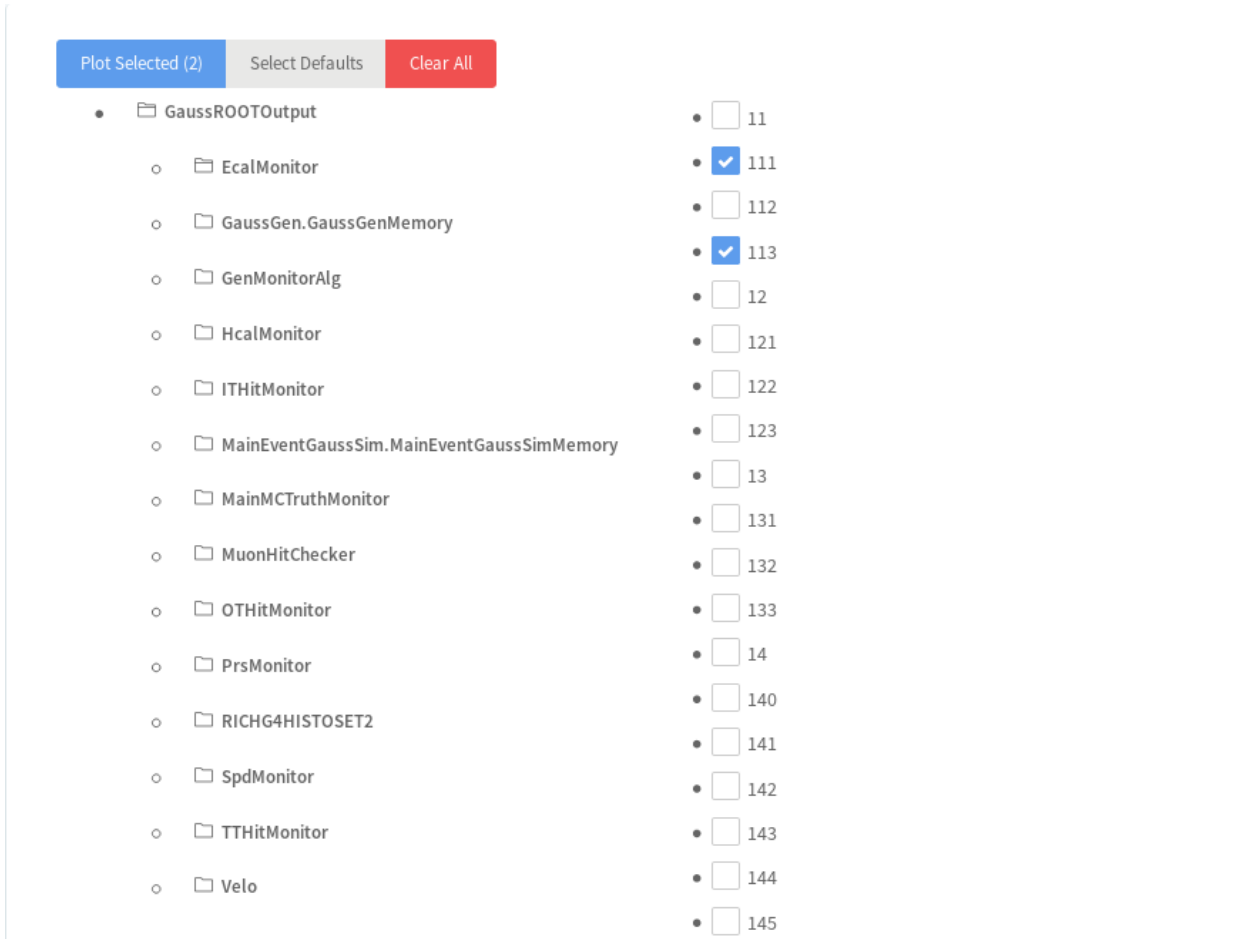


Figure 4.4: A screenshot of LHCbPR2FE's ROOT file browser's widget.

In addition to specific TurboViews, there is a *ROOT file viewer* which allows users to query any test which saves ROOT files. This means that if there is a test which is still in development or a test view does not usually display pertinent data e.g. specific debug data, this can be explored in the ROOT file viewer.

4.3.5.1 Motivation for rewriting front end

At the beginning of 2018, many of the projects on which LHCbPR2FE relied were either approaching end-of-life or were already end-of-life[72] and/or had no promise of maintenance[73, 74]. This involved several components: a paid for template, AngularJS 1.3, Bower and Node.js 5.x[75]. The following section discusses the problems caused by these projects/versions and how this contributed to the decision to rewrite the LHCbPR2FE app.

At the start of the LHCbPR2FE project in 2015, a paid for template was used as the base for the app which saved a great deal lead time in building the front end to having it usable by physicists. However, as the needs of the project evolved, the template added more problems than it solved. It was originally designed using AngularJS 1.3 and had no support for upgrading to future versions of AngularJS. This became a problem in 2018 because version 1.3 had been end-of-life for some time and the AngularJS ecosystem had stagnated, meaning that many of the packages which were used to extend the functionality of AngularJS for the app had also reached an informal end-of-life, i.e. they had been abandoned. In addition to this, it was not possible to open source LHCbPR2FE because of the licensing of the template. These issues (and other issues detailed in this section) motivated the decision to rewrite the app without the template, using the updated Angular 2+.

Two package managers were in use at the start of 2018: Bower and npm. In addition to being confusing for developers ,e.g. difficulty knowing which package manager to use for which packages,

it also introduced the possibility for package clashes (two versions of the same package installed). Bower is an open source package manager that is maintained by volunteers, but by this point almost all the developers had moved to Yarn (Bower's explicit replacement), with Bower being maintained on a best effort basis [72]. In addition to this, when Bower was used, a warning is printed on the terminal that Bower 'could break at any time'. This prompted a move to use only npm.

Node.js is the de facto standard runtime for running JavaScript applications outside of the browser. This, combined with the fact that AngularJS officially supported it, made it the natural choice for this project. The version used (Node.js 5.x) had been end of life for some time in 2018, so a move to Node.js 8.x LTS was planned.

Gulp was used as a workflow tool to build, minify, and otherwise modify² the source code for serving the app. Largely considered feature complete by the developers, code commits had stagnated and developers had moved on to new projects. With no active developers contributing to Gulp, any problems that arised would have to be fixed by LHCb developers. In addition, the Angular 2+ team recommended Webpack over Gulp, so it was decided that with future projects i.e. LHCbPR2FE2 that Webpack would be used.

Additional problems with LHCbPR2FE included: ad-hoc code architecture and lack of automated tests. There were three main code architectures in play in LHCbPR2FE making development difficult as developers could not know which architecture to target and developers reviewing merge requests found it difficult to assess whether code changes would introduce breakages. The lack of automated testing (apart from being embarrassing for a testing framework) meant that it became even more difficult to assess breakages. Often, pull requests would be accepted into the code only to find weeks later that some feature had been broken.

²Processes such as compiling from TypeScript to JavaScript, lazy loading, etc.

As it was, active development of LHCbPR2FE was stopped and work started on LHCbPR2FE2.

4.3.6 LHCbPR2FE2

Currently in development, LHCbPR2FE2 is a complete rewrite of LHCbPR2FE (see subsection 4.3.5). The previous iteration had several problems:

- ad-hoc architecture used throughout the code
- mix of TypeScript and JavaScript code
- large amount of dependencies
- untested codebase.

However, there are several features which LHCbPR2FE did well:

- inclusion of TurboViews allowing quick test views to be made for simple applications
- easy access to job information.

It was desirable to keep these features while eliminating code bloat and many of the previous dependencies.

LHCbPR2FE2 is built in Angular 6 using VMWare's Clarity Design System (CDS). The use of CDS allows developers to focus on code by using established user experience (UX) guidelines, provided by CDS, instead of having to design the look of the front end from scratch. The CDS also provides Angular bindings by design which makes it the natural choice for this project.

Angular also uses webpack, a module bundler that is much simpler than the previous set up with gulp. Using webpack, developers only need to specify an *entry point* (i.e. a central file from

which all files are eventually imported; similar to `int main()` for C++) and webpack determines which files to be included and bundles them to be served as a single file in the browser. With the previous system, it was required for developers to manually code this process by including files by hand and defining many additional processes, such as lazy loading, minifying code, etc., which are now done automatically by webpack.

Chapter 5

Analysis

The $B_c^+ \rightarrow \bar{K}^{*0}(892)(\rightarrow K^- \pi^+)K^+$ decay has not been observed to date. It is a flavour changing process involving $c \rightarrow s$ and $b \rightarrow s$ transitions (Figure 5.1). The B_c is a particularly interesting meson as it is composed of the two heaviest quarks that form bound states, given the t quark decays before it hadronises. At a mass of $(6.276 \pm 0.004) \text{ GeV}/c^2$ [12], there are very few backgrounds for this decay which, at tree level, has an amplitude proportional to the CKM elements $V_{cb}^* V_{us}$.

This chapter describes a blind analysis in which a control channel is used to validate performance of the selection and modelling of the channel. The selection is developed on simulated data of the control channel, as described in section 5.2, and then validated against the well established data and measurements of the control channel. Efficiencies are calculated for both the control and signal channels using simulated data; any deficiencies in modelling of the control channel are then propagated to efficiency estimates made using the signal channel simulated data. Throughout the procedure, no signal data in a defined signal region, i.e. a mass window around the expected signal peak, are examined until all aspects of the analysis have been studied thoroughly to reduce bias (a

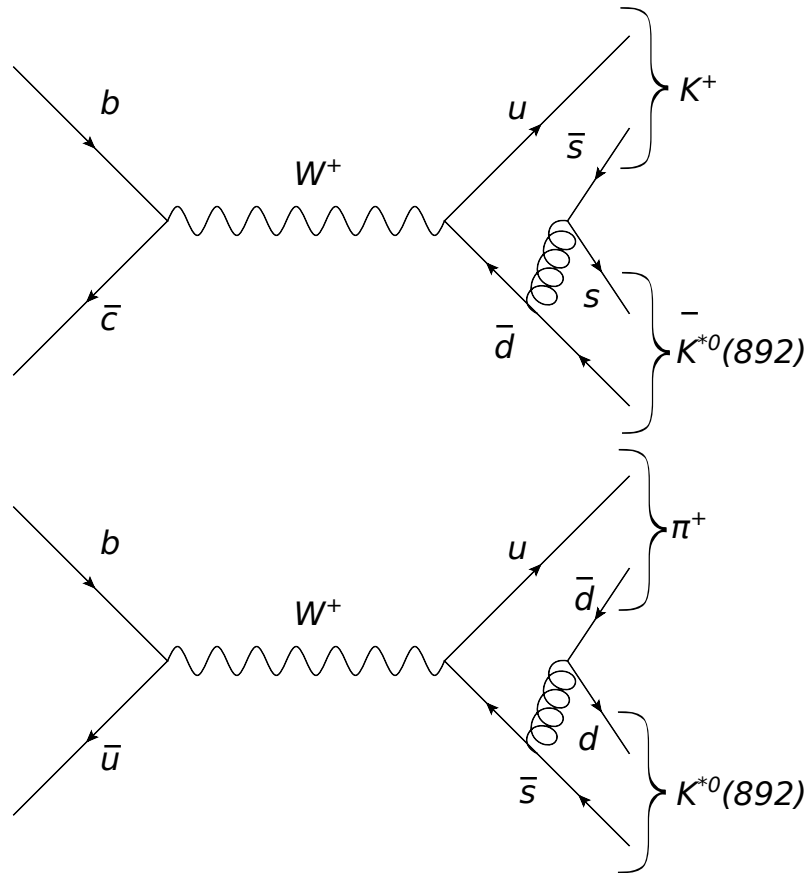


Figure 5.1: Feynman diagrams representing the two most common decay modes for the control channel and signal channel.

process known as ‘blinding’). Modelling of the background data in the signal region is, prior to unblinding, carried out by performing fits to the mass sidebands and extrapolating underneath the signal peak.

The key parts of the analysis are:

section 5.2 Develop selection of the data to maximise chosen figure of merit (so-called Punzi figure of merit (Punzi FoM)). This is performed using a mixture of hard cuts and a BDT.

section 5.3 Perform fits on data using signal and background parameterisations, established prior to unblinding, to extract signal yield.

section 5.4 Evaluation of efficiencies associated with the signal and control channel.

section 5.5 Calculation of systematic errors arising from choices made in the analysis or unknown factors beyond the control of the analysis such as theoretical uncertainties and LHCb’s B_c fragmentation fraction.

The control channel for this analysis is $B^+ \rightarrow K^{*0}(892)(\rightarrow K^+ \pi^-) \pi^+$. This channel was chosen because of its similarity to the $B_c^+ \rightarrow \bar{K}^{*0}(892)(\rightarrow K^- \pi^+) K^+$. Ideally, the control channel would have the same decay products and topology. In this case the $B^+ \rightarrow K_0^*(892) K$ has too small a branching fraction to be used effectively. Therefore, the $B^+ \rightarrow K^{*0}(892)(\rightarrow K^+ \pi^-) \pi^+$ was chosen because it has the same topology and very similar decay products i.e. swapping a K for a π .

5.1 Simulation

Simulation is widely used to understand the performance of given selections. It is of paramount importance that simulation provides a good description of the data. For this exclusive reconstruction, PID is particularly important given the control and signal channel final states differ only in the identification of the ‘bachelor’ K/π .

5.1.1 Recalculating ProbNN variables

Detailed comparisons showed that simulation of ProbNN variables (section 2.8) were poorly estimated by the simulation for a variety of reasons, including: miscalibration of the detector; imperfect

knowledge of physics interactions e.g. how stable particles interact with materials present in the detector; and ProbNN's hidden layers being unknown and therefore it being difficult to model the interplay between the variables (a common problem with neural nets). Therefore the ProbNN variables were recalculated using a package called PIDCorr [76] that applies a kernel density estimation for ProbNN based on p_T , η and the number of tracks in a given event (N_{tr}). This improved the agreement of simulated data with data making it more suitable for use with the BDT.

5.1.1.1 PIDCorr

Improvement in the agreement of simulated data with data for ProbNN variables involves taking p_T , η , N_{tr} and the ProbNN variables from simulated data, formulating a Probability Density Function (PDF) based on a 4D Kernel Density Estimation (KDE) from a separate, well known sample where the particle type is clear, the data are accurately understood (i.e. fits to data have a high precision), and there is good coverage between the p_T , η and N_{tr} variables.

The reweighting process can be broken down into the following steps [76]:

1. Obtain a sufficiently well known dataset, i.e. one that contains a well known decay channel with good signal efficiency and low background, is fit and sWeighted¹[77] to provide the calibration sample.
2. Transform the input variables of the calibration sample into relatively uniform distributions allowing for more accurate KDE. E.g. $\text{ProbNN}'_x = 1 - (1 - \text{ProbNN}_x)^\gamma$ (where γ is between

¹sWeighting, as described in [77], is a process by which real data is taken and has weights applied to it that match the probability that a given event is signal or background depending on input PDFs. This means that for a given mass, m , the probability an event in that bin is a signal event is $S(m)/(S(m) + B(m))$ where $S(m)$ and $B(m)$ are the signal and background PDFs respectively.

0.15 and 0.5 for different ProbNN), $p_T = \ln p_T$ and $N'_{tr} = \ln N_{tr}$. (η is sufficiently uniform without a transformation.)

3. 1D KDE are calculated for each transformed variable.
4. The two most correlated variables, different for each case of ProbNN, have their 1D PDFs multiplied together with a fixed kernel width creating an approximate PDF. The individual variable PDFs are then multiplied again but with variable kernel widths where the kernel is defined as proportional to the square of the PDF density at that point on the approximate PDF.
5. The other two remaining variables are multiplied similarly, with the PDF of the last step being multiplied by a 1D variable PDF.

As a demonstration, the results of this process on ProbNNp can be seen in Figure 5.2.

5.2 Selection

In order to maximise the performance of the signal selection, criteria that distinguish the signal channel signal and background are devised and applied to data.

5.2.1 Preselection

To make best use of the BDT, a preselection is applied. These cuts are used to remove poor quality events or events that have an *a priori* reason not to be signal events e.g. the case that events lie far outside the phase space of $B^+ \rightarrow K^{*0}(892)(\rightarrow K^+\pi^-)\pi^+$ or $B_c^+ \rightarrow \bar{K}^{*0}(892)(\rightarrow K^-\pi^+)K^+$.

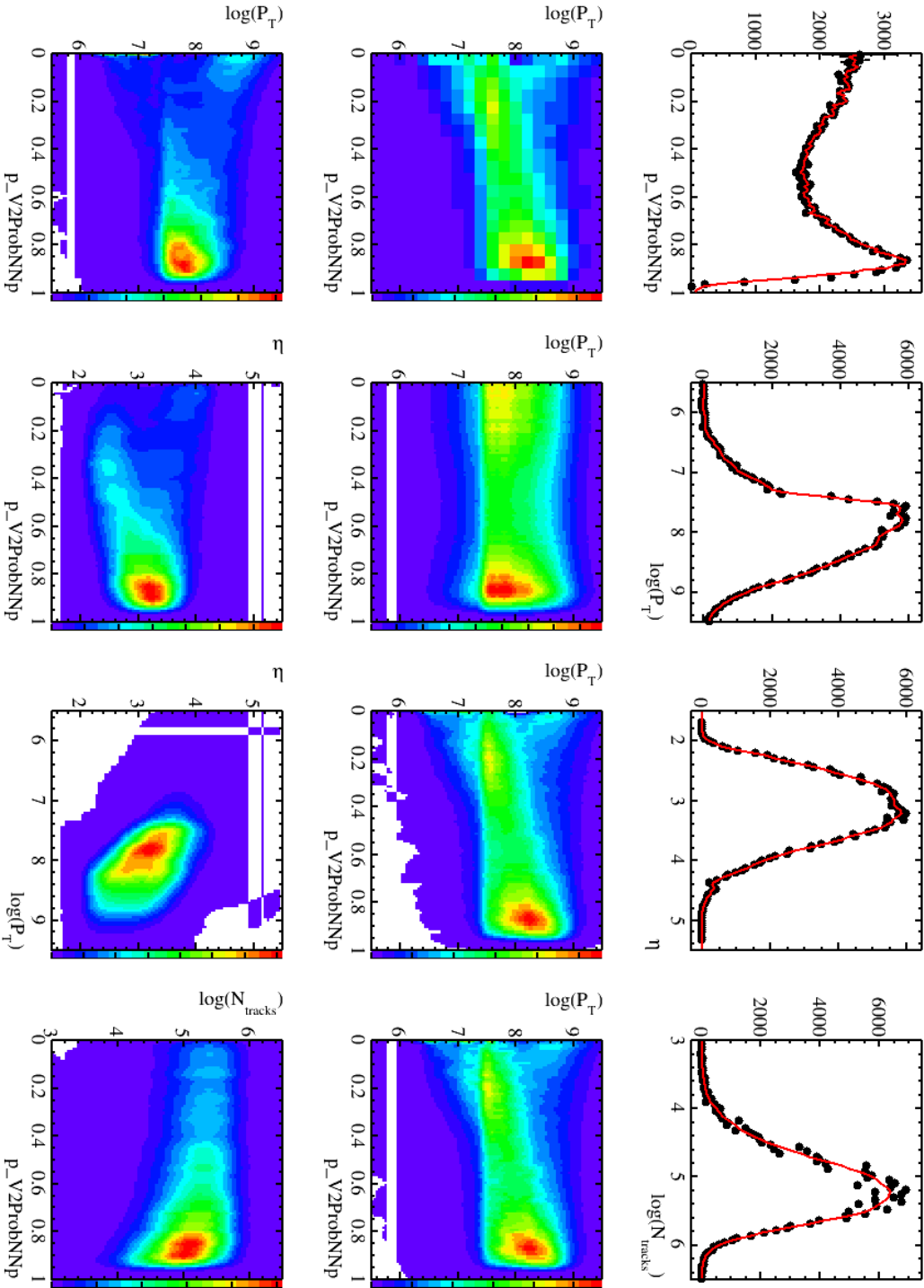


Figure 5.2: Results of the calculation of the KDE for ProbNNp [78].

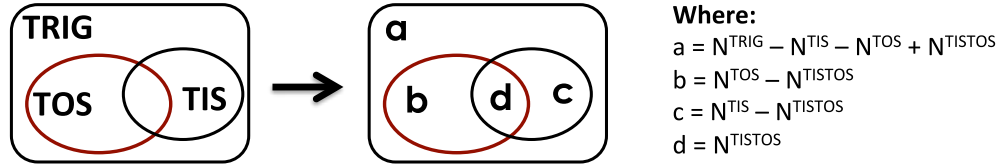


Figure 5.3: Schematic diagram of the TISTOS method [79].

This allows the BDT to boost sensitivity based on more subtle features of the data rather than highlighting obvious differences between background and signal e.g. $K^{*0}(892)$ mass.

Preselection comes in three stages: trigger, stripping and loose invariant mass criteria around the $K^{*0}(892)$ resonance.

5.2.1.1 Trigger cuts

The trigger cuts used in this analysis are listed in Table 5.1. It is required that a given event pass at least one trigger i.e. a logical OR in every level and a logical AND between levels 5.3. Trigger lines ending in $_TOS^2$ indicate that the event itself has triggered the line whereas $_TIS^3$ indicates that the line was triggered by something independent of the candidate.

It is possible to measure the efficiency of the triggers using a data driven method, the so-called TISTOS method [79]. Since the simulated data in general do not provide a fully accurate model of at least one of the triggers in the analysis, this data driven method is used to estimate efficiencies and systematic errors. For the TISTOS method, the efficiency of a given trigger line is defined as:

$$\epsilon_{\text{Trig}} = \frac{N_{\text{Trig|Sel}}}{\sum_i N_{\text{Sel}}^i} = \frac{N_{\text{Trig|Sel}}}{\sum_i \frac{N_{\text{TIS|Sel}}^i}{\epsilon_{\text{TIS}}^i}} = \frac{N_{\text{Trig|Sel}}}{\sum_i \frac{N_{\text{TIS|Sel}}^i N_{\text{TOS|Sel}}^i}{N_{\text{TISTOS|Sel}}^i}} \quad (5.1)$$

²Trigger On Signal

³Trigger Independent of Signal

Table 5.1: Trigger cuts. All events must pass at least one trigger on each level to be included.

Trigger level	Lines
L0	LOGlobal_TIS LOHadronDecision_TOS
HLT1	Hlt1TrackAllL0Decision_TOS
HLT2	Hlt2Topo2BodyBDTDecision_TOS Hlt2Topo3BodyBDTDecision_TOS

where Trig|Sel is the given trigger line given a fixed selection and N is the number of events and ϵ is the efficiency. All sums are over phase space bins, if applied.

The LOGlobal_TIS trigger catches any events which have been triggered by any TIS trigger. The LOHadronDecision_TOS trigger selects the highest E_T hadron (as identified by the PS and SPD subdetectors). The Hlt1TrackAllL0Decision_TOS trigger verifies all L0 decisions based on the improved (partial) reconstruction available at HLT1. The Hlt2Topo2BodyBDTDecision_TOS and Hlt2Topo3BodyBDTDecision_TOS triggers take advantage of full reconstruction available at HLT2 and apply a BDT to identify 2-body and 3-body decays.

5.2.1.2 Stripping

The following requirements are taken from [29] which uses the same stripping selection. These account for the shorter lifetime of the B_c^+ meson and no muons. To allow for the measurement of the control channel, a mass window around the B^+ has been opened.

Reconstructed candidates for both signal and control channel decays must satisfy the following criteria which are based on reconstructed tracks:

- at least one track has a p_T greater than 1.5 GeV/c,

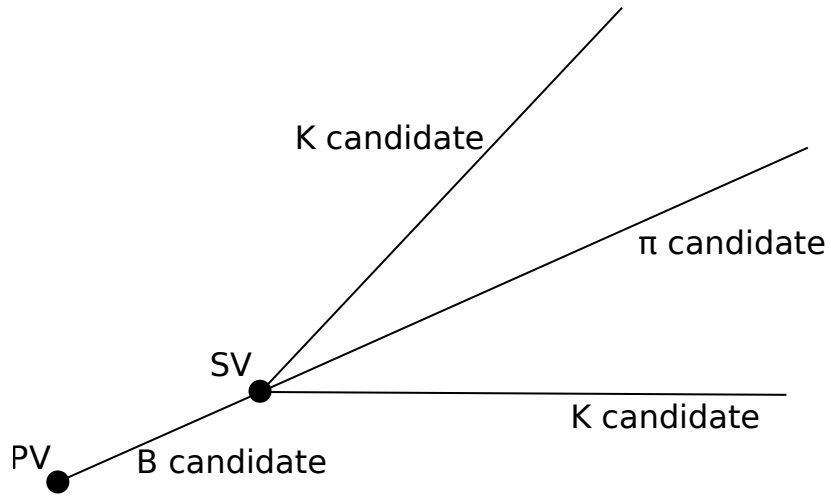


Figure 5.4: Schematic view of the decay as seen in the lab frame. PV refers to the primary vertex where the B candidate is first detected. SV refers to the secondary vertex where the B candidate decays. Since the $K^{*0}(892)$ decays immediately, there are only two vertices visible in the detector.

- sum of the p_T of all tracks greater than 4.5 GeV/c,
- sum of the momenta of all tracks greater than 22 GeV/c,
- distance from secondary vertex (SV) (Figure 5.4) to PV greater than 1.5 mm,
- SV χ^2/NDF of less than 20,
- the angle between the B candidate's momentum vector and the vector between primary and secondary vertices has $\cos(\theta)$ greater than 0.9999,
- fewer than 200 tracks with hits in the VELO.

The tracks from which candidates are formed are required to have (as is standard in LHCb):

- p_T of greater than 0.25 GeV/c,
- momentum of greater than 2.5 GeV/c,
- χ^2/NDF of greater than 1 for the IP,
- χ^2/NDF less than 3 for each track fit,
- distance of closest approach no more than 0.2 mm from SV,
- a ProbNN_K of greater than 0.2 on K tracks,
- a ProbNN_π of greater than 0.15 on π tracks,
- a $\text{ProbNN}_{\text{ghost}}$ of greater than 0.5, where ghost tracks are tracks for which points have randomly aligned to create a track which does not represent a true particle track. $\text{ProbNN}_{\text{ghost}}$ provides ProbNN-like detection of these tracks

The reconstructed B_c^+ or B^+ meson candidate must in addition satisfy:

- mass between 5.10 GeV/c² to 5.50 GeV/c² or 6.05 GeV/c² to 6.50 GeV/c²,
- χ^2/NDF for the IP less than 10,
- p_T of greater than 1 GeV/c.

5.2.1.3 Resonant mass cuts

After stripping, a further cut to the $K^{*0}(892)$ was applied requiring the mass to be from 800 MeV to 1200 MeV.

5.2.2 BDT

The final selection uses a BDT from the sklearn python package [80]. The list of variables used as inputs to the BDT can be found in Table 5.2 and plots showing the distribution of signal and background input variables can be found in Figures 5.5 to 5.8.

The BDT is composed of two parts: decision trees and a booster. The decision trees use the Gini impurity [81] method for ensuring the split between signal and background is sufficient in chosen subsamples. The maximum depth [82] of the trees is two. The maximum number of variables in each tree is eight. The minimum samples per leaf is 9.9% of the total amount of data. The booster is an AdaBoostClassifier using the algorithm SAMME [83]. It is configured to have a learning rate of 0.5 and 250 decision trees and a random seed of 9001.

BDTs are a common machine learning algorithm which takes a series of weak learners (decision trees) and *boosts* (weights) them according to their ability to distinguish signal candidates from background. An traditional decision tree consists of multiple factors deciding a single outcome,

Table 5.2: List of variables used in BDT.

Variable name	Variable description
Bc_ConsKstar_chi2__0	Fitted $K^{*0}(892)$ mass χ^2
Bc_IPCHI2_OWNPV	B candidate impact parameter χ^2
d1_ProbNNk	ProbNNk of the first daughter
d1_ProbNNpi	ProbNNpi of the first daughter
d1_TRACK_Likelihood	Likelihood of the fitted track for the first daughter
d2_ProbNNk	ProbNN $_K$ of the second daughter
d2_ProbNNpi	ProbNN $_{\pi}$ of the second daughter
d2_TRACK_Likelihood	Likelihood of the fitted track for the second daughter

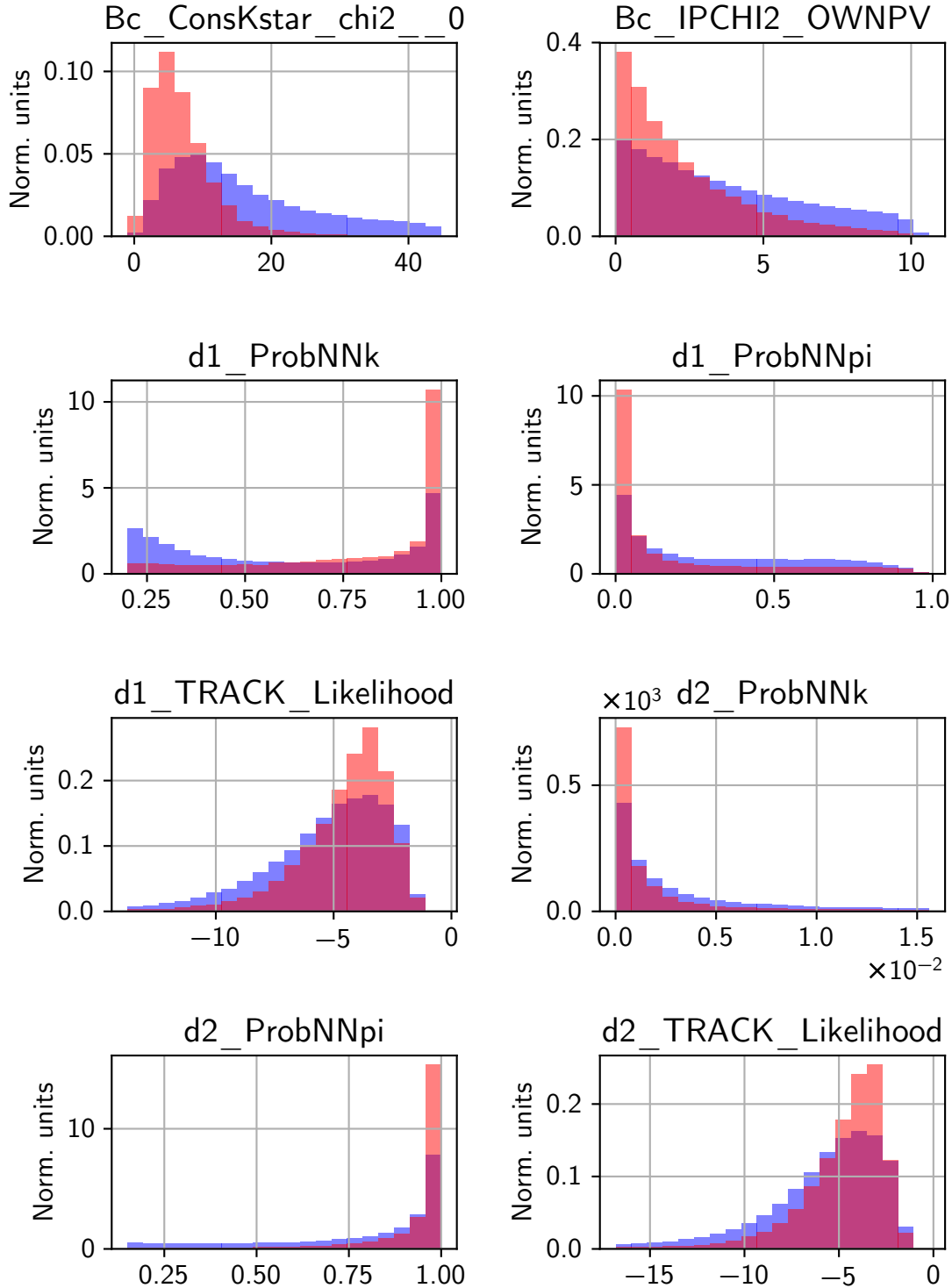


Figure 5.5: Input variable distributions for the BDT for $B^+ \rightarrow K^{*0}(892) (\rightarrow K^+ \pi^-) \pi^+$ 2011. Red is simulated data (signal) and blue is data sidebands (background). x -axes are dimensionless. y -axes are normalised counts (such that the area under each individual histogram is 1).

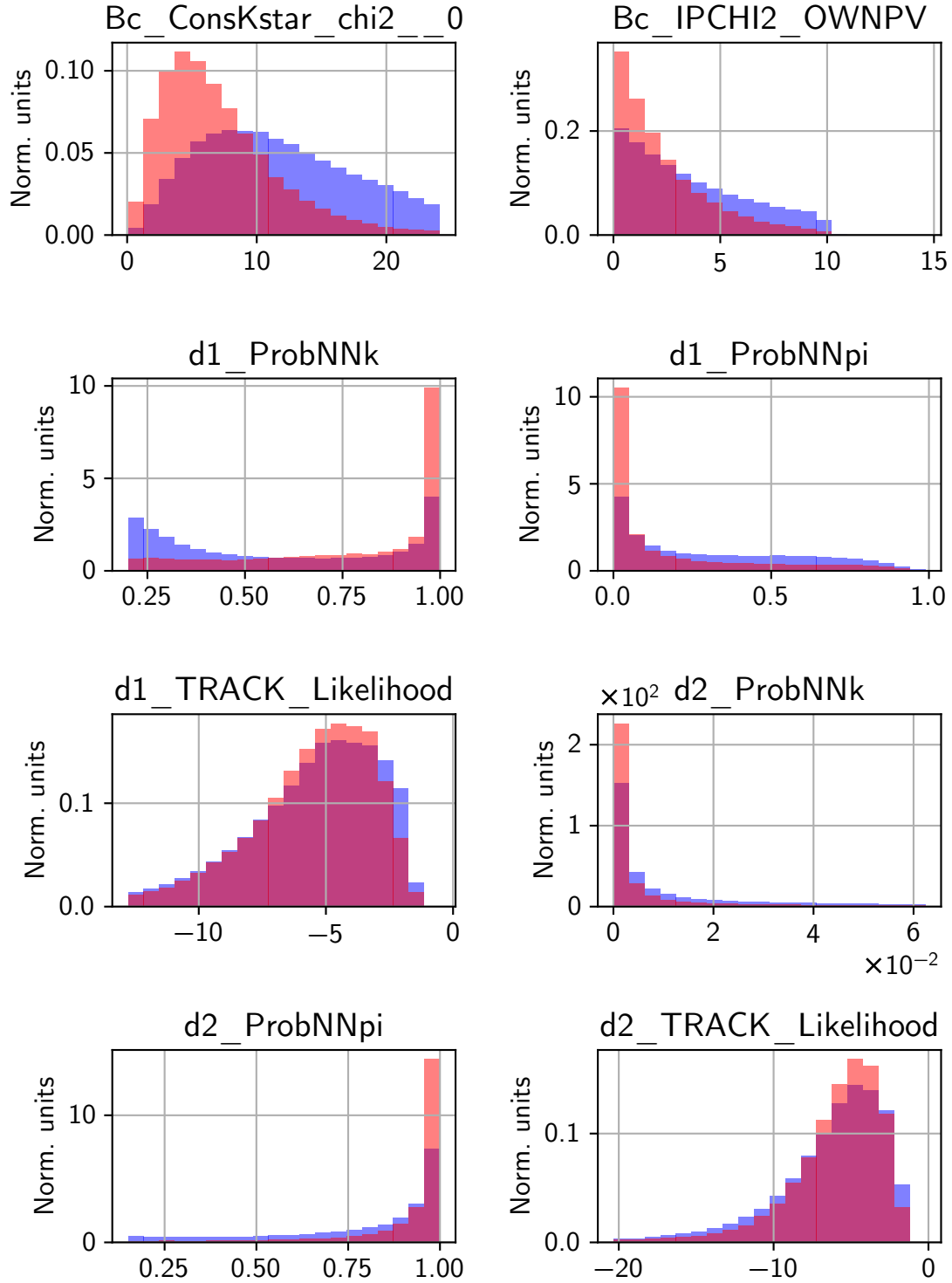


Figure 5.6: Input variable distributions for the BDT for $B^+ \rightarrow K^{*0}(892) (\rightarrow K^+ \pi^-) \pi^+$ 2012. Red is simulated data (signal) and blue is data sidebands (background). x -axes are dimensionless. y -axes are normalised counts (such that the area under each individual histogram is 1).

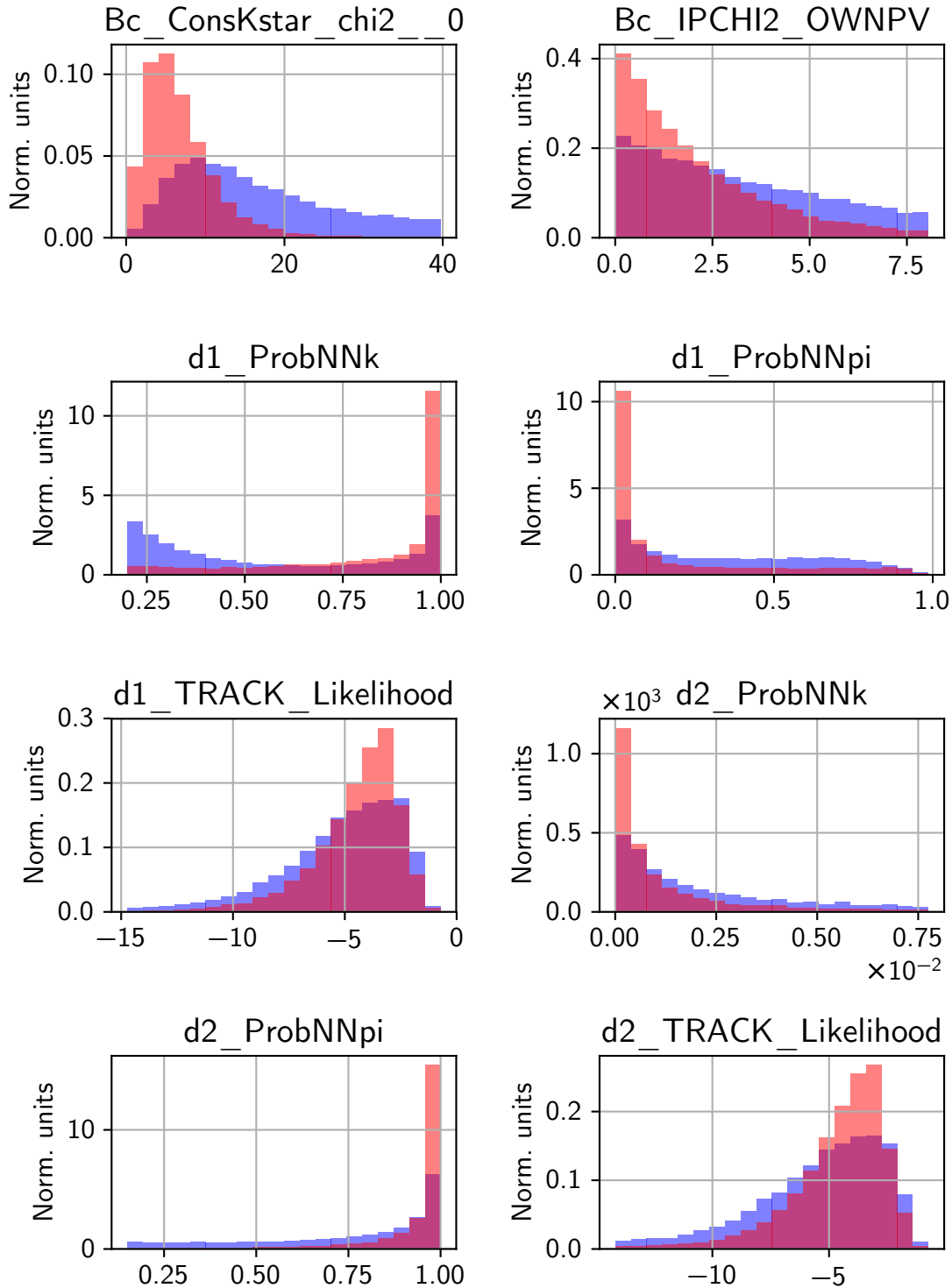


Figure 5.7: Input variable distributions for the BDT for $B_c^+ \rightarrow \bar{K}^{*0}(892) (\rightarrow K^- \pi^+) K^+$ 2011. Red is simulated data (signal) and blue is data sidebands (background). x -axes are dimensionless. y -axes are normalised counts (such that the area under each individual histogram is 1).

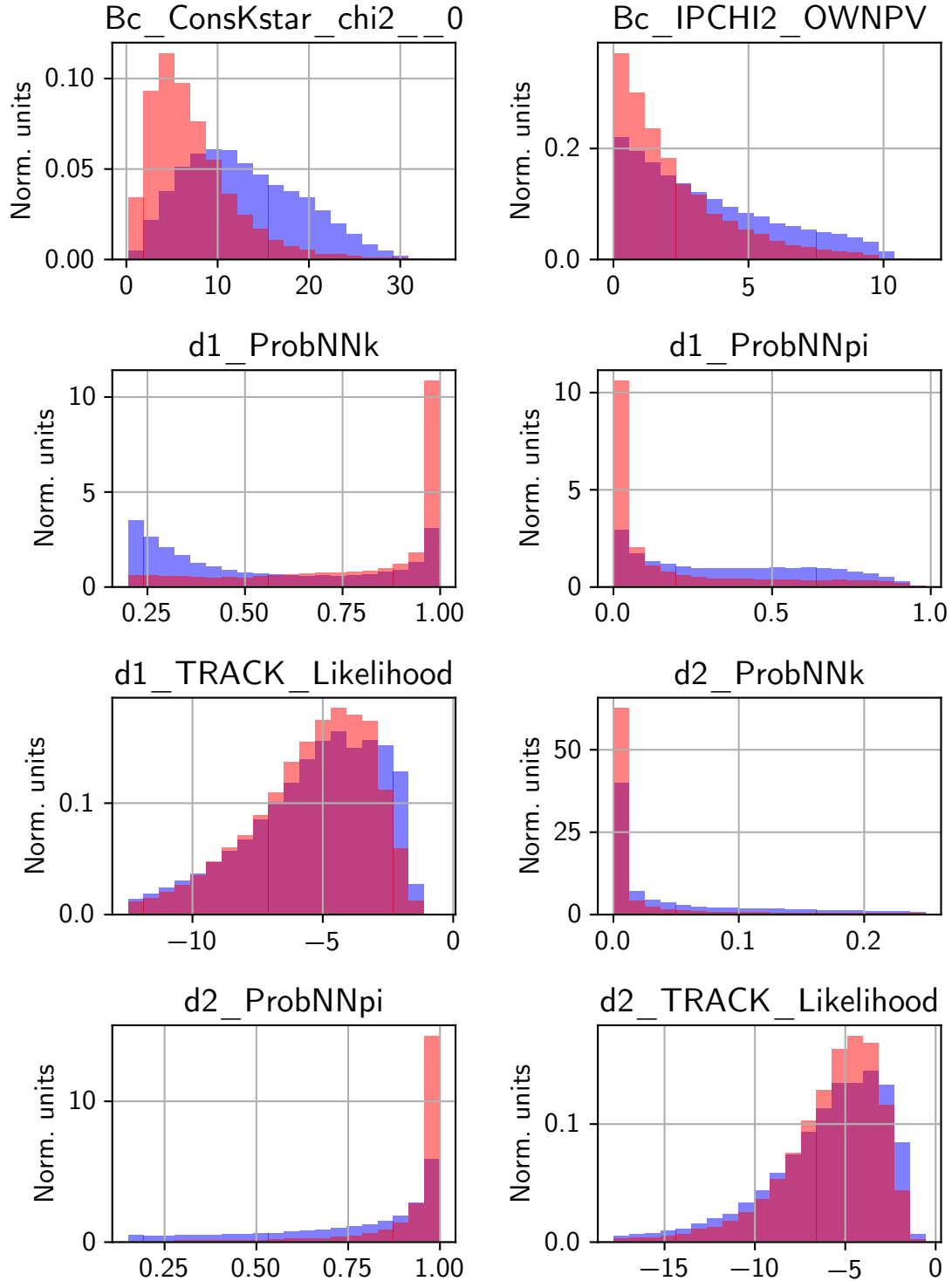


Figure 5.8: Input variable distributions for the BDT for $B_c^+ \rightarrow \bar{K}^{*0}(892) (\rightarrow K^- \pi^+) K^+$ 2012. Red is simulated data (signal) and blue is data sidebands (background). x -axes are dimensionless. y -axes are normalised counts (such that the area under each individual histogram is 1).

where each factor comes with a probability if it is true or false. In a BDT, many shallow trees, or ‘stubs’ are created that are only one or two factors (or ‘leaves’) deep. In the case of continuous data, the factors are individual selection criteria e.g. $p_T < 30$ MeV. The boosting algorithm then weights each of the stubs in terms of predictive power, so that the most predictive stubs are given the strongest weight.

When so-called ‘BDT weights’ are applied to an event, it outputs a number between $(-1, 1)$ which maps to the probability that an event is 100% likely to be background (-1) or 100% likely to be signal (1) or equally likely to be both (0) .

5.2.2.1 Results

BDTs weights are tested for overtraining⁴ by applying the weights to the training sample and a testing sample not used in the BDT training. If the BDT response of the test data agree with the training data, then the BDT has been appropriately trained and can be used on the remaining data. The overtraining plots for the control and signal channels can be seen in figs. 5.9(a), 5.9(b), 5.10(a) and 5.10(b).

This analysis uses a k-folding [84] technique where the data are trained and tested on mutually exclusive subsamples of the dataset such that all the data have a valid BDT applied to them. This means that for a dataset split into two equal parts, A and B , one can train a BDT on A and test/apply it to B while training a separate BDT on B and testing/applying it to A . The data are then combined with a BDT event for each event.

⁴If overtrained, the BDT will overestimate its effectiveness. Overtraining is when the BDT becomes too specific about describing the subset of the data that has been used for training rather than the properties of the parent distribution.

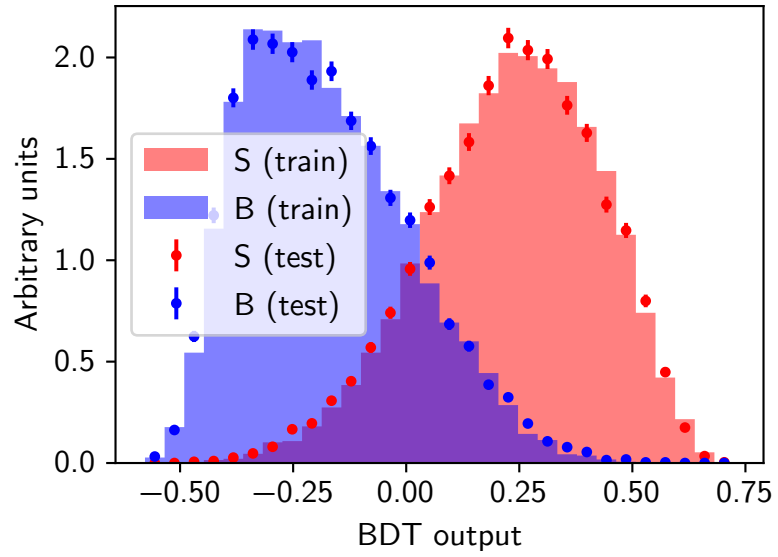
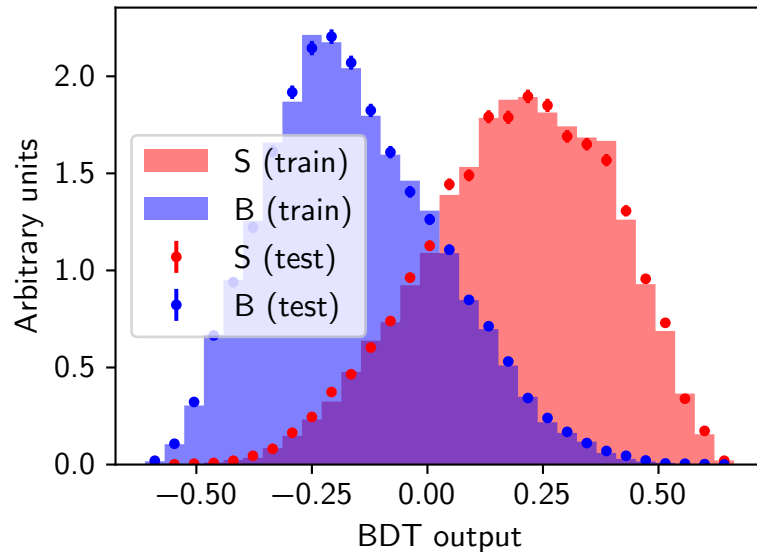
(a) Overtraining check for $B^+ \rightarrow K^{*0}(892)(\rightarrow K^+ \pi^-) \pi^+$ 2011 data(b) Overtraining check for $B^+ \rightarrow K^{*0}(892)(\rightarrow K^+ \pi^-) \pi^+$ 2012 data

Figure 5.9: Overtraining plots for $B^+ \rightarrow K^{*0}(892)(\rightarrow K^+ \pi^-) \pi^+$. Filled histograms represent data used to train the BDT. Dot with errors represent testing data. If the histograms are not compatible, this is a sign that the BDT is overtrained.

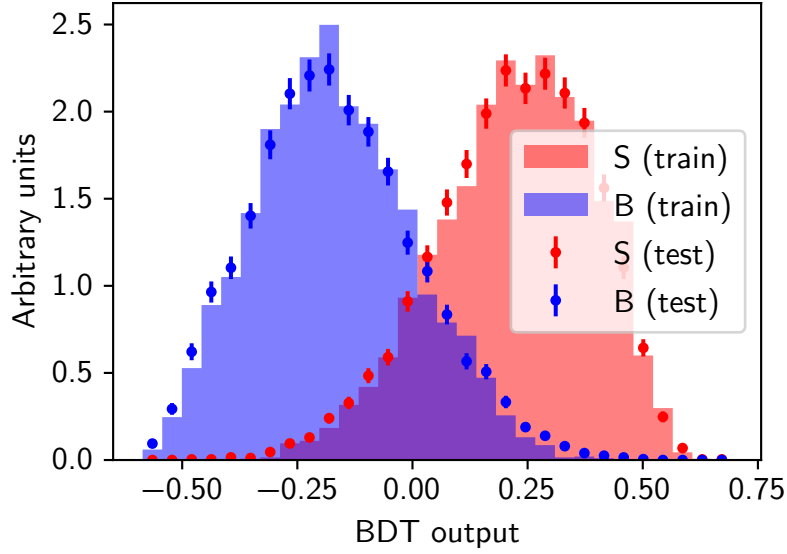
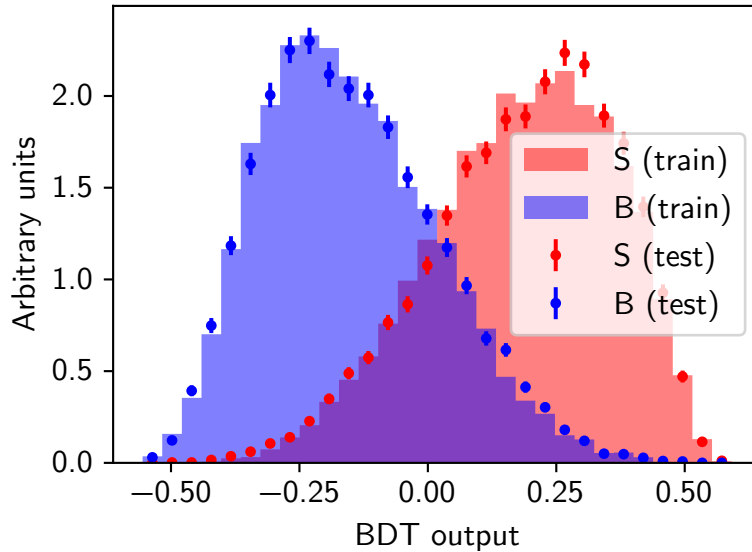
(a) Overtraining check for $B_c^+ \rightarrow \bar{K}^{*0}(892)(\rightarrow K^- \pi^+)K^+$ 2011 data(b) Overtraining check for $B_c^+ \rightarrow \bar{K}^{*0}(892)(\rightarrow K^- \pi^+)K^+$ 2012 data

Figure 5.10: Overtraining plots for $B_c^+ \rightarrow \bar{K}^{*0}(892)(\rightarrow K^- \pi^+)K^+$. Filled histograms represent data used to train the BDT. Dot with errors represent testing data. If the histograms are not compatible, this is a sign that the BDT is overtrained.

5.2.2.2 Punzi figure of merit

Choosing the most significant BDT cut is best done by defining a statistically supported figure of merit. The Punzi FoM [85] was chosen for this analysis since it is appropriate for analyses where the final cross section is not known. Other figures of merit were considered $(S/\sqrt{B}, S/(\sqrt{S+B}))$, but these all required *a priori* knowledge of the cross section.

The Punzi FoM for various BDT cuts can be found in figs. 5.11 and 5.12. It is defined as:

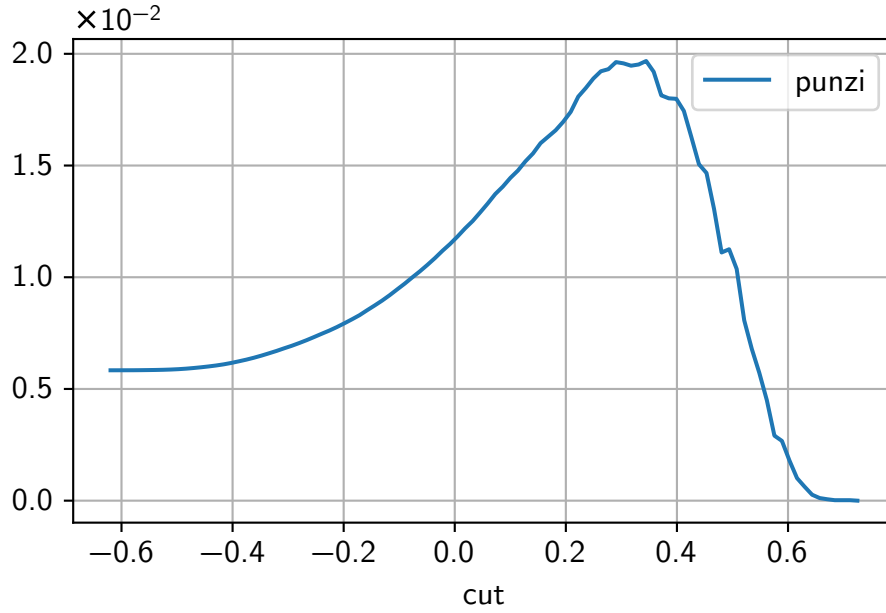
$$\frac{\varepsilon(t)}{a/2 + \sqrt{B(t)}}, \quad (5.2)$$

where t is independent variable under examination e.g. mass of the B candidate, ε is the efficiency of the signal for given cuts, a is the target significance in standard deviations and B is the number of background events in the signal region. For this analysis, $a = 5$.

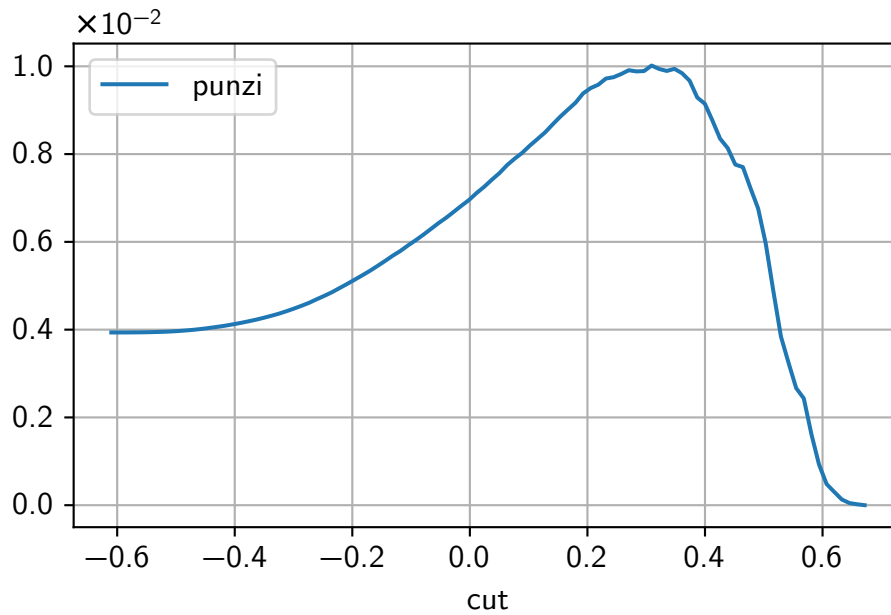
The cuts for this analysis are chosen to be as $\text{bdt} > 0.10$ for the $B^+ \rightarrow K^{*0}(892)(\rightarrow K^+\pi^-)\pi^+$ case and $\text{bdt} > 0.10$ for the $B_c^+ \rightarrow \bar{K}^{*0}(892)(\rightarrow K^-\pi^+)K^+$ case, where bdt is the BDT response for each event. These values were chosen to be left of the peak found in the figs. 5.11 and 5.12 in order to pick a value that is relatively insensitive to small changes in the BDT value required. If the Punzi FoM is not perfectly modelled by simulated data, it is possible that the peak of the distribution could move, meaning that the cut may fall down the ‘wrong’ side of the maximum.

5.3 Yield extraction

The purpose of this analysis is to measure the yield of the decay $B_c^+ \rightarrow \bar{K}^{*0}(892)(\rightarrow K^-\pi^+)K^+$. The control channel is used to validate the method and quantify the level of agreement between sim-



(a) Punzi figure of merit for BDT $B^+ \rightarrow K^{*0}(892)(\rightarrow K^+\pi^-)\pi^+$ 2011.



(b) Punzi figure of merit for BDT $B^+ \rightarrow K^{*0}(892)(\rightarrow K^+\pi^-)\pi^+$ 2012.

Figure 5.11: Punzi figure of merit for various BDT cuts for control channel case. The x -axis is defined as $\text{bdt response} > x$, with the y -axis defined as the (dimensionless) figure of merit.

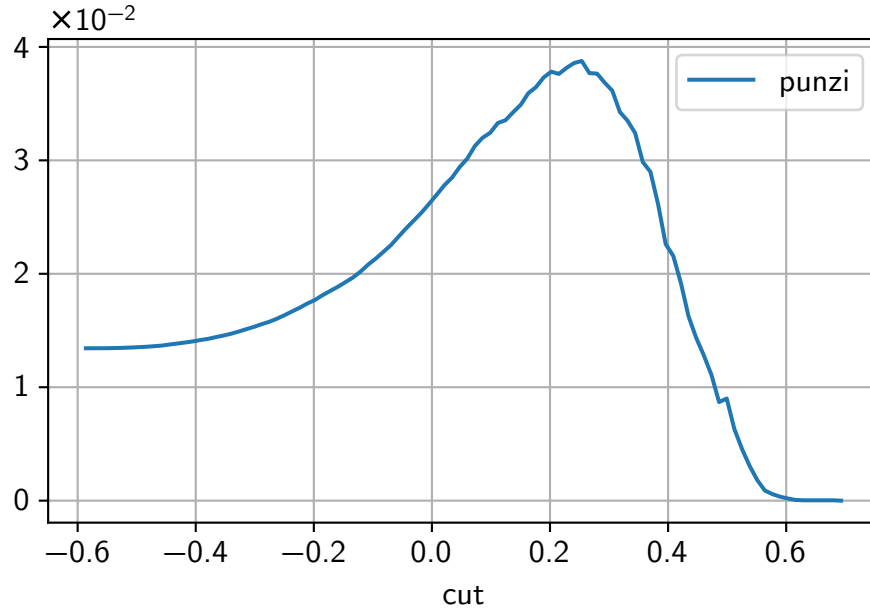
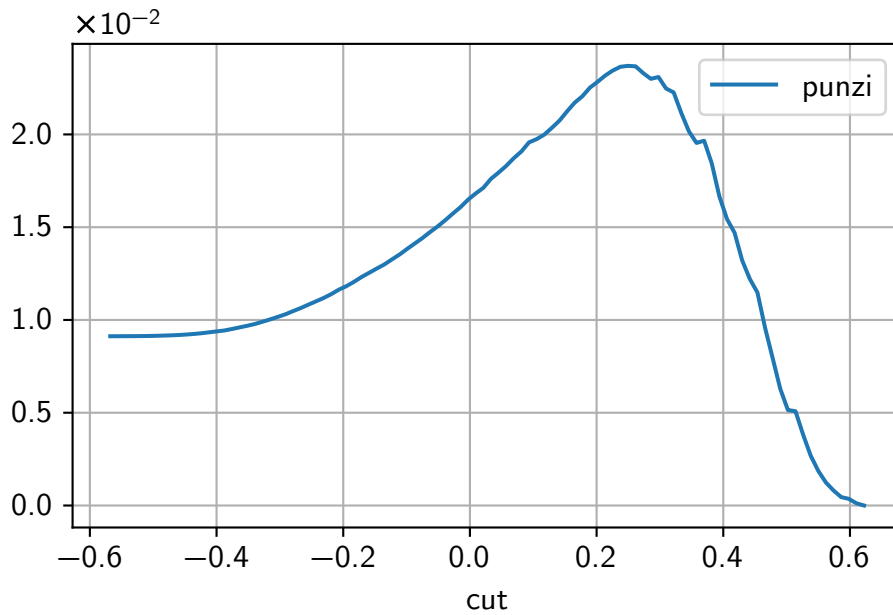
(a) Punzi figure of merit for BDT $B_c^+ \rightarrow \bar{K}^{*0}(892)(\rightarrow K^- \pi^+)K^+$ 2011.(b) Punzi figure of merit for BDT $B_c^+ \rightarrow \bar{K}^{*0}(892)(\rightarrow K^- \pi^+)K^+$ 2012.

Figure 5.12: Punzi figure of merit for various BDT cuts for signal channel case. The x -axis is defined as BDT response $> x$, with the y -axis defined as the (dimensionless) figure of merit.

ulated data and data, which is then incorporated into the fit for the $B_c^+ \rightarrow \bar{K}^{*0}(892)(\rightarrow K^- \pi^+) K^+$ case.

For the $B^+ \rightarrow K^{*0}(892)(\rightarrow K^+ \pi^-) \pi^+$, the following steps are carried out:

1. fit the signal PDF to the simulated data,
2. fix key parameter values,
3. fit the control channel data with the same signal PDF (using the fixed values), allowing the yield to float,
4. extract the yield.

The mass offset and ratio of σ s between simulated data and data for the $B^+ \rightarrow K^{*0}(892)(\rightarrow K^+ \pi^-) \pi^+$ are used to Gaussian constrain the corresponding parameters in the final fit from which the yield for the $B_c^+ \rightarrow \bar{K}^{*0}(892)(\rightarrow K^- \pi^+) K^+$ is extracted.

5.3.1 Fit description

Selected signal and control channel candidates are described using an Ipatia distribution [86]. Derived from a Crystal Ball (CB) distribution[87], the Ipatia distribution has a hyperbolic core which has been parameterised to account for variance prior density, i.e. for the unknown variance of the distribution, while the radiative tails are constructed by analogy from the CB. This does not include a correction for per-event errors, but tests from [86] show that this correction is negligible over the kinematic phase space of LHCb.

The Ipatia distribution has the form:

$$I(m, \mu, \sigma, \lambda, \zeta, \beta, a, n) \propto \begin{cases} \left((m - \mu)^2 + \frac{\xi K_\lambda(\xi)}{K_{\lambda+1}(\xi)} \sigma^2 \right)^{\frac{1}{2}(\lambda - \frac{1}{2})} e^{\beta(m - \mu)} K_{\lambda - \frac{1}{2}} \left(\zeta \sqrt{1 + \left(\frac{m - \mu}{A_\lambda(\zeta)\sigma} \right)^2} \right) & , \text{ where } \frac{m - \mu}{\sigma} > -a \\ \frac{G}{\left(1 - m / \left(n \frac{G}{G'} - a \sigma \right) \right)^n} & , \text{ where } \frac{m - \mu}{\sigma} \leq -a \end{cases} \quad (5.3)$$

where m is the mean, μ is the mean offset, i.e. the central value for the fitted mass, ξ is related to the variance prior, σ is the RMS of the distribution (and also contains a term scaling it with the variance prior), β is the asymmetry parameter (set to 0 in this analysis) and $K_n(\xi)$ are cylindrical harmonics or special Bessel functions of the third kind, parameterised with ξ . For more detailed information on these parameters, see [86, 88]. G itself describes the core of a CB-like function and is defined as

$$G(m, \mu, \sigma, \lambda, \zeta, \beta) \propto \left((m - \mu)^2 + \frac{\xi K_\lambda(\xi)}{K_{\lambda+1}(\xi)} \sigma^2 \right)^{\frac{1}{2}(\lambda - \frac{1}{2})} e^{\beta(m - \mu)} K_{\lambda - \frac{1}{2}} \left(\zeta \sqrt{1 + \left(\frac{m - \mu}{A_\lambda(\zeta)\sigma} \right)^2} \right). \quad (5.4)$$

Fits to simulated data can be seen in figs. 5.13(a), 5.13(b), 5.14(a) and 5.14(b). In all four figures, good agreement can be seen between the Monte Carlo (MC) data and the fitted Ipatia.

In all cases, the simulated data/data are fit simultaneously between years to make the best use of the information content available.

For the fit to data, the following parameters are fixed: β , λ and ζ . Their values can be found in Table 5.3. These variables were fixed to reduce the number of free parameters in the fit and values chosen based on previous experience in LHCb. The mean mass (μ) was found to vary between simulated data and data in the control channel so the mean is allowed to float in the control channel in order to provide an offset to fix the mean in the signal channel case, i.e. the signal channel mean

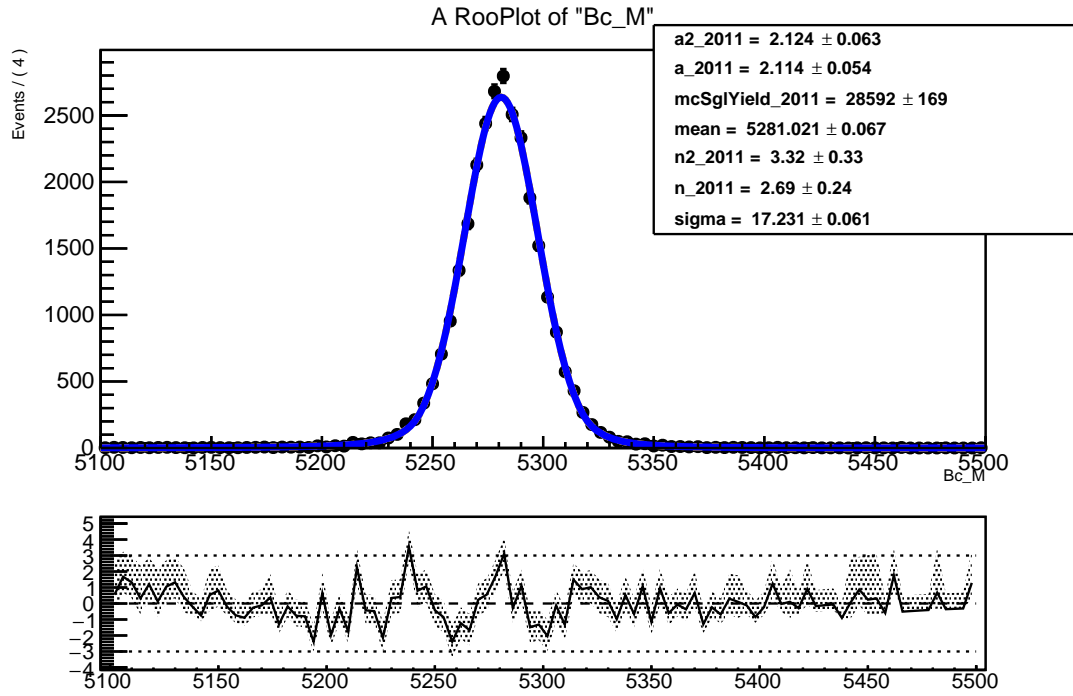
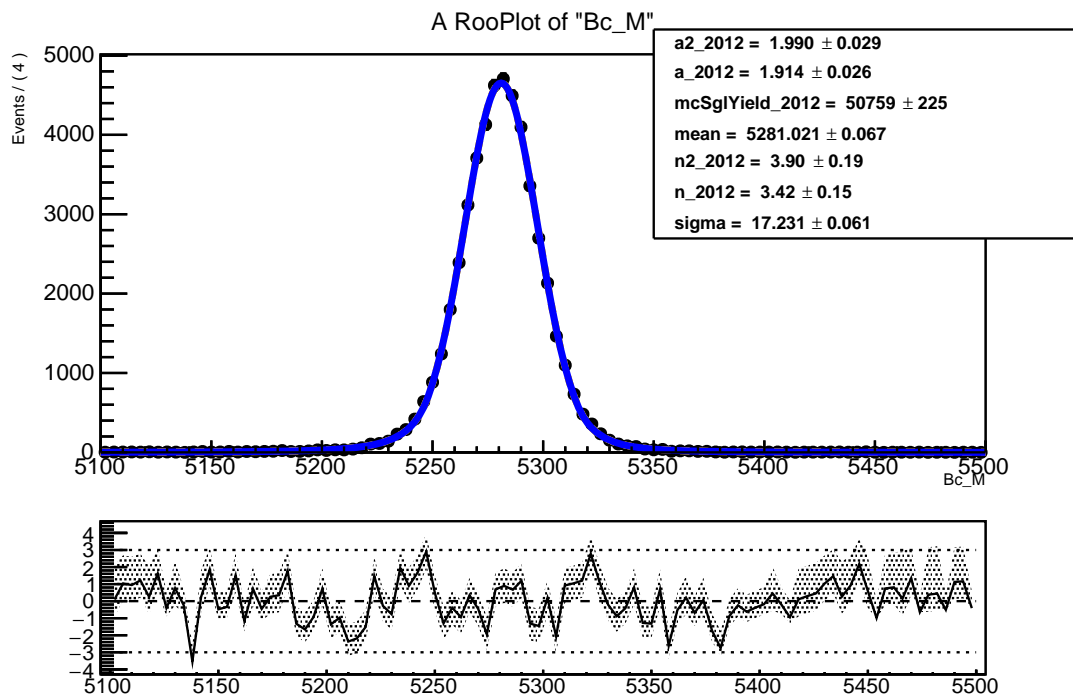
(a) Fit of 2011 control channel ($B^+ \rightarrow K^{*0}(892)(\rightarrow K^+\pi^-)\pi^+$) simulated data(b) Fit of 2012 control channel ($B^+ \rightarrow K^{*0}(892)(\rightarrow K^+\pi^-)\pi^+$) simulated data

Figure 5.13: Fit to simulated data for the control channel using Ipatia distribution.

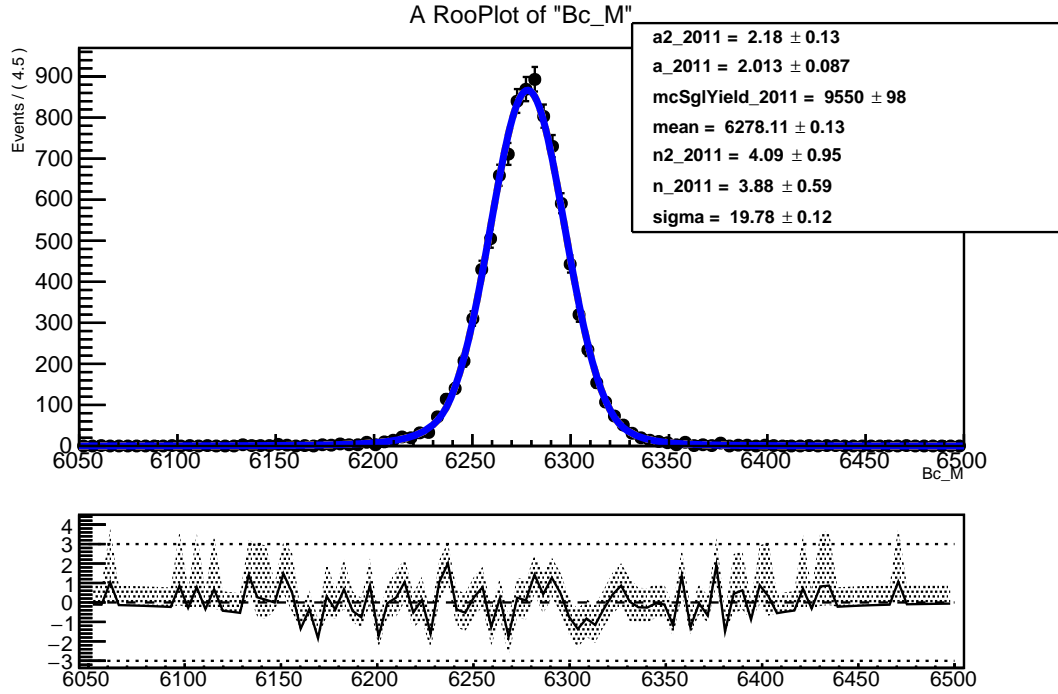
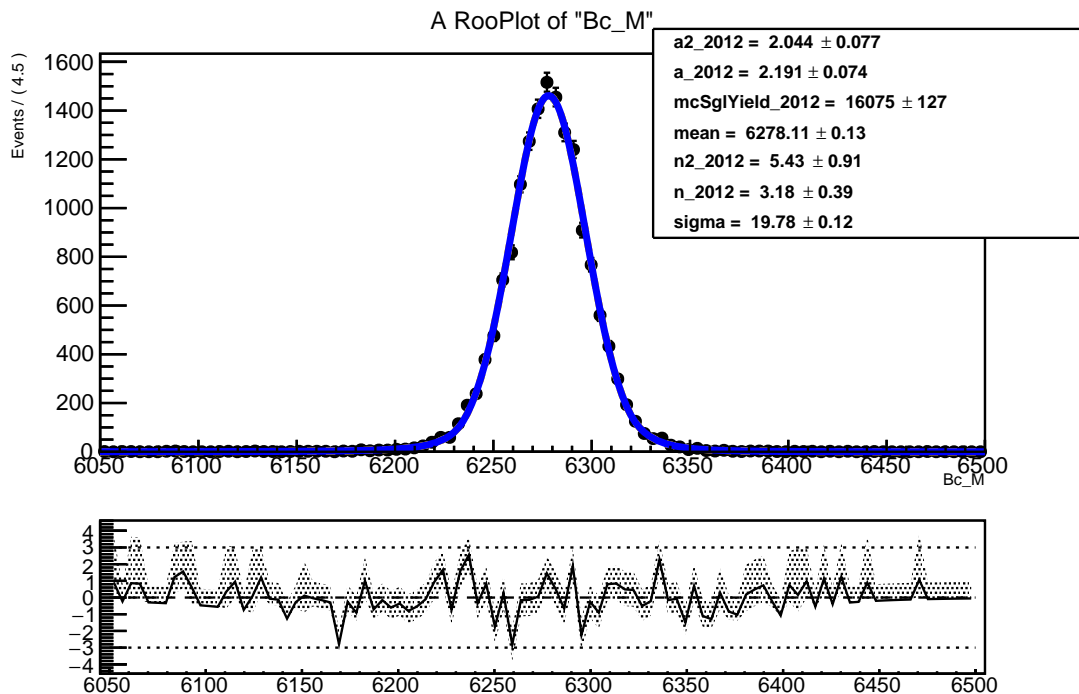
(a) Fit of 2011 control channel ($B_c^+ \rightarrow \bar{K}^{*0}(892)(\rightarrow K^- \pi^+) K^+$) simulated data(b) Fit of 2012 control channel ($B_c^+ \rightarrow \bar{K}^{*0}(892)(\rightarrow K^- \pi^+) K^+$) simulated data

Figure 5.14: Fit to simulated data for the signal channel using Ipatia distribution.

Table 5.3: Values of parameters held constant in final Ipatia function.

Symbol	Value
β	0.0
λ	-20.0
ζ	0.005

mass is Gaussian constrained with a mean of

$$\mu_{\text{data,signal channel}} = \mu_{\text{MC,signal channel}} + (\mu_{\text{data,control channel}} - \mu_{\text{MC,control channel}}), \quad (5.5)$$

and a width equal to the error propagated to $\mu_{\text{data,signal channel}}$.

Using MC data to test there were no mis-ID peaks in the signal region (e.g. simulating a $K\pi$ swap), it was established that there is only one significant component to the background for the $B^+ \rightarrow K^{*0}(892)(\rightarrow K^+\pi^-)\pi^+$ case: combinatorial. The combinatorial background is modelled as a first order Chebyshev polynomial with the parameter $a_{0,\text{cheby}}$.

The fit results for the $B^+ \rightarrow K^{*0}(892)(\rightarrow K^+\pi^-)\pi^+$ case can be found in Figures 5.15 and 5.16. Reasonable agreement can be found in both figures with $\sim 99\%$ of the pulls within 3σ . The behaviour of the tails is slightly different between years and therefore 2011 and 2012 data are considered separately, but with the mean and sigma parameters shared.

Due to the relatively high mass of the B_c meson the only significant contribution to background is combinatorial in nature. This is parameterised by a first order Chebyshev polynomial as shown in Figure 5.17, prior to unblinding signal region.

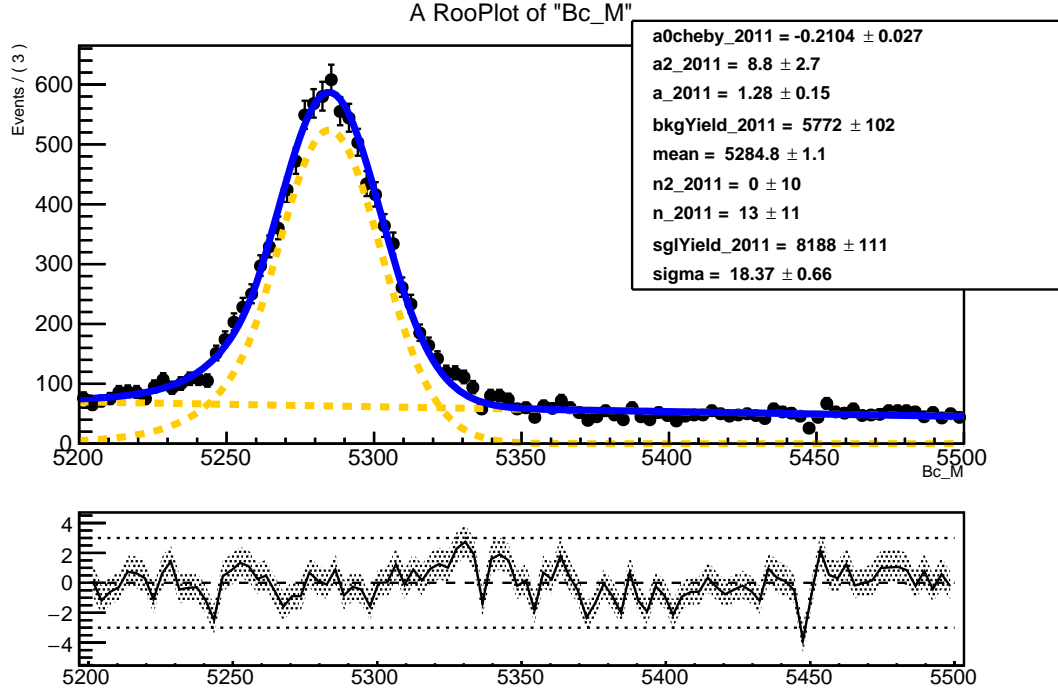


Figure 5.15: Fit of 2011 control channel ($B^+ \rightarrow K^{*0}(892)(\rightarrow K^+ \pi^-) \pi^+$) data.

5.3.2 Expected results

Using the information from the control channel, the relative efficiencies between the control and rare channel (detailed in section 5.4) are calculated as:

$$\left(\frac{\epsilon_{MC, B_c^+}}{\epsilon_{MC, B^+}} \right)_{2011} = 0.304 \pm 0.014, \quad (5.6)$$

$$\left(\frac{\epsilon_{MC, B_c^+}}{\epsilon_{MC, B^+}} \right)_{2012} = 0.307 \pm 0.013. \quad (5.7)$$

Assuming

$$\frac{\epsilon_{data, B_c^+}}{\epsilon_{data, B^+}} = \frac{\epsilon_{MC, B_c^+}}{\epsilon_{MC, B^+}}, \quad (5.8)$$

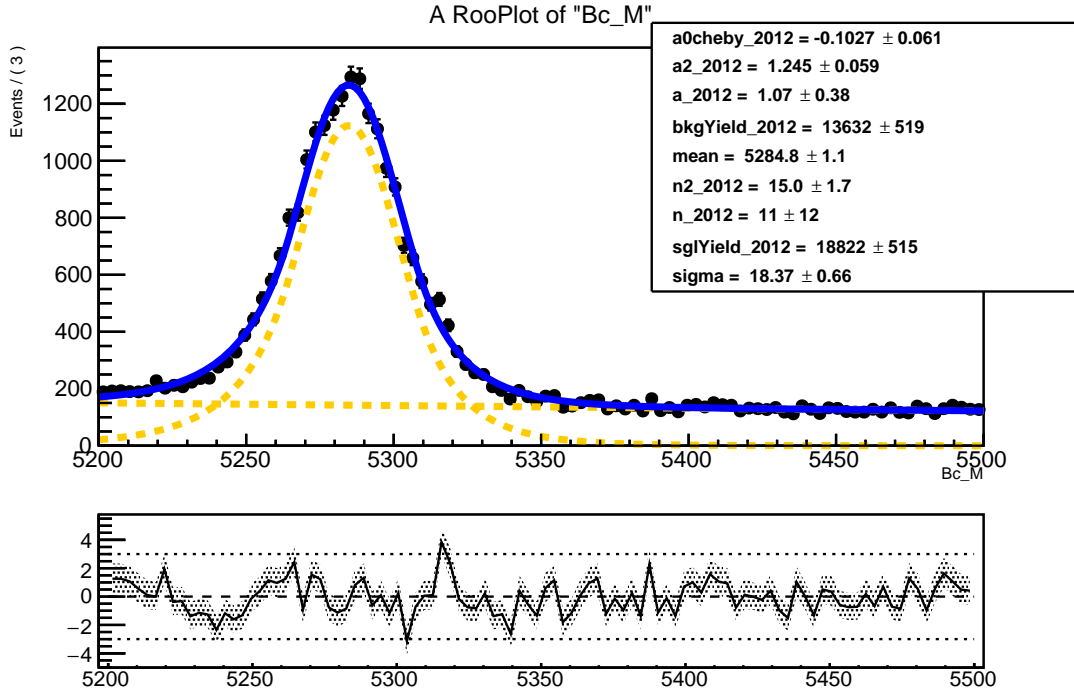
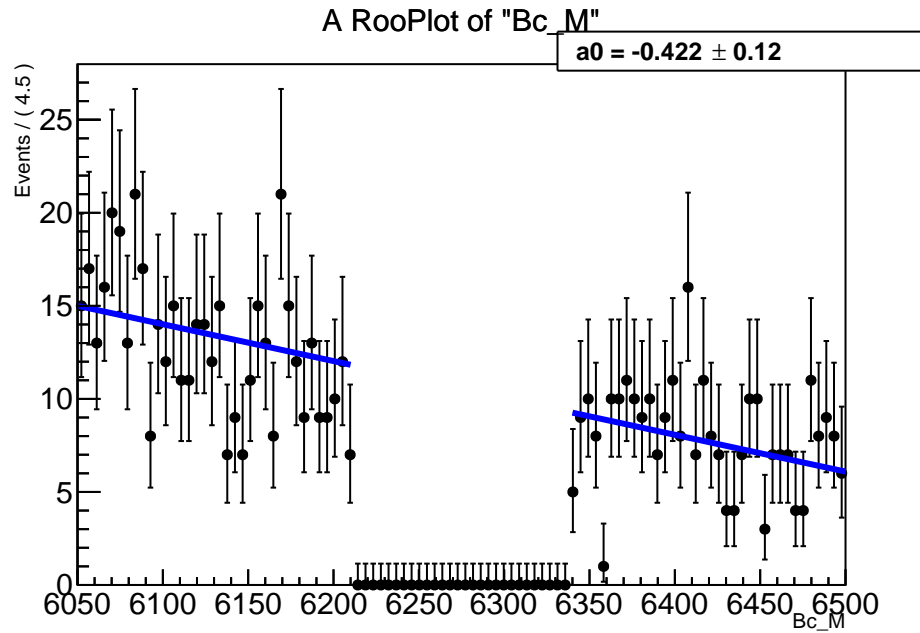


Figure 5.16: Fit of 2012 control channel ($B^+ \rightarrow K^{*0}(892)(\rightarrow K^+ \pi^-) \pi^+$) data.

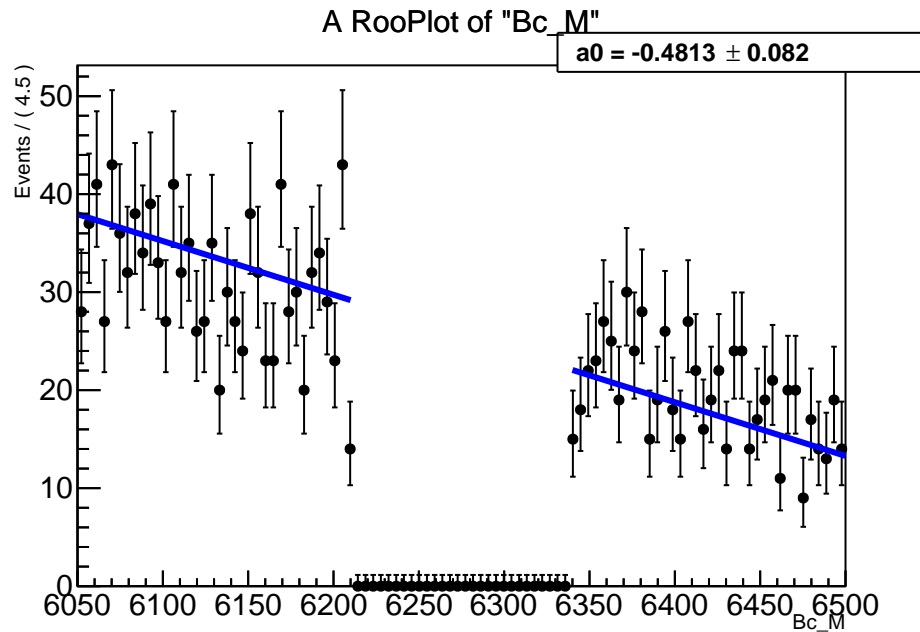
the expected efficiency of the B_c^+ case

$$\epsilon_{\text{data}, B_c^+, 2011} = \left(\frac{\epsilon_{\text{MC}, B^+}}{\epsilon_{\text{MC}, B_c^+}} \times \epsilon_{\text{data}, B^+} \right)_{2011} = 0.098 \pm 0.010, \quad (5.9)$$

$$\epsilon_{\text{data}, B_c^+, 2012} = \left(\frac{\epsilon_{\text{MC}, B^+}}{\epsilon_{\text{MC}, B_c^+}} \times \epsilon_{\text{data}, B^+} \right)_{2012} = 0.111 \pm 0.012, \quad (5.10)$$



(a) Signal channel sidebands 2011



(b) Signal channel sidebands 2012

Figure 5.17: Background sidebands for $B_c^+ \rightarrow \bar{K}^{*0}(892)(\rightarrow K^- \pi^+) K^+$, (top: 2011, bottom: 2012). As the fits are unbinned, the binning shown here does not affect the fit.

where $\epsilon_{\text{data},B^+}$ is $N_{\text{observed}}/N_{\text{produced}}$ for the B^+ case. Rates taken from section 1.2 give the following predicted results

$$\frac{N_{\text{predicted},B_c^+,2011}}{N_{\text{predicted},B^+,2011}} \sim [0.1, 2.5] \times 10^{-4}, \quad (5.11)$$

$$\frac{N_{\text{predicted},B_c^+,2012}}{N_{\text{predicted},B^+,2012}} \sim [0.2, 2.8] \times 10^{-4} \quad (5.12)$$

where $N_{\text{predicted}} = \mathcal{L} \sigma \epsilon_{\text{MC}}$.

This gives an estimate for the number of observed events in the B_c channel to be of:

$$N_{\text{observed},B_c^+,2011} = \frac{N_{\text{predicted},B_c^+,2011}}{N_{\text{predicted},B^+,2011}} \times N_{\text{observed},B^+,2011} \sim [0.1, 2.0] \text{ events}, \quad (5.13)$$

$$N_{\text{observed},B_c^+,2012} = \frac{N_{\text{predicted},B_c^+,2012}}{N_{\text{predicted},B^+,2012}} \times N_{\text{observed},B^+,2012} \sim [0.3, 5.3] \text{ events}. \quad (5.14)$$

5.3.3 Fit results

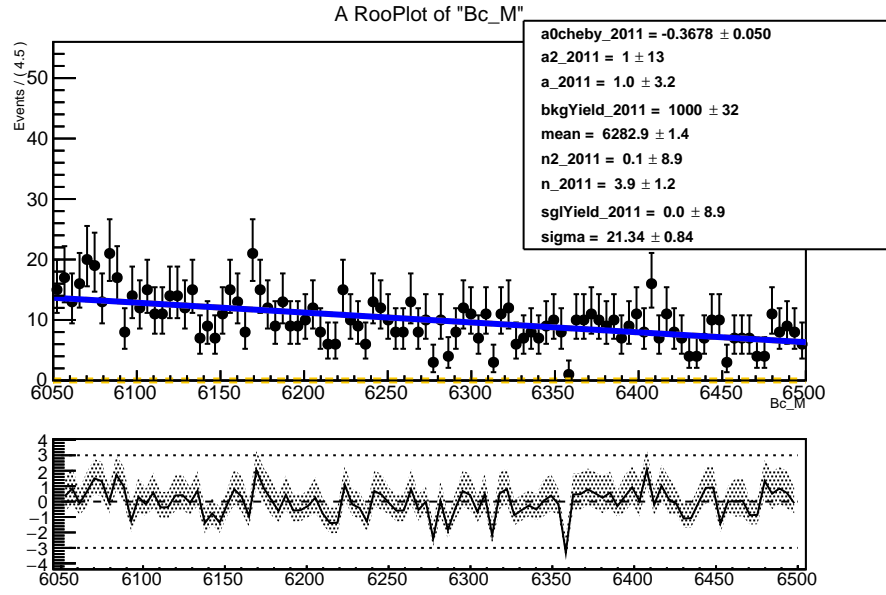
The unblinded fits shown in Figure 5.18 show no significant yield detected. Although disappointing, this non-observation is consistent with the previous hints from [29] given the significance of those results.

Assuming that this analysis will be extended later using Run 2 results, no limits will be set based on this analysis these data. The following section details estimated efficiencies and systematic errors.

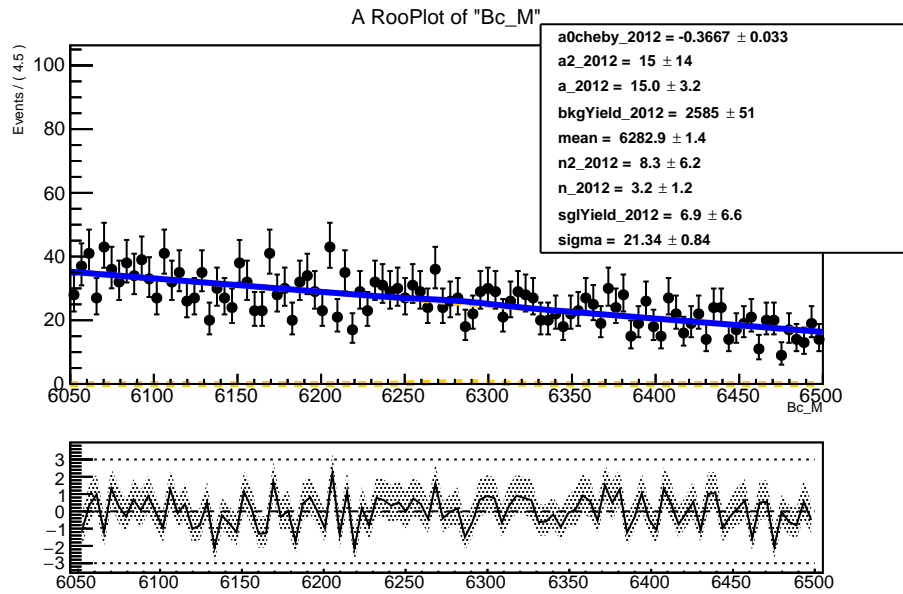
5.4 Efficiencies

The efficiencies for this analysis can be described by

$$\epsilon_{\text{tot|geometry}} = \epsilon_{\text{stripping,presel|geometry}} \epsilon_{\text{trig|strip,presel,geo}} \epsilon_{\text{bdt|trig,strip,presel,geo}}, \quad (5.15)$$



(a) Fit of 2011 signal channel ($B_c^+ \rightarrow \bar{K}^{*0}(892) (\rightarrow K^- \pi^+) K^+$) data



(b) Fit of 2012 signal channel ($B_c^+ \rightarrow \bar{K}^{*0}(892) (\rightarrow K^- \pi^+) K^+$) data

Figure 5.18: Unblinded data fits for $B_c^+ \rightarrow \bar{K}^{*0}(892) (\rightarrow K^- \pi^+) K^+$.

where $\epsilon_{\text{tot|geometry}}$ quantifies the total efficiency for selecting the control or signal decays within the LHCb acceptance, $\epsilon_{\text{stripping,preSEL|geometry}}$ quantifies the efficiency of selection given particles within the LHCb acceptance, the $\epsilon_{\text{trig|strip,preSEL,geo}}$ is the trigger efficiency (given the previous) and $\epsilon_{\text{bdT|trig,strip,preSEL,geo}}$ describes the efficiency of the BDT cut applied as the last stage of the selection.

5.4.1 Selection efficiency

The selection efficiency, $\epsilon_{\text{tot|geometry}}$, is calculated by applying the selection described in section 5.2 to simulated signal or control channel data. For a breakdown of these efficiencies, see tables 5.4 and 5.5.

The stripping/preselection efficiency, $\epsilon_{\text{stripping,preSEL|geometry}}$, describes the number of candidate decays that are reconstructed and that pass the cuts in the selection compared to the number of events created within the acceptance of LHCb⁵. It is evaluated by applying the selection, without the trigger cuts, on the simulated data and calculating relative to the number of events within the acceptance.

Trigger given stripping/preselection, $\epsilon_{\text{trig|strip,preSEL,geo}}$, efficiency is calculated using simulated events, with the exception of HLT1 which uses the data-driven TISTOS method described in subsection 5.2.1.

As seen in tables 5.4 and 5.5, the largest contribution to inefficiency is the initial preselection ($\epsilon_{\text{stripping,preSEL|geometry}}$). This efficiency is comparable with that of [29] which is expected as the stripping selection is identical, differing only in the $K^{*0}(892)$ mass window requirement. Other efficiencies are also broadly similar, noting that the current analysis is optimised for the reson-

⁵Usually, there would be a geometric efficiency describing the difference between the total number of events produced and the number produced within the LHCb acceptance but since the branching ratio obtained for $B^+ \rightarrow K^{*0}(892)(\rightarrow K^+\pi^-)\pi^+$ is already calculated within the same acceptance, this is not needed.

Table 5.4: Efficiencies for simulated data for the control channel.

Name	Symbol	2011	2012
Stripping	$\epsilon_{\text{stripping,presel,geometry}}$	0.0934 ± 0.0004	0.0869 ± 0.0004
L0	$\epsilon_{\text{L0 strip,presel,geo}}$	0.563 ± 0.015	0.530 ± 0.014
HLT1 (given L0)	$\epsilon_{\text{HLT1 L0,strip,presel,geo}}$	0.809 ± 0.005	0.805 ± 0.004
HLT2 (given L0, HLT1)	$\epsilon_{\text{HLT2 L0,HLT1,strip,presel,geo}}$	0.850 ± 0.006	0.923 ± 0.005
BDT (given above)	$\epsilon_{\text{bdt trig,strip,presel,geo}}$	0.758 ± 0.006	0.688 ± 0.004
total	$\epsilon_{\text{tot geo}}$	0.0274 ± 0.0008	0.0235 ± 0.0006

Table 5.5: Efficiencies for simulated data for the signal channel.

Name	Symbol	2011	2012
Stripping	$\epsilon_{\text{stripping,presel,geometry}}$	0.03594 ± 0.00016	0.03437 ± 0.00015
L0	$\epsilon_{\text{L0 strip,presel,geo}}$	0.525 ± 0.018	0.491 ± 0.016
HLT1 (given L0)	$\epsilon_{\text{HLT1 L0,strip,presel,geo}}$	0.771 ± 0.008	0.770 ± 0.006
HLT2 (given L0, HLT1)	$\epsilon_{\text{HLT2 L0,HLT1,strip,presel,geo}}$	0.751 ± 0.009	0.806 ± 0.007
BDT (given above)	$\epsilon_{\text{bdt trig,strip,presel,geo}}$	0.762 ± 0.010	0.689 ± 0.007
total	$\epsilon_{\text{tot geo}}$	0.00833 ± 0.00032	0.00721 ± 0.00025

ant K^{*0} (892) annihilation channel while those of reference [29] are optimised for the inclusive selection including $B_c \rightarrow D^0(\rightarrow KK)\pi$; $B_c \rightarrow B_s(\rightarrow KK)\pi$; and $B_c \rightarrow \chi_{c0}(\rightarrow KK)\pi$.

5.5 Systematic errors

Systematic errors are evaluated prior to unblinding using simulated data for signal and control channels, and data for control channel where appropriate.

Given the low expected yield, only those sources of systematic uncertainty, that are considered to be important are evaluated quantitatively, including: modelling of background (exponential vs.

polynomial); choice of signal PDF; and toy studies to investigate the stability of the fit from which yield is extracted.

5.5.1 Fit model choices

The choice of an Ipatia function in subsection 5.3.1 is not the only viable choice; an alternative that gives a comparable quality of fit is the DCB. A single CB function is built with a Gaussian core and a radiative tail that uses a power law. Mathematically, this takes the form:

$$f(x|a, n, \mu, \sigma) \propto \begin{cases} \exp\left(-\frac{(x-\mu)^2}{2\sigma^2}\right), & \text{for } \frac{x-\bar{x}}{\sigma} > -a \\ A\left(B - \frac{x-\mu}{\sigma}\right)^{-n}, & \text{for } \frac{x-\mu}{\sigma} \leq -a \end{cases} \quad (5.16)$$

where $A = \left(\frac{n}{|a|}\right)^n \exp\left(-\frac{|a|^2}{2}\right)$ and $B = \frac{n}{|a|} - |a|$. A DCB is the sum of two independent CB functions with a shared mean, μ , and width, σ . As such, the data for the control channel are fitted with a DCB and the parameters compared with the Ipatia function. The plots of these fits can be seen in figs. 5.19 and 5.20

The background model is treated similarly, with an exponential function being compared with the choice of Chebyshev polynomial. The plots are shown in figs. 5.21 and 5.22. A qualitative assessment and technical challenges (i.e. unstable fits when background event number changed) found when fitting an exponential function to control channel data in the full fits led to a Chebyshev polynomial being used for the final analysis.

To investigate the dependence on the extracted signal yield on the choice of signal PDF, two fits are performed to data and simulated data for the control channel: one using Ipatia and one using DCB PDFs (figs. 5.19 and 5.20). The differences between those are shown in Table 5.6. While the changes in the mean between Ipatia and DCB (μ) values are completely consistent with zero, there

Table 5.6: Comparisons of variables between Ipatia and DCB fit.

Identifier	μ_{Ipatia}	μ_{DCB}	$\mu_{\text{Ipatia}} - \mu_{\text{DCB}}$	$\mu_{\text{Ipatia}}/\mu_{\text{DCB}}$
MC	5281.02 ± 0.07	5281.04 ± 0.07	-0.02 ± 0.10	0.999996 ± 0.000019
DATA	5284.8 ± 1.1	5284.4 ± 0.6	0.4 ± 1.3	1.00007 ± 0.00024
Identifier	σ_{Ipatia}	σ_{DCB}	$\sigma_{\text{Ipatia}} - \sigma_{\text{DCB}}$	$\sigma_{\text{Ipatia}}/\sigma_{\text{DCB}}$
MC 2011	17.23 ± 0.06	16.70 ± 0.08	0.53 ± 0.10	1.032 ± 0.006
MC 2012	17.23 ± 0.06	16.70 ± 0.08	0.53 ± 0.10	1.032 ± 0.006
DATA 2011	18.4 ± 0.7	18.4 ± 1.0	0.0 ± 1.2	1.00 ± 0.06
DATA 2012	18.4 ± 0.7	18.4 ± 1.0	0.0 ± 1.2	1.00 ± 0.06
Identifier	N_{Ipatia}	N_{DCB}	$N_{\text{Ipatia}} - N_{\text{DCB}}$	$N_{\text{DCB}}/N_{\text{Ipatia}}$
MC 2011	$(2.859 \pm 0.017) \times 10^4$	$(2.859 \pm 0.017) \times 10^4$	$(-0.0 \pm 2.4) \times 10^2$	1.000 ± 0.008
MC 2012	$(5.076 \pm 0.023) \times 10^4$	$(5.076 \pm 0.023) \times 10^4$	$(0.0 \pm 3.2) \times 10^2$	1.000 ± 0.006
DATA 2011	$(8.19 \pm 0.11) \times 10^3$	$(9.2 \pm 0.5) \times 10^3$	$(-1.0 \pm 0.6) \times 10^3$	1.12 ± 0.07
DATA 2012	$(1.88 \pm 0.05) \times 10^4$	$(1.969 \pm 0.011) \times 10^4$	$(-9 \pm 5) \times 10^2$	1.046 ± 0.029

are small differences in the corresponding change in the width (σ) parameters in simulated data. Looking at the overall effect in the yield (N), there is no significant difference between the values extracted of the two PDFs. This is for a relatively large sample size for the control channel, which may not be reflected for low signal yield case of the signal channel.

For a more thorough evaluation toy studies could be carried out in the following manner: generate toy datasets, each corresponding to a distinct mass distribution which has been randomly generated based on the signal PDF fit to simulated data; perform fits to each toy dataset with an Ipatia and a DCB; collect the fit results; examine the distribution of the per-toy differences and evaluate the significance of the difference from zero. This procedure would be carried out for a variety of expected signal yields e.g. 10, 100, etc., as the behaviour of the difference distribution may be a function of the signal yield.

Given the low expected yield in the signal channel, this study was deferred until after unblinding. Consequently, as no signal yield was observed this study was not carried out.

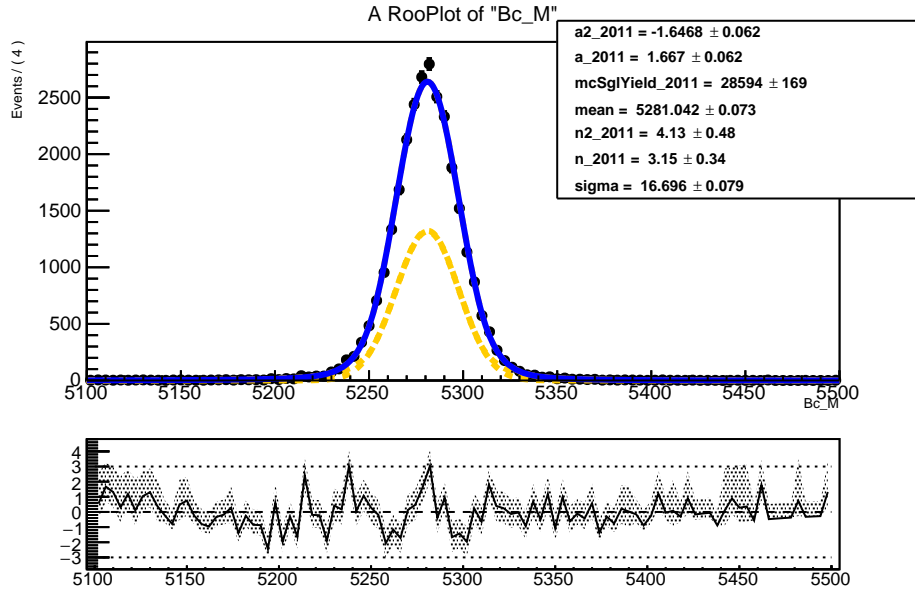
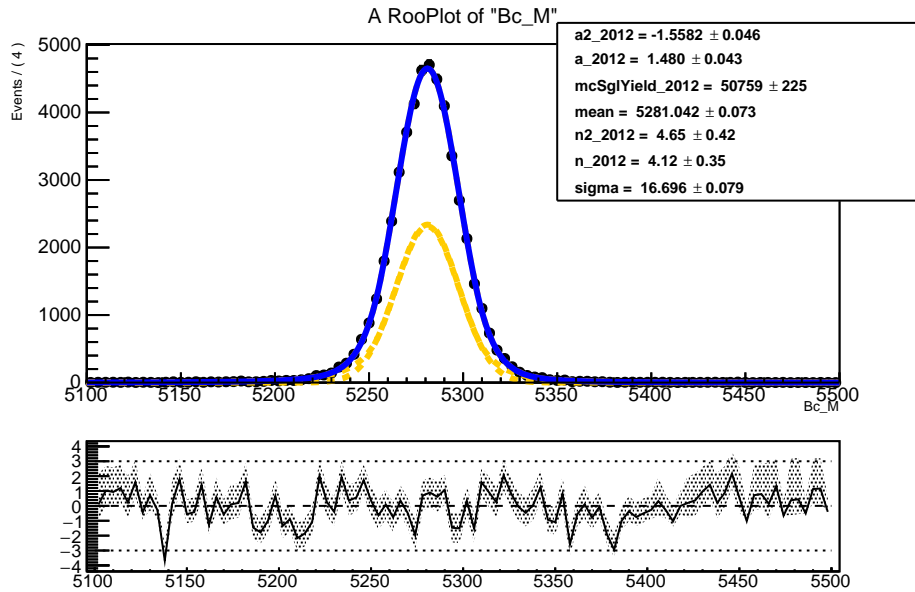
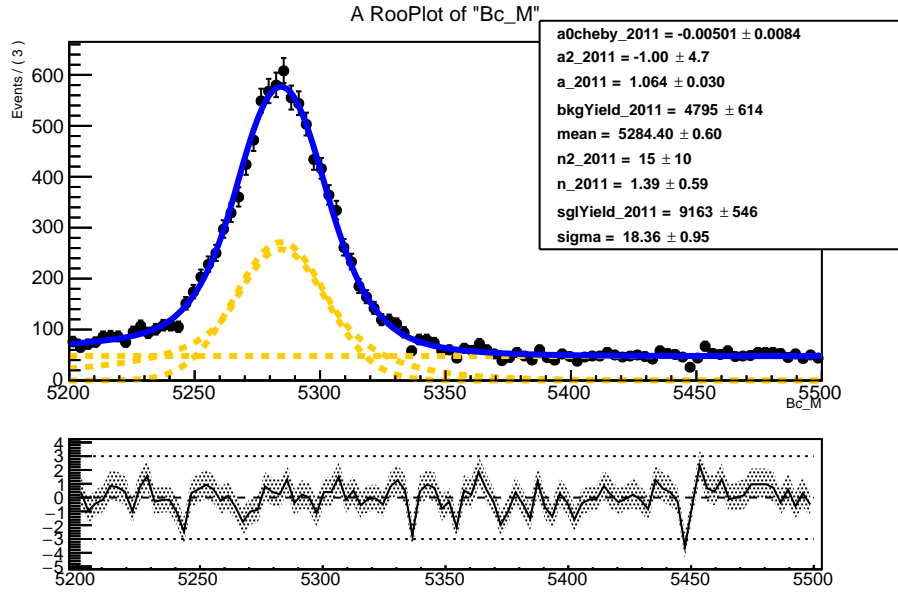
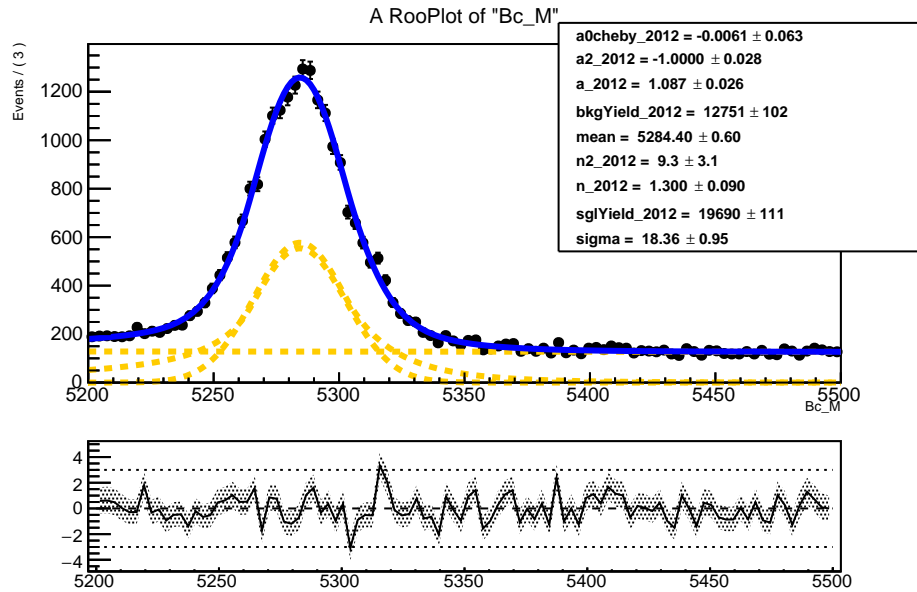
(a) DCB MC fit for $B^+ \rightarrow K^{*0}(892)(\rightarrow K^+ \pi^-) \pi^+$ 2011(b) DCB MC fit for $B^+ \rightarrow K^{*0}(892)(\rightarrow K^+ \pi^-) \pi^+$ 2012

Figure 5.19: DCB fit to control channel simulated data 2011

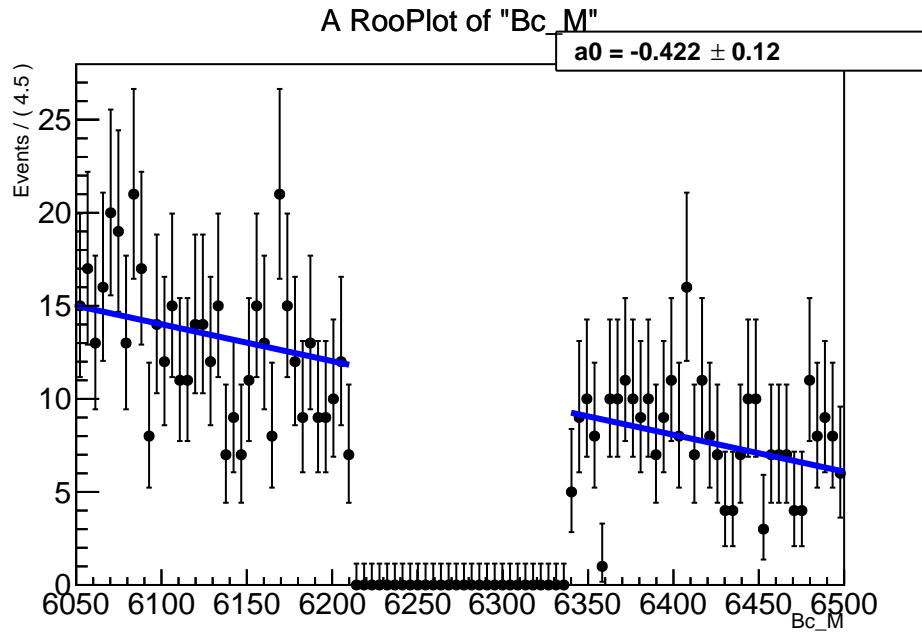


(a) DCB data fit for $B^+ \rightarrow K^{*0}(892)(\rightarrow K^+ \pi^-) \pi^+$ 2011

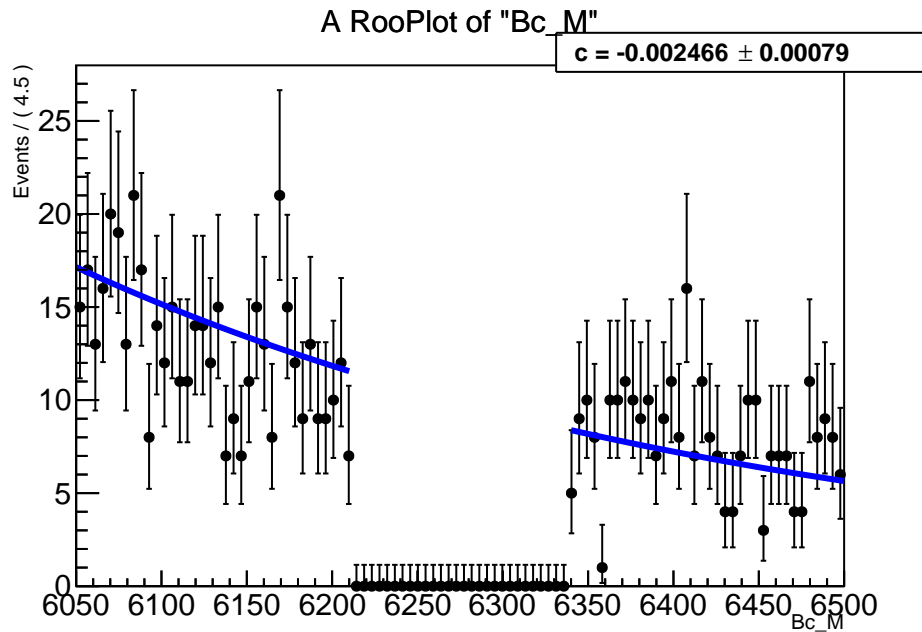


(b) DCB data fit for $B^+ \rightarrow K^{*0}(892)(\rightarrow K^+ \pi^-) \pi^+$ 2012

Figure 5.20: DCB fit to control channel data 2011

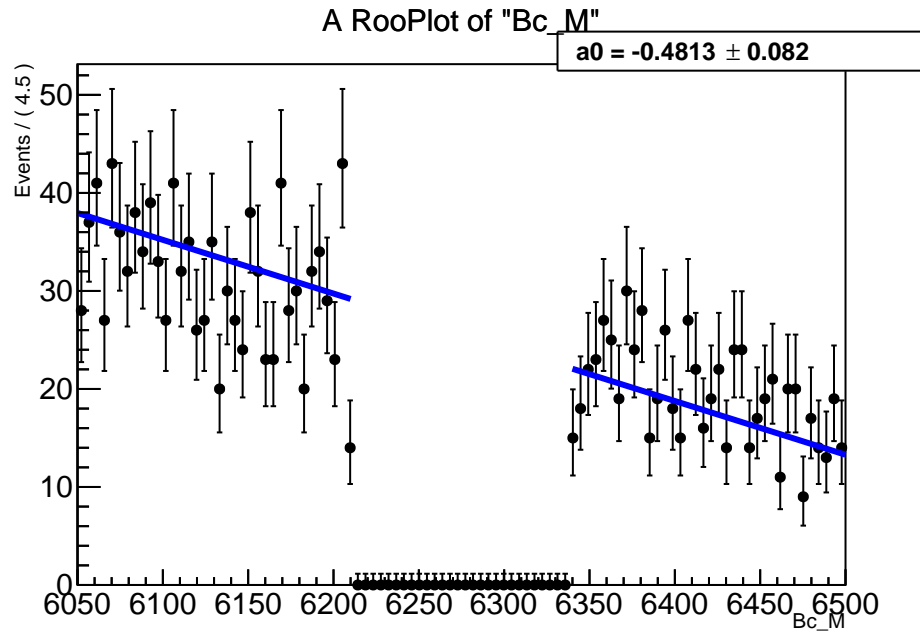


(a) Fit with polynomial.

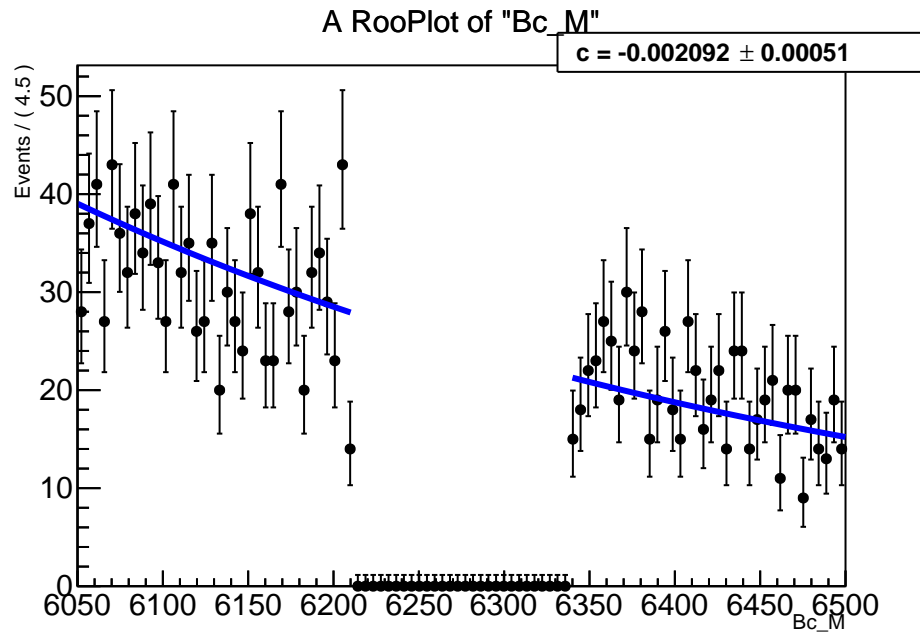


(b) Fit with exponential.

Figure 5.21: Background fit of 2011 signal channel for $B_c^+ \rightarrow \bar{K}^{*0}(892)(\rightarrow K^- \pi^+) K^+$ data



(a) Fit with polynomial.



(b) Fit with exponential.

Figure 5.22: Background fit of 2012 signal channel for $B_c^+ \rightarrow \bar{K}^{*0}(892)(\rightarrow K^- \pi^+)K^+$ data

5.5.2 Toy studies

Toy studies are performed to test the quality of the fit model. A bad fit model will have difficulty fitting to the data without heavy fine tuning; a good or stable model will have a lower sensitivity to the arbitrarily chosen initial parameter values used in the fit and the extracted yield match the actual number of signal candidates in the distribution.

As can be seen in Figure 5.23, the toy studies show good overall behaviour with the extracted number of candidates reflecting the true number of candidates in the distribution over a wide range of generated candidate yields down to ~ 30 signal events.

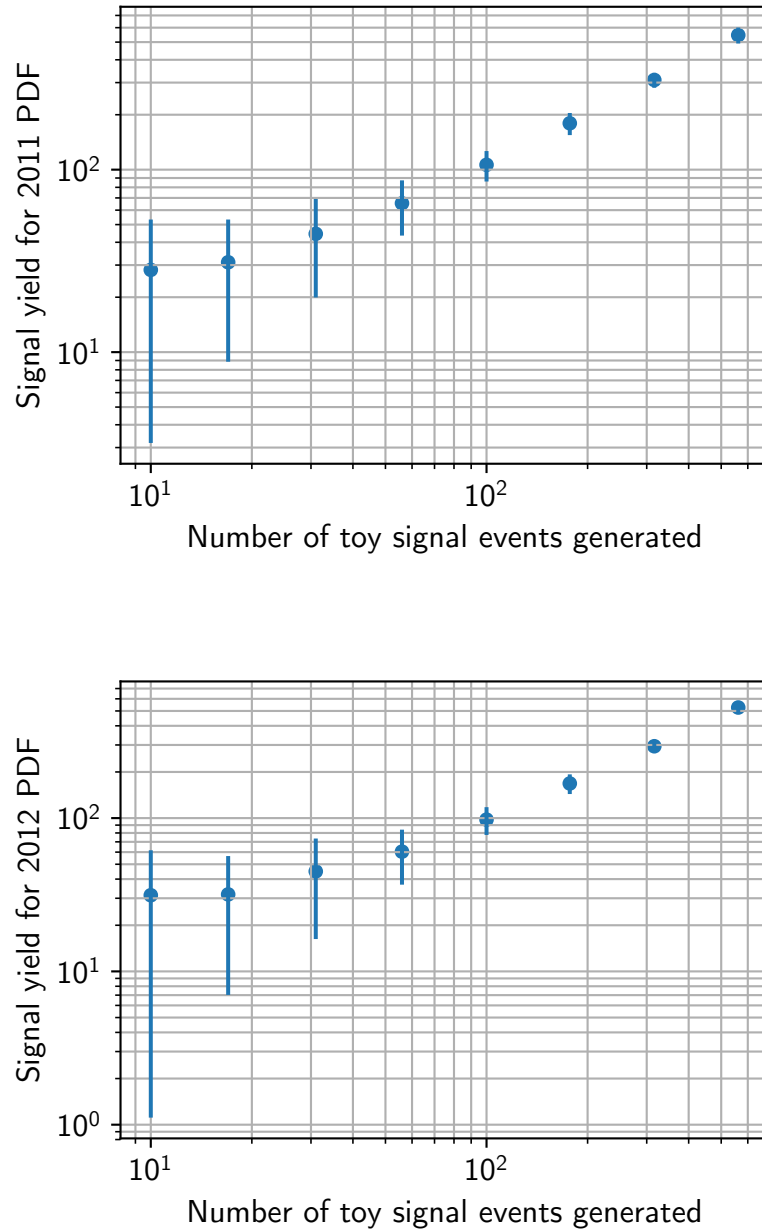


Figure 5.23: Toy studies for the $B^+ \rightarrow K^{*0}(892)(\rightarrow K^+\pi^-)\pi^+$ case with a background of 100 events i.e. a simulation of $B_c^+ \rightarrow \bar{K}^{*0}(892)(\rightarrow K^-\pi^+)K^+$ (upper: 2011; lower: 2012)

Chapter 6

Conclusion

The work presented in this thesis describes three distinct areas of research ranging from testing future components of the LHCb detector, to developing a novel QA framework with continuous integration which is well suited to the needs of particle physics software, to searching for the unobserved decay $B_c^+ \rightarrow \bar{K}^{*0}(892)(\rightarrow K^- \pi^+) K^+$.

Testing the Hamamatsu R12699 PMT provided an important investigation to resolve the ambiguous behaviour of the device when exposed to a large fluence of photons. Despite a large spread between cells in the PMT, the overall trend of loss of anode sensitivity found that the device is likely to satisfy the performance requirements for LHCb Run 3.

LHCbPR2 provides a custom framework using a microservice architecture for the testing of particle physics software[89]. Loosely coupled components allow for flexible data formats and for individual components to be deployed at different rates e.g. once every quarter to many times a day. This is being rolled out within LHCb to reduce the overall workload on a small group of experts by

automating everyday tasks e.g. generating samples of events, testing new software combinations, running test jobs, etc..

A search for the charmless B_c annihilation process $B_c^+ \rightarrow \bar{K}^{*0}(892)(\rightarrow K^- \pi^+)K^+$ was carried out, using the $B^+ \rightarrow K^{*0}(892)(\rightarrow K^+ \pi^-)\pi^+$ as a control channel to validate the method and modeling. Although the procedure developed was robust, the improvement in performance over [29] was not sufficient to provide an observation. As limits for this decay were set using the same data and performance was comparable, no new limits were set here.

The search for $B_c^+ \rightarrow \bar{K}^{*0}(892)(\rightarrow K^- \pi^+)K^+$ is expected to continue to be developed using Run 2 data where a first observation of this annihilation process may be possible.

LHCbPR2 is currently being extended to provide easier integration of a more diverse sets of tests, including those from end user physics analyses which depend on upcoming software versions rather than technical tests to benchmarking simulation. Building on the success of the developments in this thesis and interests expressed at the IEEE NSS/MIC/RTSD 2017 conference[89], preparations are in hand for LHCbPR2 to be released as a public-facing open source project which may be of interest to other large physics software collaborations.

References

- [1] E. J. Lofgren. “Experiences with the Bevatron”. In: (Apr. 1956). DOI: 10.2172/877349.
- [2] J. Naisse. “Experiment and the ρ -meson”. In: *Physics Letters* 1.7 (July 1962), pp. 247–249. ISSN: 0031-9163. DOI: 10.1016/0031-9163(62)91367-7.
- [3] V. D. Hopper and S. Biswas. “Evidence Concerning the Existence of the New Unstable Elementary Neutral Particle”. In: *Physical Review* 80.6 (Dec. 1950), pp. 1099–1100. ISSN: 1536-6065. DOI: 10.1103/PhysRev.80.1099.
- [4] A. Pevsner et al. “Evidence for a Three Pion Resonance Near 550-MeV”. In: *Phys.Rev.Lett* 7 (1961), pp. 421–423. DOI: 10.1103/PhysRevLett.7.421.
- [5] R. P. Feynman. “The Behavior of Hadron Collisions at Extreme Energies”. In: *Special Relativity and Quantum Theory: A Collection of Papers on the Poincaré Group*. Ed. by M. E. Noz and Y. S. Kim. Dordrecht: Springer Netherlands, 1988, pp. 289–304. ISBN: 978-94-009-3051-3. DOI: 10.1007/978-94-009-3051-3_25. URL: https://doi.org/10.1007/978-94-009-3051-3_25.
- [6] M. Gell-Mann. “A schematic model of baryons and mesons”. In: *Physics Letters* 8.3 (Feb. 1964), pp. 214–215. ISSN: 0031-9163. DOI: 10.1016/S0031-9163(64)92001-3.

- [7] M. Breidenbach et al. “Observed Behavior of Highly Inelastic Electron-Proton Scattering”. In: *Physical Review Letters* 23.16 (Oct. 1969), pp. 935–939. ISSN: 1079-7114. DOI: 10.1103/PhysRevLett.23.935.
- [8] J. J. Aubert et al. “Experimental Observation of a Heavy Particle J ”. In: *Physical Review Letters* 33.23 (Dec. 1974), pp. 1404–1406. ISSN: 1079-7114. DOI: 10.1103/PhysRevLett.33.1404.
- [9] J.-E. Augustin et al. “Discovery of a Narrow Resonance in e^+e^- Annihilation”. In: *Physical Review Letters* 33.23 (Dec. 1974), pp. 1406–1408. ISSN: 1079-7114. DOI: 10.1103/PhysRevLett.33.1406.
- [10] S. W. Herb et al. “Observation of a Dimuon Resonance at 9.5 GeV in 400-GeV Proton-Nucleus Collisions”. In: *Physical Review Letters* 39.5 (Aug. 1977), pp. 252–255. ISSN: 1079-7114. DOI: 10.1103/PhysRevLett.39.252.
- [11] D0 Collaboration et al. “Search for High Mass Top Quark Production in $p\bar{p}$ Collisions at $\sqrt{s} = 1.8$ TeV”. In: *Physical Review Letters* 74.13 (Mar. 1995), pp. 2422–2426. ISSN: 1079-7114. DOI: 10.1103/PhysRevLett.74.2422.
- [12] Particle Data Group et al. “Review of Particle Physics”. In: *Physical Review D* 98.3 (Aug. 2018), p. 030001. ISSN: 2470-0029. DOI: 10.1103/PhysRevD.98.030001.
- [13] F. A. Scott. “Energy Spectrum of the Beta-Rays of Radium E”. In: *Phys. Rev.* 48.5 (Sept. 1935), pp. 391–395. DOI: 10.1103/PhysRev.48.391.
- [14] S. Mertens. “Direct Neutrino Mass Experiments”. In: *J. Phys. Conf. Ser.* 718.2 (May 2016), p. 022013. ISSN: 1742-6596. DOI: 10.1088/1742-6596/718/2/022013.

- [15] C. L. Cowan Jr. et al. “Detection of the Free Neutrino: A Confirmation”. In: *Science* 124 (July 1956), pp. 103–104. ISSN: 0036-8075. DOI: 10.1126/science.124.3212.103.
- [16] G. J. Aubrecht. “The Fundamental Particles and Interactions Wall Chart, The Teaching of Contemporary Physics, and the Future of the SSC”. In: *SpringerLink* (1991), pp. 525–536. DOI: 10.1007/978-1-4615-3746-5_52.
- [17] LHCb collaboration. “Observation of $J/\psi p$ resonances consistent with pentaquark states in $\Lambda_b^0 \rightarrow J/\psi p K^-$ decays”. In: *Phys. Rev. Lett.* 115 (2015), p. 072001. DOI: 10.1103/PhysRevLett.115.072001. arXiv: 1507.03414 [hep-ex].
- [18] H1 and ZEUS collaborations. “Pentaquark searches at HERA”. In: *Nucl. Phys. B Proc. Suppl.* 164 (Feb. 2007), pp. 113–116. ISSN: 0920-5632. DOI: 10.1016/j.nuclphysbps.2006.11.112.
- [19] B. Andersson et al. “Parton fragmentation and string dynamics”. In: *Physics Reports* 97.2 (July 1983), pp. 31–145. ISSN: 0370-1573. DOI: 10.1016/0370-1573(83)90080-7.
- [20] F. J. Dyson. “The Radiation Theories of Tomonaga, Schwinger, and Feynman”. In: *Physical Review* 75.3 (Feb. 1949), pp. 486–502. ISSN: 1536-6065. DOI: 10.1103/PhysRev.75.486.
- [21] B. C. Odom et al. “New Measurement of the Electron Magnetic Moment Using a One-Electron Quantum Cyclotron”. In: *Phys. Rev. Lett.* 97 (2006), p. 030801.
- [22] T. Aoyama et al. “Revised value of the eighth-order QED contribution to the anomalous magnetic moment of the electron”. In: *Phys. Rev. D* 77 (2008), p. 053012. DOI: 10.1103/PhysRevD.77.053012. arXiv: 0712.2607 [hep-ph].
- [23] Particle Data Group et al. “Review of Particle Physics”. In: *Physical Review D* 98.3 (Aug. 2018), p. 030001. ISSN: 2470-0029. DOI: 10.1103/PhysRevD.98.030001.

- [24] LHCb collaboration. “Observation of the decay $B_c^+ \rightarrow B_s^0 \pi^+$ ”. In: *Phys. Rev. Lett.* 111 (2013), p. 181801. DOI: 10.1103/PhysRevLett.111.181801. arXiv: 1308.4544 [hep-ex].
- [25] I. P. Gouz et al. “Prospects for the B_c studies at LHCb”. In: *Phys. At. Nucl.* 67.8 (Aug. 2004), pp. 1559–1570. ISSN: 1063-7788. DOI: 10.1134/1.1788046.
- [26] Z.-J. Xiao and X. Liu. “The two-body hadronic decays of B_c meson in the perturbative QCD approach: A short review”. In: *Chin. Sci. Bull.* 59 (2014), pp. 3748–3759. DOI: 10.1007/s11434-014-0418-z. arXiv: 1401.0151 [hep-ph].
- [27] Z. Rui and Z.-T. Zou. “S-wave ground state charmonium decays of B_c mesons in the perturbative QCD approach”. In: *Physical Review D* 90.11 (Dec. 2014), p. 114030. ISSN: 2470-0029. DOI: 10.1103/PhysRevD.90.114030.
- [28] LHCb collaboration. “Measurement of B_c^+ production at $\sqrt{s} = 8$ TeV”. In: *Phys. Rev. Lett.* 114 (2015), p. 132001. DOI: 10.1103/PhysRevLett.114.132001. arXiv: 1411.2943 [hep-ex].
- [29] LHCb collaboration. “Study of B_c^+ decays to the $K^+ K^- \pi^+$ final state and evidence for the decay $B_c^+ \rightarrow \chi_{c0} \pi^+$ ”. In: (2016). arXiv: 1607.06134 [hep-ex].
- [30] A. A. Alves Jr. et al. “The LHCb detector at the LHC”. In: *JINST* 3 (2008), S08005. DOI: 10.1088/1748-0221/3/08/S08005.
- [31] *LHCb bb production angle plots*. [Online; accessed 19. Dec. 2018]. Nov. 2013. URL: https://lhcb.web.cern.ch/lhcb/speakersbureau/html/bb_ProductionAngles.html.
- [32] D. Eckstein. *The LHCb VERtex LOcator*. 2003. URL: http://lhcb-doc.web.cern.ch/lhcb-doc/presentations/conferencetalks/postscript/2003presentations/lhcb2003_099.pdf.

- [33] P. N. Griffith. *First observation and branching fraction measurement of the rare decay $\Lambda_b^0 \rightarrow pK\mu^+\mu^-$ at the LHCb experiment, CERN.*
- [34] M. Adinolfi et al. “Performance of the LHCb RICH detector at the LHC”. In: *Eur. Phys. J. C* 73 (2013), p. 2431. DOI: 10.1140/epjc/s10052-013-2431-9. arXiv: 1211.6759 [physics.ins-det].
- [35] *LHCb RICH: Technical Design Report*. LHCb-TDR-003. Geneva, 2000.
- [36] H. P. K. K. *Photomultiplier Tube Handbook (all chapters)*. [Online; accessed 14. May 2018]. May 2018. URL: http://www.hamamatsu.com/jp/en/community/optical_sensors/articles/photomultiplier_tube_handbook/index.html.
- [37] A. A. Alves Jr. et al. “Performance of the LHCb muon system”. In: *JINST* 8 (2013), P02022. DOI: 10.1088/1748-0221/8/02/P02022. arXiv: 1211.1346 [physics.ins-det].
- [38] P. Perret and X. Vilasís-Cardona. “Performance of the LHCb calorimeters during the period 2010-2012”. In: *J. Phys. Conf. Ser.* 587.1 (2015), p. 012012. DOI: 10.1088/1742-6596/587/1/012012.
- [39] I. Machikhiliyan and the LHCb calorimeter group. “The LHCb electromagnetic calorimeter”. In: *J. Phys. Conf. Ser.* 160.1 (Apr. 2009), p. 012047. ISSN: 1742-6596. DOI: 10.1088/1742-6596/160/1/012047.
- [40] R. Aaij et al. “Performance of the LHCb calorimeters”. In: (2014). in preparation.
- [41] A. C. Benvenuti et al. “A shashlik calorimeter with longitudinal segmentation for a linear collider”. In: *Nuclear Instruments and Methods in Physics Research Section A: Accelerators, Spectrometers, Detectors and Associated Equipment* 461.1 (Apr. 2001), pp. 373–375. ISSN: 0168-9002. DOI: 10.1016/S0168-9002(00)01247-X.

- [42] F. Sauli. “GEM: A new concept for electron amplification in gas detectors”. In: *Nucl. Instrum. Meth.* A386 (1997), pp. 531–534. DOI: 10.1016/S0168-9002(96)01172-2.
- [43] [Online; accessed 27. May 2019]. Dec. 2018. URL: <http://lhcbdoc.web.cern.ch/lhcbdoc/stripping/config/stripping21r1/index.html>.
- [44] [Online; accessed 21. May 2019]. Dec. 2018. URL: http://lhcbdoc.web.cern.ch/lhcbdoc/stripping/config/stripping21r1/bhadron/strippingbc2hhh_kpipi_exclline.html.
- [45] [Online; accessed 21. May 2019]. Dec. 2018. URL: http://lhcbdoc.web.cern.ch/lhcbdoc/stripping/config/stripping21r1/bhadron/strippingbc2hhh_kkpi_exclline.html.
- [46] M. Adinolfi et al. “Performance of the LHCb RICH detector at the LHC”. In: *Eur. Phys. J. C* 73 (2013), p. 2431. DOI: 10.1140/epjc/s10052-013-2431-9. arXiv: 1211.6759 [physics.ins-det].
- [47] The Starterkit team and contributors. *The LHCb data flow · GitBook*. [Online; accessed 19. Dec. 2018]. Dec. 2018. URL: <https://lhcb.github.io/starterkit-lessons/first-analysis-steps/dataflow.html>.
- [48] I. Belyaev et al. “Handling of the generation of primary events in Gauss, the LHCb simulation framework”. In: *J. Phys. Conf. Ser.* 331 (2011), p. 032047. DOI: 10.1088/1742-6596/331/3/032047.
- [49] T. Sjöstrand, S. Mrenna and P. Skands. “A brief introduction to PYTHIA 8.1”. In: *Comput. Phys. Commun.* 178 (2008), pp. 852–867. DOI: 10.1016/j.cpc.2008.01.036. arXiv: 0710.3820 [hep-ph].

- [50] C.-H. Chang et al. “BCVEGPY: an event generator for hadronic production of the Bc meson”. In: *Comput. Phys. Commun.* 159.3 (June 2004), pp. 192–224. ISSN: 0010-4655. DOI: 10.1016/j.cpc.2004.02.005.
- [51] D. J. Lange. “The EvtGen particle decay simulation package”. In: *Nucl. Instrum. Meth. A* 462 (2001), pp. 152–155. DOI: 10.1016/S0168-9002(01)00089-4.
- [52] J. Allison et al. “Recent developments in Geant4”. In: *Nuclear Instruments and Methods in Physics Research Section A: Accelerators, Spectrometers, Detectors and Associated Equipment* 835 (2016), pp. 186–225. ISSN: 0168-9002. DOI: <https://doi.org/10.1016/j.nima.2016.06.125>. URL: <http://www.sciencedirect.com/science/article/pii/S0168900216306957>.
- [53] M. Clemencic et al. “The LHCb simulation application, Gauss: Design, evolution and experience”. In: *J. Phys. Conf. Ser.* 331 (2011), p. 032023. DOI: 10.1088/1742-6596/331/3/032023.
- [54] *The MOORE Project*. [Online; accessed 17. Oct. 2018]. Oct. 2018. URL: <http://lhcbdoc.web.cern.ch/lhcbdoc/moore>.
- [55] *The BRUNEL Project*. [Online; accessed 17. Oct. 2018]. Oct. 2018. URL: <http://lhcbdoc.web.cern.ch/lhcbdoc/brunel>.
- [56] *The DAVINCI Project*. [Online; accessed 17. Oct. 2018]. Oct. 2018. URL: <http://lhcbdoc.web.cern.ch/lhcbdoc/davinci>.
- [57] M. Calvi et al. “Characterization of the Hamamatsu H12700A-03 and R12699-03 multi-anode photomultiplier tubes”. In: *JINST* 10.09 (2015), P09021. DOI: 10.1088/1748-0221/10/09/P09021. arXiv: 1506.04302 [physics.ins-det].

- [58] S. Aiello et al. "Aging characterization on large area photo-multipliers". In: *Nuclear Instruments and Methods in Physics Research Section A: Accelerators, Spectrometers, Detectors and Associated Equipment* 725 (2013). VLVvT 11, Erlangen, Germany, 12 - 14 October, 2011, pp. 151–154. ISSN: 0168-9002. DOI: <https://doi.org/10.1016/j.nima.2012.11.130>. URL: <http://www.sciencedirect.com/science/article/pii/S0168900212014775>.
- [59] M. Calvi et al. "First characterization of the Hamamatsu R11265 multi-anode photomultiplier tube". In: *Nuclear Instruments and Methods in Physics Research Section A: Accelerators, Spectrometers, Detectors and Associated Equipment* 766 (2014). RICH2013 Proceedings of the Eighth International Workshop on Ring Imaging Cherenkov Detectors Shonan, Kanagawa, Japan, December 2-6, 2013, pp. 156–159. ISSN: 0168-9002. DOI: <https://doi.org/10.1016/j.nima.2014.05.123>. URL: <http://www.sciencedirect.com/science/article/pii/S0168900214006925>.
- [60] O. GmbH. *Advanced Laser Diode Systems A.L.S. GmbH*. [Online; accessed 19. Apr. 2018]. Apr. 2018. URL: <http://www.alsgmbh.com/products>.
- [61] *81150A Pulse Function Arbitrary Noise Generator | Keysight (formerly Agilent's Electronic Measurement)*. [Online; accessed 19. Apr. 2018]. Apr. 2018. URL: <https://www.keysight.com/en/pd-1287544-pn-81150A/pulse-function-arbitrary-noise-generator?cc=GB&lc=eng>.
- [62] *VI729 / Digitizers | CAEN*. [Online; accessed 19. Apr. 2018]. Apr. 2018. URL: <http://www.caen.it/csite/CaenProd.jsp?idmod=465&parent=11>.

- [63] *Electronic Systems Engineering | PREP | Pool Catalog | EG & G/Ortec Directory | AN308NL Dual Linear Fan-In*. [Online; accessed 5. Dec. 2018]. Oct. 2008. URL: http://prep.fnal.gov/catalog/hardware_info/egg_ortec/an308nl.html.
- [64] *H12700 and R12699 datasheets*. [Online; accessed 19. Apr. 2018]. Apr. 2018. URL: https://www.hamamatsu.com/resources/pdf/etd/H12700_TPMH1348E.pdf.
- [65] B. L. Paredes et al. “Response of photomultiplier tubes to xenon scintillation light”. In: *arXiv* (Jan. 2018). doi: 10.1016/j.astropartphys.2018.04.006. eprint: 1801.01597.
- [66] M. Clemencic, B. Couturier and S. Kyriazi. “Improvements to the User Interface for LHCb’s Software continuous integration system.” In: *J. Phys. Conf. Ser.* 664.6 (2015), p. 062025. doi: 10.1088/1742-6596/664/6/062025.
- [67] M. Clemencic and B. Couturier. “A New Nightly Build System for LHCb”. In: *J. Phys. Conf. Ser.* 513 (2014), p. 052007. doi: 10.1088/1742-6596/513/5/052007.
- [68] M. Clemencic and B. Couturier. “LHCb Build and Deployment Infrastructure for run 2”. In: *J. Phys. Conf. Ser.* 664.6 (2015), p. 062008. doi: 10.1088/1742-6596/664/6/062008.
- [69] *LHCbPR < LHCb < TWiki*. [Online; accessed 1. May 2019]. May 2019. URL: <https://twiki.cern.ch/twiki/bin/view/LHCb/LHCbPR>.
- [70] M. Bostock, V. Ogievetsky and J. Heer. “D3: Data-Driven Documents”. In: *IEEE Trans. Visualization & Comp. Graphics (Proc. InfoVis)* (2011). URL: <http://vis.stanford.edu/papers/d3>.
- [71] S. Linev. *JSROOT*. <https://github.com/root-project/jsroot>.

- [72] *Consider deprecating Bower*. · Issue #2298 · bower/bower. [Online; accessed 5. Dec. 2018]. Dec. 2018. URL: <https://github.com/bower/bower/issues/2298>.
- [73] Node.js Foundation. *Releases | Node.js*. [Online; accessed 27. May 2019]. May 2019. URL: <https://nodejs.org/en/about/releases>.
- [74] *Angular - Angular versioning and releases*. [Online; accessed 27. May 2019]. Apr. 2019. URL: <https://angular.io/guide/releases>.
- [75] *LHCb Core Software / LHCbPR2FE*. [Online; accessed 20. May 2019]. May 2019. URL: <https://gitlab.cern.ch/lhcb-core/LHCbPR2FE>.
- [76] *MeerkatPIDResampling < LHCb < TWiki*. [Online; accessed 5. Dec. 2018]. Dec. 2018. URL: <https://twiki.cern.ch/twiki/bin/view/LHCb/MeerkatPIDResampling>.
- [77] M. Pivk and F. R. Le Diberder. “sPlot: A statistical tool to unfold data distributions”. In: *Nucl.Instrum.Meth.* A555 (2005), pp. 356–369. DOI: 10.1016/j.nima.2005.08.106. arXiv: physics/0402083 [physics.data-an].
- [78] LHCb Collaboration. *LHCb-INT-2017-007*. Unpublished.
- [79] S. Tolk et al. “Data driven trigger efficiency determination at LHCb”. In: *CERN Document Server* (May 2014). URL: <https://cds.cern.ch/record/1701134>.
- [80] F. Pedregosa et al. “Scikit-learn: Machine Learning in Python”. In: *Journal of Machine Learning Research* 12 (2011), pp. 2825–2830.
- [81] L. Breiman. *Classification and Regression Trees*. CRC Press, 2017. ISBN: 978-135146048-4.

- [82] D. (<http://cs.stackexchange.com/users/755/d-w>). *Size of decision tree and depth of decision tree*. Computer Science Stack Exchange. URL:<http://cs.stackexchange.com/q/39699> (version: 2015-02-23). eprint: <http://cs.stackexchange.com/q/39699>. URL: <http://cs.stackexchange.com/q/39699>.
- [83] J. Zhu et al. “Multi-class adaboost”. In: *Statistics and its Interface 2.3* (2009), pp. 349–360.
- [84] M. Stone. “Cross-Validatory Choice and Assessment of Statistical Predictions”. In: *Journal of the Royal Statistical Society. Series B (Methodological)* 36.2 (1974), pp. 111–147. ISSN: 0035-9246. DOI: 10.2307/2984809.
- [85] G. Punzi. “Sensitivity of searches for new signals and its optimization”. In: *Statistical Problems in Particle Physics, Astrophysics, and Cosmology*. Ed. by L. Lyons, R. Mount and R. Reitmeyer. 2003, p. 79. arXiv: physics/0308063.
- [86] D. Martinez Santos and F. Dupertuis. “Mass distributions marginalized over per-event errors”. In: *Nucl. Instrum. Meth. A* 764 (2014), pp. 150–155. DOI: 10.1016/j.nima.2014.06.081. arXiv: 1312.5000 [hep-ex].
- [87] T. Skwarnicki. “A study of the radiative cascade transitions between the upsilon-prime and upsilon resonances”. In: *DESY* (1986). URL: <https://core.ac.uk/display/25146039>.
- [88] A. McNeil, R. Frey and P. Embrechts. *Quantitative Risk Management: Concepts, Techniques, and Tools*. Princeton Series in Finance. Princeton University Press, 2005. ISBN: 9780691122557. URL: https://books.google.co.uk/books?id=f5J%5C_0ZPeq50C.
- [89] *IEEE 2017 NSS/MIC/RTSD Online Program*. [Online; accessed 20. Dec. 2018]. Dec. 2018. URL: https://www.eventclass.org/contxt_ieee2017/online-program/session?s=450.